Master Thesis in Instrumentation and Measurement Science

Low-energy surface vibration measurements on the α-quartz (0001) surface

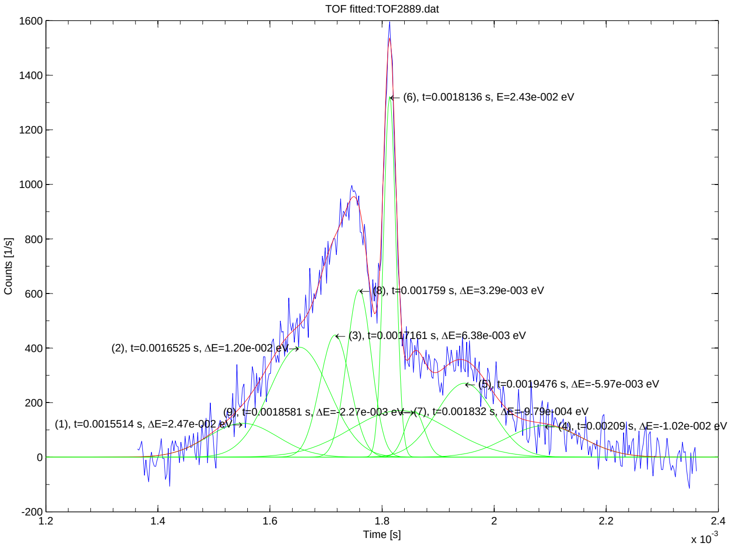

Jenny Louise Luneng
March 14, 2011

Dedicated to Bjarte and Robin.

Abstract

Despite the enormous range of usages, only little is known about the dynamic and structural properties of quartz (SiO_2) surfaces on the atomic scale. The main reason for this is probably that quartz is an insulator, with the outermost surface layer consisting entirely of oxygen atoms. This means that it is difficult to investigate quartz with most surface science techniques which investigates the material on the atomic level. Three years ago, the first paper on the low-energy surface phonons on the α-quartz (0001) surface were published. The paper presented results measured using helium scattering as well as a theoretical prediction of the phonon spectra. The experimental results presented only partially agreed with the theoretically predicted energy spectrum, and in particular there were no phonon measurements fitting into the lower energy band predicted at around 5 meV.

The main aim for this thesis was to investigate if the predicted low-energy surface phonons, not found from earlier experiments, are in fact present at the surface. For that, new measurements at different surface conditions and with a higher energy resolution than previously used, were performed using helium atom scattering. The results were analyzed using a new fitting procedure.

The main outcome of this thesis is that lower phonon energy bands could be found. For the $\Gamma\vec{K}$-direction of the Brillouin zone the dispersionless phonon mode was found at (2,3 +/- 0,6) meV and higher overtones at (6,1 +/- 0,5) meV and at (10,9 +/- 1,5) meV. For the $\Gamma\vec{M}$-direction of the Brillouin zone the dispersionless phonon mode was found at (2,9 +/- 0,4) meV, higher overtones at (6,6 +/- 0,6) meV and at (10,8 +/- 1,5) meV.

Abstrakt

Selv om kvarts (SiO_2) brukes i mange forskjellige vitenskaper, vet man veldig lite om den dynamiske og strukturelle oppbyggingen av kvartsoverflaten på atomær skala. Grunnen til dette er sannsynligvis at kvarts er en isolator, hvor de første overflatelagene bare består av oksygenatomer. Dette betyr at det er vanskelig å utforske kvarts med de fleste overflateteknikker brukt på atomært nivå. For tre år siden ble den første artikkelen om overflatefononer på α-kvarts (0001) overflaten publisert. Denne artikkelen presenterte resultater av målinger gjort ved spredning av heliumatom, og i tillegg ble det presentert teoretiske beregninger av fononspekteret. De eksperimentelle resultater stemte bare til en viss grad med det teoretiske energispekteret, hvor særlig mangelen på fononer i det lavere energibåndet rundt 5 meV var overraskende.

Hovedmålet med denne masteroppgaven var å undersøke om lavenergifononene som ikke ble funnet i de første eksperimentene faktisk er tilstede på overflaten. For dette er det gjort nye spredningsmålinger med heliumatomer ved forskjellige overflatebetingelser, og med en høyere energioppløsning enn hva som ble gjort tidligere. For analysering brukes en nyutviklet tilpasningsprosedyre, som er presentert i denne oppgaven.

Hovedresultatet i denne materoppgaven er at overflatefononbånd med lavere energi ble funnet. For $\Gamma\vec{K}$-retningen til Brillouinsonen er det funnet dispersjonsløst modus ved (2,3 +/- 0,6) meV og høyere overtoner ved (6,1 +/- 0,5) meV og (10,9 +/- 1,5) meV. For $\Gamma\vec{M}$-retningen til Brillouinsonen er det funnet dispersjonsløst modus ved (2,9 +/- 0,4) meV og høyere overtoner ved (6,6 +/- 0,6) meV og (10,8 +/- 1,5) meV.

Acknowledgment

First of all i would like to thank my supervisor, Professor Bodil Holst, for all the support and help during this master project. I would also like to thank her for not making my maternity leave a problem. A special thanks to Bjørn Samelin for all the effort he put in my thesis, for the stimulating discussions and for never letting me feel that a question is stupid.

I would like to thank Katrin Fladischer for doing the measurement with such dedication and for writing notes with such accuracy.

Many thanks to Elin Søndergård and Anne Lelarge from the Laboratoire Surface et Interface du Verre, Saint Gobain Recherche for preparing the samples.

I would also like to thank Haakon Fossen for supplying me with a beautiful picture of a quartz crystal.

A huge thanks goes to my office mates, Sabrina Eder and Thomas Reisinger, for pushing me a bit harder. I would also like to thank them for all the time they have used to help, for the long and instructive discussions and for the endless coffee breaks.

A special thanks goes to Bjarte Høydal for all the love and support throughout my entire study and Robin Høydal Luneng for all the hugs and kisses I got when I needed them the most. Mum, Bente Luneng, and dad, Halvard Sivertsen, also deserve a special thanks for always being there for me and my little family.

To my best friend, Hege Erdal: Thank you for being you! Thanks for all the encouragement, and for thanks for correcting my grammar.

Also many thanks to my fellow students and friends Selda, Beate, Sigrid and Monica for many motivational conversations and for all the coffee we drank together.

Contents

List of Figures

List of Tables

Chapter 1

Introduction

12% of the earth crust consists of quartz, (SiO_2), and it is one of the most common minerals on earth [1]. Quartz is here taken to refer to crystalline or polycrystalline SiO_2 in various forms. Quartz can exist in a range of forms [2], as Table 1.1 shows. Figure 1.1 is showing a quartz crystal found at Hardangervidda.

The only stable crystalline form on earth is α-quartz. But also the amorphous form (SiO_2) silica glass can for all practical purposes be considered stable at terrestrial conditions [4].

The different forms of SiO_2 are built of tetrahedron shaped units, with a Si-atom in the center and surrounded by oxygen atoms, see Figure 1.2. All work presented in this thesis is concerned with the investigation of the α-quartz (0001) surface. Silica glass and quartz are extremely important for a wide range of applications, ranging from optical components [6], microelectronics [7] and even biotechnology (for example interactions of silica surfaces with water and biomolecules) [8].

Despite the enormous range of usages, only little is known about the surfaces of quartz on the atomic/nano level. The reason for this is that quartz is an insulator, with the outermost surface layer consisting entirely of oxygen atoms. That means that it is difficult to investigate quartz with most surface science techniques which investigates the material on the atomic level. I.e. low energy electron diffraction (LEED), gracing incidence X-ray diffraction and scanning tunneling microscopy

Figure 1.1: Quartz crystal from Hardangervidda [3].

Table 1.1: Modifications of crystalline SiO_2 [4].

Modification	Crystal system
α-quartz	Trigonal
β-quartz	Hexagonal
α-tridymite	Rhombic
β-tridymite	Hexagonal
α-cristobalit	Tetragonal
β-cristobalite	Cubical
Stishovit	Tetragonal
Coesit	Monoclinic
Keatit	Tetragonal

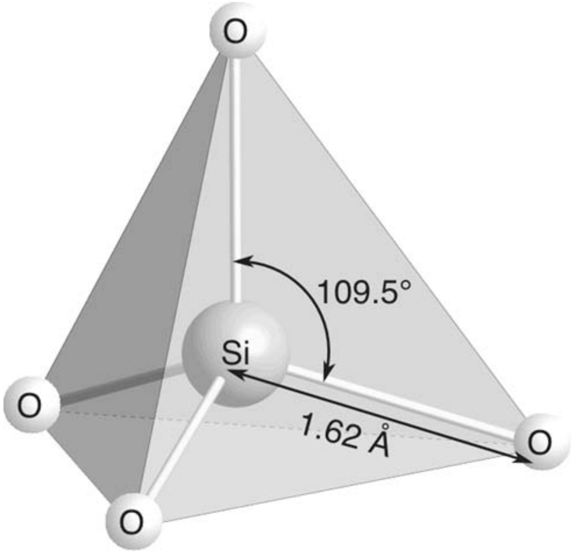

Figure 1.2: The basic tetrahedron of the SiO_4-group. The Figure is shown with average bond length and angle [5].

(STM). First experiments were carried out on the α-quartz (0001) surface in 1970 using LEED [9]. The crystal was polished and then etched in hydrofluoric acid in order to remove damaged layers. This experiments showed a hexagonal diffraction pattern with a periodicity of (1×1) corresponding to the periodicity of the bulk, and no rotation relative to the bulk. Due to charging effects it was not possible to obtain very good diffraction patterns. Further experiments on α-quartz (0001) were carried out in the 1990s [10]. These measurements confirmed the hexagonal diffraction pattern from previous measurements for samples annealed up to $500°C$. For the samples annealed above 600°, the diffraction showed an additional $(\sqrt{84}\times\sqrt{84})R11°$ surface reconstruction. First measurements on the α-quartz (0001) surface using Atomic Force Microscopy (AFM) were performed in 2003 [11]. However, only features down to about 70 nm could be resolved in this work.

In 2007 the first experiments using helium atom scattering (HAS) from the α-quartz (0001) surface were performed [12]. Measurements were carried out on a surface annealed to 1025°C for 72 hours under a pressure of 2 bar of oxygen. The diffraction pattern reported here confirmed the hexagonal surface pattern showed by LEED some years earlier. The work on resolving the surface structure of α-quartz (0001) is still ongoing. See for example [13], [14] and [15].

HAS is an established, even though a not so widely used technique, for investigating surface structures and dynamical properties of surfaces. In 1928 Knauer and Stern [16] searched with a beam of molecules of hydrogen and helium, for diffraction patterns from crystals, and Stern managed together with Estermann in 1930 to get diffraction peaks from a LiF-surface [17]. In the 1980s there was an important breakthrough; the introduction of the supersonic He-nozzle beam which made it possible to create molecular beams with a narrow velocity spread ($\frac{\Delta v}{v} > 1\%$) [18]. This increased the field of applications considerably, making it possible to obtain precise diffraction patterns and to use molecular beams, in particular helium, for the study of low-energy surface phonons.

Phonons are quantized modes of vibration in a crystal lattice, and the physical properties (like thermal and electrical conductivities) of a crystal can be at least partially explained by them. Bulk phonons have already been studied by neutron scattering since the 1950s [19]. In 1965 there was a first attempt to study surface vibrations on a clean (100) tungsten crystal using LEED [20]. The first to measure phonons using helium atom scattering, was Bledsoe and Fischer [21] in their work on scattering from LiF(001) in 1974.

The advantage of helium atom scattering is that it is strictly surface sensitive and non destructive. Because of the low energies typically used $(10-300)$ meV, the incoming atoms only probe the outermost layers of the crystal, and there is absolutely no penetration into the bulk. These low energies correspond to a de Broglie wavelength of the order of a few Ångström (see Figure 1.3), and that is in the range of the lattice constants of solid materials. Another important feature coming along with the low energies are that they allow investigation of very fragile materials (as long as the materials are stable in ultra high vacuum). Helium atoms are electrically neutral and chemically inert, and HAS is therefore not limited to conductive metal surfaces, but can also be used on insulators (like quartz) and semiconductors.

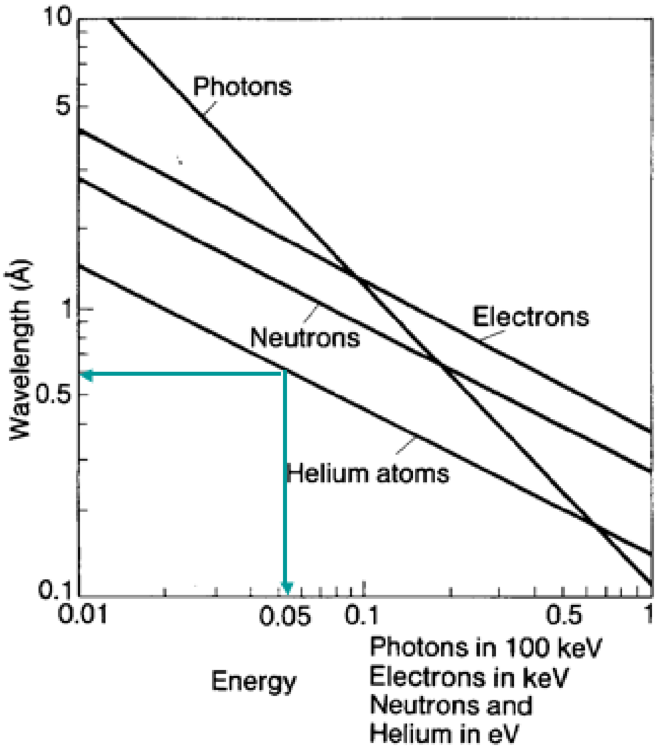

Figure 1.3: Energy vs. wavelength for different particles. [22]. Note that the energy of helium is more than 1000 times smaller than the energy of electrons for a given wavelength.

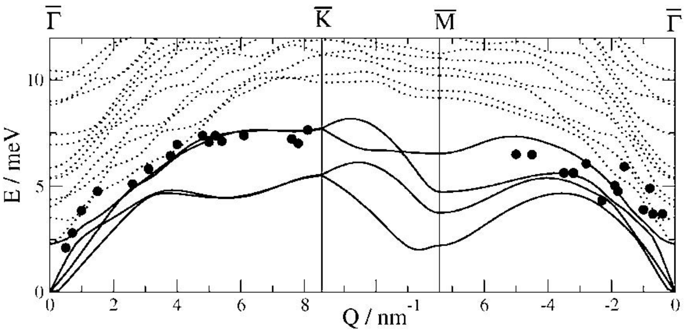

Figure 1.4: Calculated phonon-dispersion curves as a function of the surface wave vector $\vec{Q}$ along the boundaries of the irreducible part of the first surface Brillouin zone for a dry α-quartz (0001) surface. Circular dots denote experimentally measured values [23].

Shortly after the publishing of the first structural paper on α-quartz investigated with helium atom scattering, also the first paper on the low-energy surface phonons on α-quartz was published [23]. This paper yielded results which only partially agreed with the theoretically predicted spectrum, see Figure 1.4. In particular the lack of phonon measurements in the lower energy band is puzzling. For this reason it was decided to perform a new series of phonon measurements, with the main goal to ensure if the low-energy phonons predicted by theory were present or not. This has been the main topic of this thesis.

The preparation for the measurements began in October 2008. The instrument used for these measurements, MaGiE -'Makroskopische Gitter Experimente', was the same instrument that had been used for the original phonon measurements [23]. After MaGiE had been moved from Graz in Austria to Bergen, an oil-free pre-vacuum pump and a new turbo molecular pump were installed, so a new, faster venting procedure for the target chamber was developed. I also designed a new and improved sample holder for the quartz crystal.

In March 2009 I went for Maternity leave and I had to put the project temporarily on hold. At that time all components for carrying out the measurements were finished, and a first quartz sample had already been tested, but unfortunately no results could be obtained from this sample due to an unforeseen problem with oil-contamination. The measurements presented in this thesis were then performed by Katrin Fladischer, in the time period of 13.04.2010 - 28.07.2010. The 10 mm × 10 mm × 1 mm crystal used was supplied by *Crystal GmbH.* It was prepared from a synthetically grown and twin free α-quartz crystal, cut along the (0001)-direction with a miscut less than 0,3 % by Anne Lelarge and Elin Søndergård from the *Laboratoire Surface et Interface du Verre, Saint Gobain Recherche* in Aubervilliers, France and transported to Bergen in an argon container. The details are described in Section 3.3.4. The data has been analysed using a Matlab fitting program developed for the group by Bjørn Samelin.

The structure of the thesis is as follows:

- Chapter 2 begins with a short introduction to the concept of crystal structures, which is the fundamental background for this work, followed by a presentation of the crystal structure of quartz. Then follows a description of the concept of phonons. The chapter finishes with a discussion on helium scattering from surfaces.

- A general description of the apparatus MaGiE is presented in Chapter 3, with a particular emphasis on the components that have been modified/developed as part of this thesis. The setup and calibration for the measurements are also included in this chapter.

- In Chapter 4 the process for analyzing the phonon measurements of the α-quartz (0001) surface using helium atom scattering and time-of-flight (TOF)-analysis is described. The basic principle of TOF is to measure the time t the particle has used to travel a length L to get the average speed, $v = \frac{L}{t}$. This is done by dividing the He-beam into small pulses by a chopper and recording the arrival of the atoms at the detector with time resolution. The fitting procedure of the TOF-spectra is thoroughly described in Section 4.2.

- In Chapter 5 first the diffraction patterns for different sample orientations are reviewed. Then the results of the phonon measurements are given and compared with theory. The main result is that the low-energy phonon band could now be identified.

- In Chapter 6 the conclusion and outlook is found.

Chapter 2

Theory

This chapter begins with a short introduction to the concept of crystal structures, which is the fundamental background for this work, followed by a presentation of the crystal structure of quartz. Then comes a description of the concept of phonons. The chapter finishes with a discussion on helium scattering from surfaces.

2.1 The concept of crystal structures

A single crystal is build up by a regular, periodic structure of different components (atoms, molecules or ions), which is repeated throughout the whole volume. If we neglect the chemical structure of the repeated unit, and just look at the periodicity, we can define the Bravais lattice.

All points in a Bravais lattice can be described by position vectors, $\vec{R}$:

$$\vec{R} = n_1\vec{a}_1 + n_2\vec{a}_2 + n_3\vec{a}_3. \tag{2.1}$$

$\vec{a}_1$, $\vec{a}_2$ and $\vec{a}_3$ are any three vectors (not parallel and orthogonal to each other), n_i is an integer. The lattice has to be invariant during translation, $\vec{T} = v_1\vec{a}_1 + v_2\vec{a}_2 + v_3\vec{a}_3$, where v_i is an integer. The number of Bravais lattices is fixed.

In other words, a Bravais lattice is a spatial pattern of discrete points that looks identical from every position in the lattice [24].

2.1.1 Crystal surfaces

A crystal surface can be described as a periodic structure in two dimensions. That does not mean that the atoms necessarily have to be situated in a plane, but rather that the surface is periodic only in two dimensions [26]. It is the two-dimensional periodicity of the surface that lets us classify the expected symmetry elements and the different surface structures. The surface of a crystal will usually exhibit steps with various heights, and these steps separate domains of atomic planes. Defects such as adsorbed atoms and kinks can be detected. This is the so called TLK (Terrace, Kink, Ledge) - model, see Figure 2.1 [25].

Corresponding to the bulk crystallography, a 2D Bravais lattice can also be

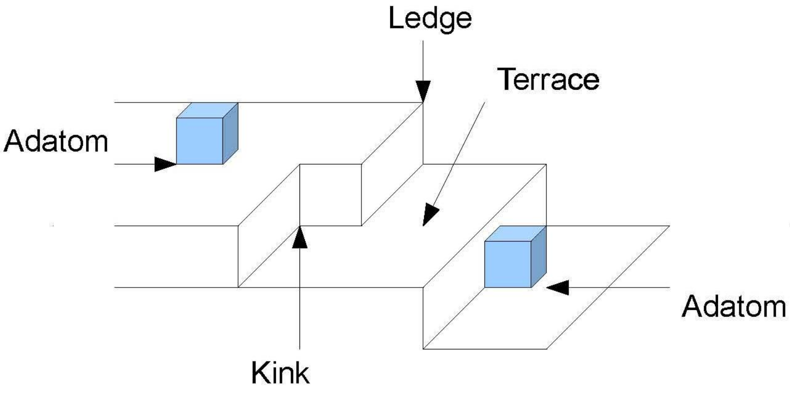

Figure 2.1: A TLK-model of the surface [25].

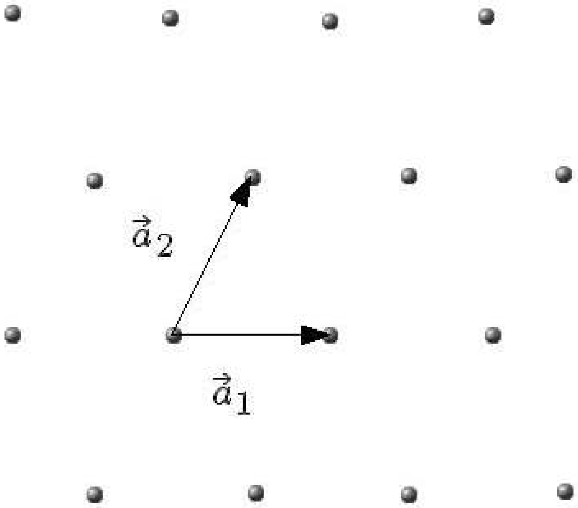

Figure 2.2: The parallelogram made from the sides $\vec{a}_1$ and $\vec{a}_2$ is called the primitive cell. A primitive cell will fill all space by repetition of suitable crystal translation operations [26].

defined for the description of the two-dimensional surface symmetry.

$$\vec{r} = n\vec{a}_1 + m\vec{a}_2,\ n, m = 0,\ \pm1,\ \pm2,\ \pm3\ \ldots \tag{2.2}$$

Notation for surface structure

When the translation vectors corresponding to the primitive cell on the surface are $n\vec{a}_1$ and $m\vec{a}_2$, see Figure 2.2, the superstructures can be written as $p(n \times m)$ (p, meaning primitive, is sometimes omitted). This simple notation is useful when the surface unit cell is in registry with the unit cell of the substrate. When the surface unit cell is rotated corresponding to the unit cell in the substrate, or when the relationship between the cell dimensions is not an integer, this notation needs to be extended: For simple rotations, $(x \times y)R\Theta$, denotes a surface structure that is obtained from the unit cell by a rotation of Θ and the length of the base vectors times x and y, where x and y are not necessarily integers [25].

2.1.2 Reciprocal space of a surface

In solid state physics, it is common to study diffraction of waves from crystals. The diffraction peaks are described using the reciprocal lattice notation. The reciprocal lattice for a given Bravais lattice is the set of all vectors, $\vec{K}$, that yields plane waves, $e^{i\vec{K}\cdot\vec{r}}$, with the periodicity of the Bravais lattice itself [27].

With $\vec{R} = n_1\vec{a}_1 + n_2\vec{a}_2$, and n_i as any integer, $\vec{R}$ represents the two-dimensional Bravais lattice, see Section 2.1. This plane wave has to be invariant during translation with any of these lattice vectors:

$$e^{i\vec{K}\cdot(\vec{r}+\vec{R})} = e^{i\vec{K}\cdot\vec{r}}. \tag{2.3}$$

This is valid for all $\vec{R}$ in the Bravais lattice and any $\vec{r}$ [27].

The reciprocal lattice is important because it can be directly observed in diffraction experiments.

Each point of the two dimensional reciprocal lattice is defined by the reciprocal lattice vector G_{hk}

$$G_{hk} = h\vec{a}_1^* + k\vec{a}_2^*. \tag{2.4}$$

h and k are integers.

The parallelogram that appears from the vectors $\vec{a}_1^*$ and $\vec{a}_2^*$ defines the reciprocal unit cell. This is related to the real space unit cell by

$$\vec{a}_1^* = 2\pi\frac{\vec{a}_2 \times \vec{n}}{\vec{a}_1 \cdot (\vec{a}_2 \times \vec{n})}. \tag{2.5}$$

$$\vec{a}_2^* = 2\pi\frac{\vec{n} \times \vec{a}_1}{\vec{a}_2 \cdot (\vec{n} \times \vec{a}_1)}. \tag{2.6}$$

$\vec{n}$ is the unit vector perpendicular to the surface, and a_1 and a_2 are the vectors corresponding to the primitive cell in Figure 2.2. The reciprocal lattice of the reciprocal lattice is the original Bravais lattice [27].

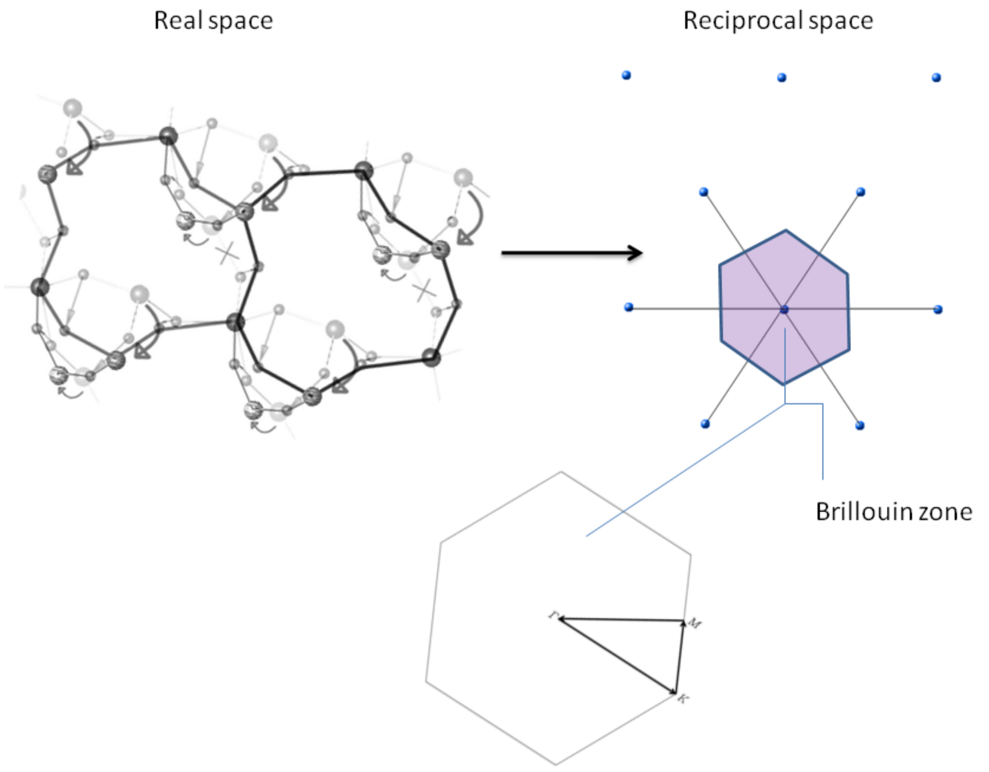

Figure 2.3: Left: The predicted reconstructed surface of α-quartz (0001) [12]. Right: The corresponding Brillouin zone. Note that the Brillouin zone is rotated by 30° to the corresponding primitive cell. Below: The corresponding Brillouin zone. Γ is the center point, K is the corner point and M is the middle point of an edge joining two hexagonal faces. The measurements done for this thesis are done in the ΓM-direction and the ΓK-direction.

2.1.3 Brillouin zone

The (first) Brillouin zone corresponds to a primitive unit cell in reciprocal space. It is formed by drawing vectors from a reciprocal lattice point (the origin) to all neighboring reciprocal lattice points, constructing planes perpendicular to, and passing through, the midpoints of these vectors. The Brillouin zone is the smallest reciprocal area, about the origin bounded by these planes [28]. The Brillouin zone for the α-quartz (0001) surface can be seen in the right part of Figure 2.3. The left part is a predicted reconstruction of the α-quartz (0001) surface from [12]. The bottom picture of Figure 2.3 shows the notation for the directions the measurements where made at in this thesis.

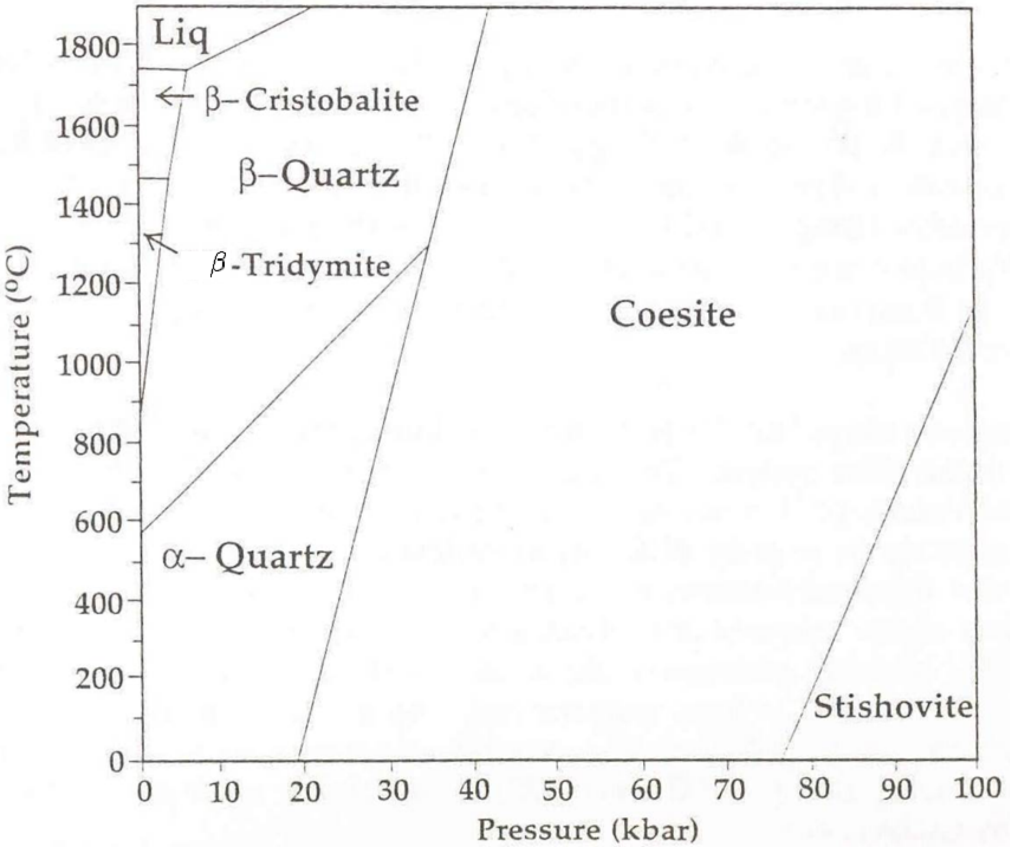

Figure 2.4: Phase diagram for the various polymorphs of SiO_2. It is only showing the polymorphs that are formed by pure SiO_2 at certain temperatures and pressures. The ones found on earth are α-quartz, α-tridymite, α-cristobalite and amorphous silica [4].

2.2 The structure of crystalline quartz

Quartz is in general composed of two parts of oxygen and one part silicon (silicon dioxide), SiO_2. The silicon atom is placed in the center of a tetrahedron with the oxygen atoms located in the four corners, see Figure 1.2. Each O-Si-O angle is $109,5°$. In α-quartz, tetrahedrons are connected together to form a trigonal crystal [2]. SiO_2 can occur in a number of other structures - polymorphs. Except from α-quartz, the other structures are only stable under high temperature, high pressure or a combination of the two conditions mentioned [4].

A simple way of displaying the polymorphs of quartz, is in a phase diagram, as in Figure 2.4

2.2.1 Surface structure of α-quartz (0001)

Both quartz and silica glass are important in many advanced technological fields like microelectronic [7] and optics [6]. Even though the bulk structure of quartz has been widely studied, only little is known about the surfaces of quartz on the

Table 2.1: Modifications of crystalline SiO_2. [2]

Modification	Crystal system
α-quartz	Trigonal
β-quartz	Hexagonal
α-tridymite	Rhombic
β-tridymite	Hexagonal
α-cristobalit	Tetragonal
β-cristobalite	Cubical
Stishovit	Tetragonal
Coesit	Monoclinic
Keatit	Tetragonal

Table 2.2: Computed surface energies for the five different models: dimer, cleaved, VAP, semidense and dense surfaces in ascending order of stability [30].

Model	Surface Energy [ev/Å]
Dimer (2×1)	0,25
Cleaved (1×1)	0,17
VAP (2×1)	0,14
Semidense (2×1)	0,09
Dense (1×1)	0,05

atomic/nano scale. Because quartz is an insulator, it is difficult to investigate quartz with most surface science technologies that investigate materials on an atomic level, i.e low energy electron diffraction (LEED), gracing incidence X-ray diffraction and scanning tunneling microscopy (STM).

The very first HAS-spectra [12] have confirmed the (1×1) pattern previously observed in LEED studies [9], but the HAS-spectra also showed additional (2×2) peaks. These experimental results were found to be in good agreement with the recent theoretical calculations from de Leeuw et al. [29] and Rignanese et al. [30].

To account for the symmetries in the HAS-spectra, a model has been proposed where terraces with step heights of about 1/3 of the unit cell height lead to domains that are rotated $\pm 60°$ relative to each other, see Figure 2.5. This model and the experimental data correspond well with the theoretical predictions that foresee a (1×1) surface reconstruction with 120° symmetry of the unit cell. The explanation of the weak (2×2)-peaks (labeled with * in Figure 2.5) is provided by Rignanese et al. [30]:

Of the four possible explanations, the dense (1×1) structure is the one that is the energetically most favorable (see Table 2.2), but the semi-dense surface structure proposed with a (2×1) reconstruction has a surface energy close to the one of the dense surface. This semi-dense surface structure would explain the diffraction pattern, since a hexagonal (1×1) structure combined with 3 domains of (2×1) structure can give a diffraction pattern similar to a (1×1) structure combined with a (2×2) structure.

The most recent paper by Chen et al. [31] is stating that the experimentally observed (2×2) pattern from [12], can be explained by combinations of (2×1)

surfaces more energetically stable than the dense (1×1) surfaces.

Figure 2.7 shows an image of the unreconstructed α-quartz (0001) surface. Recent theoretical calculations from [12], [29] and [30] have predicted reconstructions of the dry surface (no water present), as shown in Figure 2.8, and of the fully hydroxylated surface as shown in Figure 2.9. These surface reconstructions are important, since the dry surface corresponds to the initial state after sample preparation, and the hydroxylated surface is known to be the most stable.

Figure 2.10 shows an AFM image from [12] that shows large, atomically flat terraces with an average step height of 1.9nm and an average width of 200nm. The terraces are oriented 60° with respect to each other, which indicates the presence of domains, see Figure 2.5. The HAS diffraction spectra in Figure 2.6 have narrow specular peaks (limited by the present angular resolution of the apparatus, FWHM about 0,006 Å^{-1}) indicating long terraces with a mean width of at least 200Å (See Section 2.5). This is consistent with the AFM picture. The diffraction patterns also show a 60° azimuthal symmetry.

LEED-experiments on the α-quartz surface indicates an (1×1)-pattern [9], which for temperatures over 600° undergoes a reconstruction of $(\sqrt{84} \times \sqrt{84})R11^\circ$ [10].

The measurements of the surface structure of α-quartz, which were performed as part of the work for this thesis, confirm the published results, see Chapter 5.

2.3 Phonons

The motions of a crystal lattice can be described mathematically as a superposition of normal modes [24]. Due to quantum mechanical effects not all modes are allowed. In other words, the lattice vibrations are quantized and these quantized modes are referred to as phonons. This is in analogy of the photon; the quantum of the electromagnetic field. The word phonon comes from the Greek word $\phi\omega\nu\acute{\eta}$ (phonē), which translates to sound. In the simplest model, a crystal lattice can be seen as a series of atoms connected by springs, as seen in Figure 2.12. For a given unit cell containing more than one atom, there are two types of vibrations (or phonons) that can exist; optical phonons, where all the atoms in the unit cell oscillate 90 degrees out of phase, the lightest atom with biggest amplitude, and acoustic phonons, where the atoms in the unit cell are oscillating in phase (like sound waves), see Figure 2.13. The optical phonons are called optical because in ionic crystals, where the two atoms in the unit cell have opposite charge, they are excited by electromagnetic (optic) radiation [24].

There are three modes of acoustic phonons: two transverse modes (where $\vec{k}_\perp$ is perpendicular to the direction of propagation) and one longitudinal mode (where $\vec{k}_{||}$ is parallel to the direction of propagation), see Figure 2.11. Also the optical phonons have longitudinal and transverse modes [26]. The low velocity acoustic surface mode is called the Rayleigh wave or Rayleigh phonon. The Rayleigh phonon dispersion curve crosses in general the whole Brillouin zone, and is known by its special characteristic; the linear frequency versus wave number close to the Brillouin zone center [32]. An example of the linear frequency is given in Figure 2.15.

p atoms in the primitive cell corresponds to $3p$ branches in the dispersion relation:

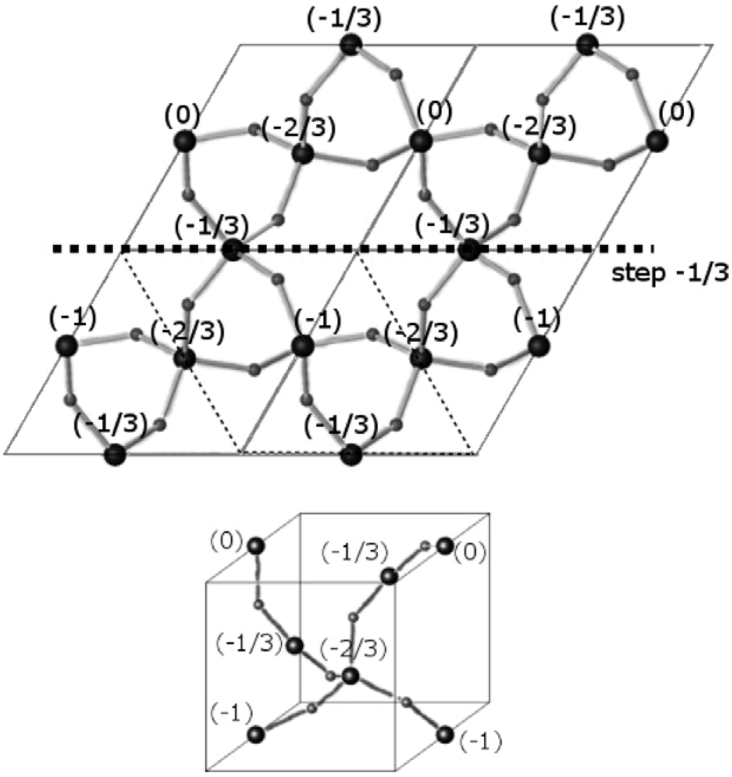

Figure 2.5: A model of how the presence of steps on the α-quartz (0001) surface can lead to domains rotated by ±60°. The numbers in brackets indicates the height position (given as fraction of unit cell heights) of the silicon atoms relative to the topmost surface atoms at position (0). The dotted bold line indicates the position of steps of 1/3 unit cell height. The pale dotted line denotes the surface unit cell for the -1/3 layer, and this layer is rotated 60° relative to the unit cell in the top layer. The bottom drawing shows the unit cell of the bulk. In both of the drawings, the silicon atoms are depicted as large black balls, and the oxygen atoms as small grey balls [12].

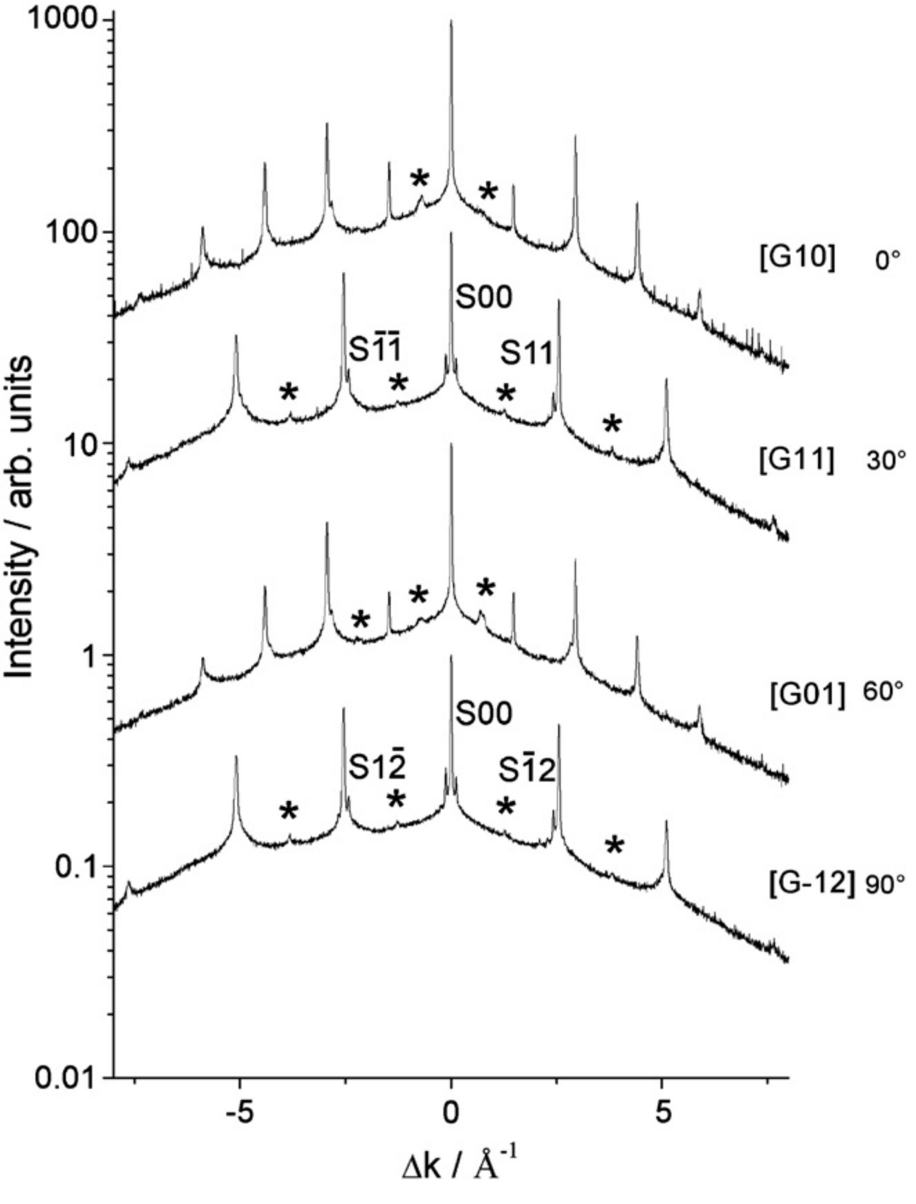

Figure 2.6: In-plane helium atom diffraction spectra for a range of crystal orientations (indicated by the reciprocal lattice indices and the in-plane angle). The helium beam energy was 67.3 meV which corresponds to a wave length, $\lambda_i = 0,55$ Å. SXX denote the most prominent satellite peaks (the sometimes recognizable small peaks placed next to the main diffraction peak) where XX stands for the lattice indices of the related main peak. Additional weak peaks are labeled with *, and these weak peaks correspond to the (2x2) reconstruction described in the main text [12].

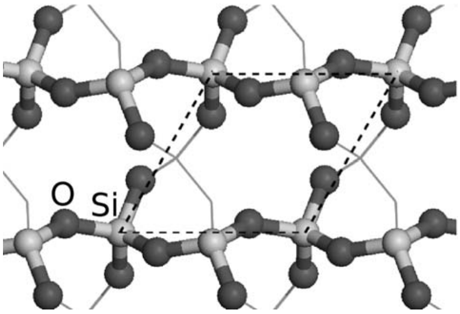

Figure 2.7: Projection of a cleaved α-quartz surface onto the (0001)-plane [23].

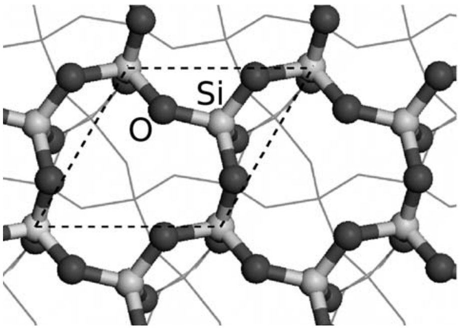

Figure 2.8: Projection of a reconstructed, dry (no water present) α-quartz surface onto the (0001)-plane. Under dry condition, the cleaved surface from Figure 2.7 relaxes to the form present in this figure, with a reduced surface energy of 1,48 J/m^2 compared to 4,0 J/m^2 for the cleaved surface [23].

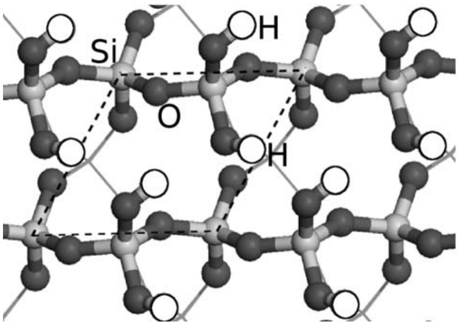

Figure 2.9: Projection of a reconstruction of a fully hydroxylated α-quartz surface onto the (0001)-plane. The surface energy here is 0,38 J/m^2, and that is even lower than the cleaved surface in Figure 2.7 and the dry surface in Figure 2.8 [23].

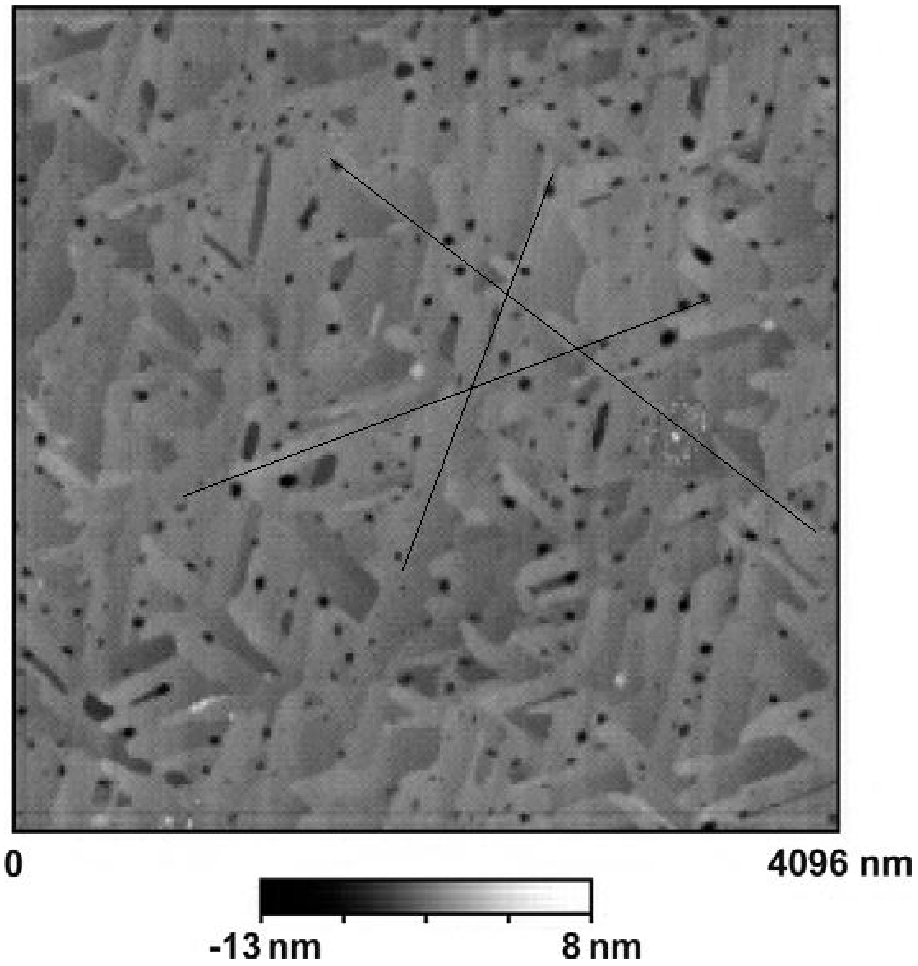

Figure 2.10: AFM image of the α-quartz surface [12]. The black lines indicates the orientations of the domains.

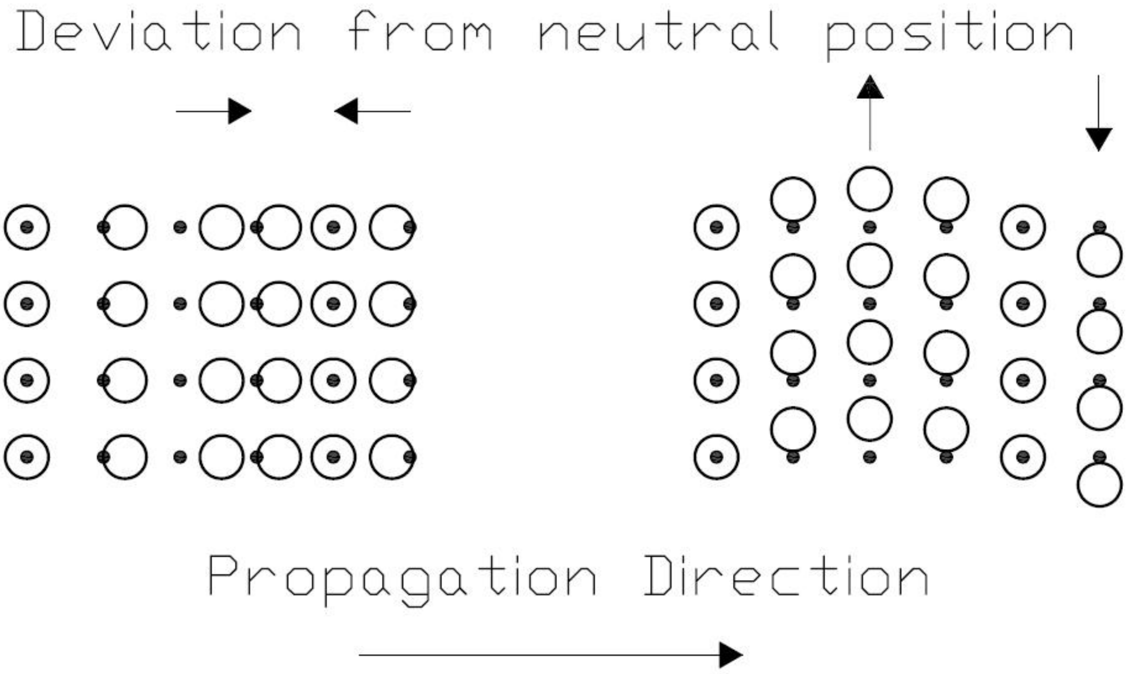

Figure 2.11: Drawing of longitudinal (left) and transversal (right) bulk phonons. The black dots indicate the neutral position and the circles the displacement [33].

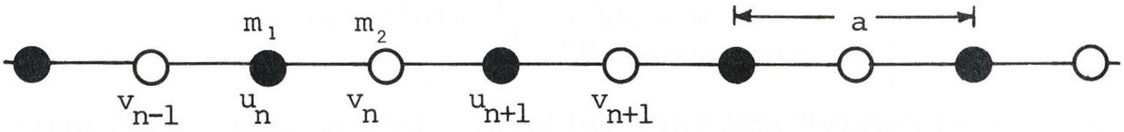

Figure 2.12: Two-atomic one-dimensional structure. The displacements of the heavy atoms m_1 are denoted u_n, and for the lighter atoms m_2 the displacements are denoted v_n. a is the distance from equilibrium [24].

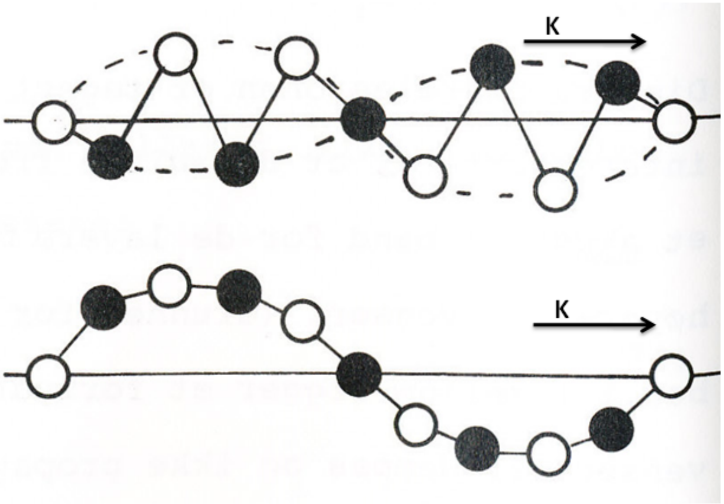

Figure 2.13: Illustration of the particle displacement of the two modes at the same wavelength. **K** is the wave vector. Upper: Transverse optical mode, where both masses in the unit cell oscillate in phase. Lower: Transverse acoustic mode, where both masses in the unit cell oscillate 90 degrees out of phase. Both figures are for a diatomic linear chain. [24].

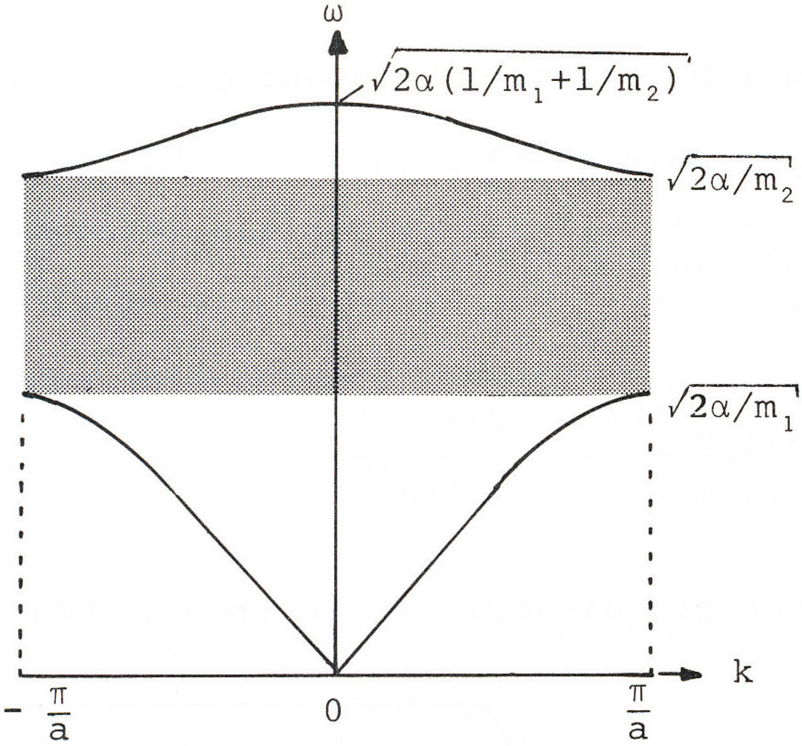

Figure 2.14: Dispersion relation for a diatomic linear chain. The higher branch is the optical branch, and the lower branch is the acoustic. The grey area is the forbidden area. m_1 is the largest mass, m_2 is the smallest mass, a is the inter atomic spacing between to equal atoms, and α is the force constant from Hooke's law [24].

$3p - 3$ optical branches and 3 acoustical branches [27]. Thus quartz (SiO_2), with 3 atoms in the primitive cell, would have 9 branches; 6 optical branches and 3 acoustic.

The common presentation of phonons is with a dispersion curve, where the phonon wave vector is plotted versus the phonon energy/frequency. An example of a surface phonon dispersion curve is given in Figure 2.16.

A crystal lattice exist because there is a stable equilibrium (an energy minimum) between the attractive and repulsive forces acting between the atoms (or ions). In the classical case, all atoms would be at potential minimum at $T = 0$. In close vicinity to the equilibrium, it is possible to develop the potential for the second order. This approximation gives the so called harmonic lattice, which is a lattice where Hooke's law of proportionality between force and fluctuation is valid.

2.4 Helium atom scattering (HAS) from surfaces

De Broglie states that every particle has a wave-like nature. A helium atom with mass m and initial energy E_i , i stands for initial, has therefore a de Broglie wavelength of

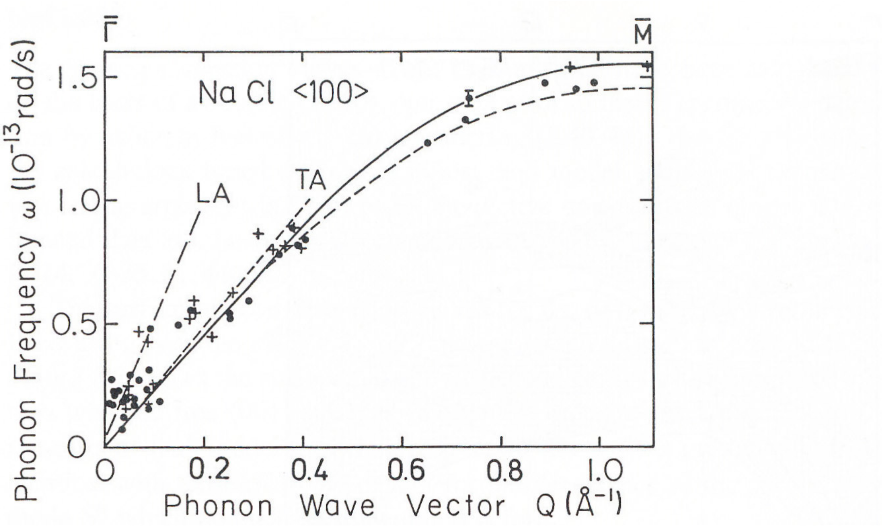

Figure 2.15: NaCl (001). Dispersion of Rayleigh waves. The straight lines indicate the slopes of the longitudinal (LA) and transverse (TA) acoustic bulk modes in the elastic limit. This is measured with inelastic helium atom scattering [34].

$$\lambda_i = \frac{h}{\sqrt{(2mE_i)}}, \tag{2.7}$$

where h is Planck's constant.

When the helium atom hits the surface at an angle θ_i the contribution from the incident wave vector $\mid \vec{k_i} \mid$ is given as

$$\vec{k_i} = \mid \vec{k_i} \mid = \frac{2\pi}{\lambda_i}, \tag{2.8}$$

and, as shown in Figure 2.17, the wave vector can be split into components parallel and normal to the surface. ($\vec{k_i} = (\vec{K_i}, k_{i,z})$ and $\vec{k_f} = (\vec{K_f}, k_{f,z})$. The capital $\vec{K_i}$ denotes the component parallel and $\vec{k_{i,z}}$ denotes the component perpendicular to the surface.)

The commonly used convention for the description of directions, vectors and angles of the scattering process, is described in Figure 2.17. The crystal surface lies in the $x-y$-plane and the normal to the surface is in the z-direction. The incoming and outgoing wave vectors are denoted with $\vec{k_i}$ and $\vec{k_f}$ respectively. $\vec{K_i}$ and $\vec{K_f}$ are the projections of the wave vectors onto the surface plane, and define the azimuthal angles ϕ_i and ϕ_f. If $\phi_i = \phi_f$ we have in-plane scattering, and if $\phi_i \neq \phi_f$ we have out-of-plane scattering [35].

2.5 Elastic scattering of helium on a surface

The Bragg-condition states that the reciprocal lattice vector is equal to the transfer of momentum. For diffraction this means conservation of the momentum parallel to the surface.

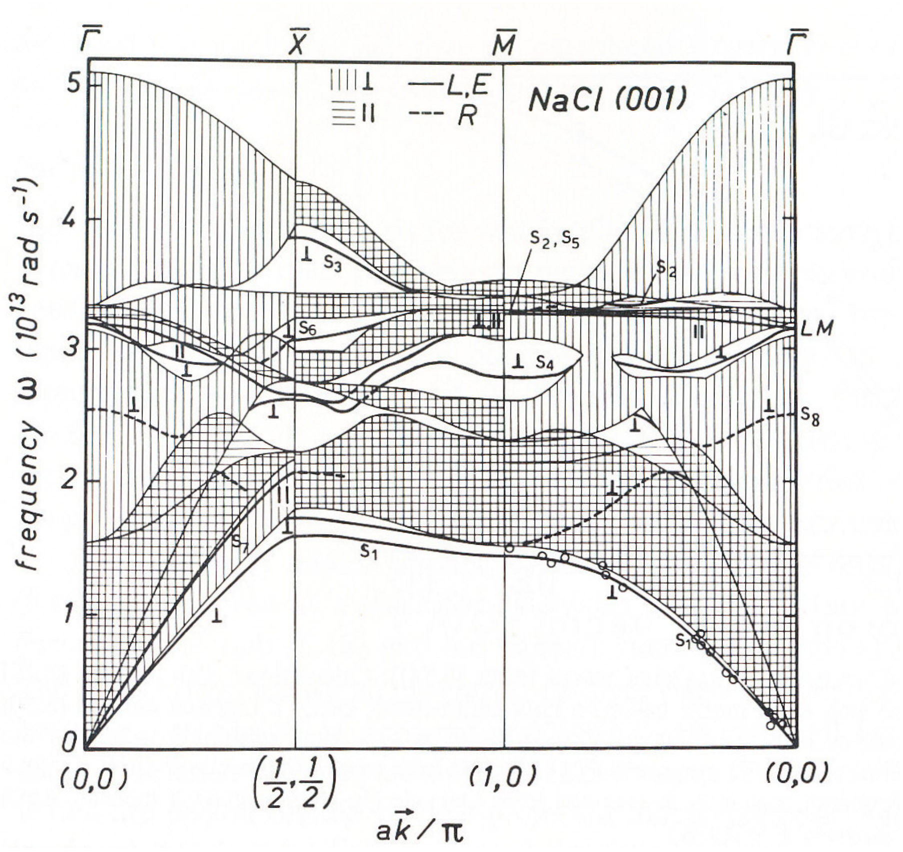

Figure 2.16: Surface phonon dispersion curves. Solid lines: Surface localized modes. Dashed lines: Resonant modes. S_i: Surface localized modes and resonances. Experimental data: Surface modes as determined by helium atom scattering measurements (open circles) [34].

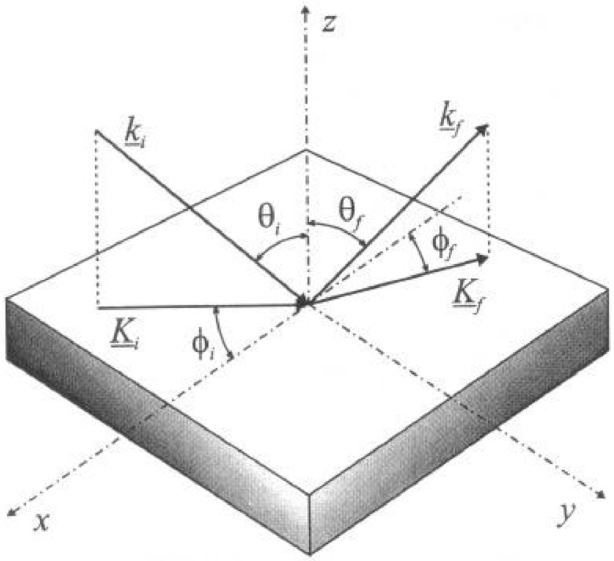

Figure 2.17: Scattering geometry. Both the initial and final wave vector, $\vec{k}_i$ and $\vec{k}_f$, and their corresponding polar angles θ_i and θ_f, have components parallel to the surface plane; $\vec{K}_i$ and $\vec{K}_f$ respectively. The azimuthal angles are denoted by ϕ_i and ϕ_f. [36]

For elastic scattering the equation for momentum conservation is

$$\Delta\vec{K} = \vec{K}_f - \vec{K}_i = \vec{G}_{hk}, \tag{2.9}$$

where h and k are the integers from Equation 2.4. Energy conservation is described by

$$\Delta E = \frac{\hbar^2}{2m}\vec{k}_f^2 - \frac{\hbar^2}{2m}\vec{k}_i^2 = 0. \tag{2.10}$$

Ewald construction

The Bragg condition in Equation 2.9 and the energy conservation in Equation 2.10 can be described graphically with the construction of the Ewald's sphere for diffraction from surfaces, i.e. the construction in two dimensions, as seen in Figure 2.18. Looking at the two-dimensional lattice as a three-dimensional lattice with an infinite lattice vector, $\vec{c} \to \infty$, in the z-direction, gives us an infinitesimal reciprocal lattice vector, $\vec{c}^* \to 0$. That means, for the two-dimensional case the lattice points all lie infinitesimally close along these lines and thus they form rods (vertical lines).

For diffraction experiments, Figure 2.18, the angle between the source and the detector is constant, ($\theta_{QD} = \theta_{SD} = \theta_i + \theta_f$), and the incident angle is changed by turning the sample. Because θ_{SD} is constant, the incident and outgoing wave vectors are related by a fixed angle. Thus if the incident angle, θ_i is changed, both the incident and outgoing wave vector have to be rotated together. This is the circle with radius $\mid \vec{k}_i + \vec{k}_f \mid$ in Figure 2.18. The directions of observable diffraction points

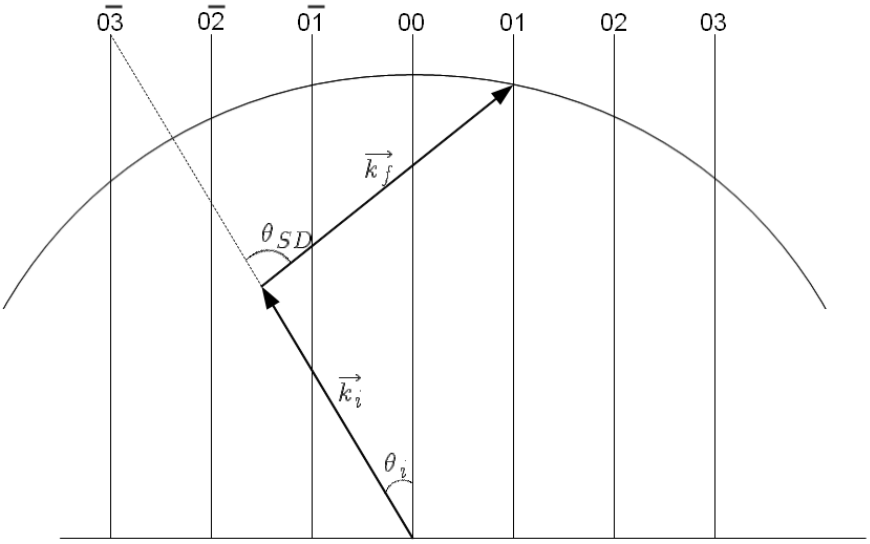

Figure 2.18: Ewald construction with a fixed detector; a so called target scan. θ_i is the angle of the incoming helium beam, θ_{SD} is the angle from the source to detector, for experiments in this thesis: $\theta_{SD} = 90°$, $\vec{k}_i$ is the wave vector of the incoming helium atom, $\vec{k}_f$ is the wave vector of the outgoing helium atom.

are given by the Bragg condition in Equation 2.9. Thus it is the intersection points of the circle and the reciprocal lattice points.

For elastic, in-plane diffraction it is possible to calculate the contribution of the momentum parallel and perpendicular to the surface from Equation 2.9 and 2.10. Parallel:

$$\Delta K(\theta_i) = -2 \mid k_i \mid \cos(\frac{\theta_{SD}}{2}) \sin(\theta_i - \frac{\theta_{SD}}{2}). \tag{2.11}$$

Perpendicular:

$$\Delta k_z(\theta_i) = -2 \mid k_i \mid \sin(\frac{\theta_{SD}}{2}) \sin(\frac{\theta_{SD}}{2} - \theta_i). \tag{2.12}$$

For the special case where $\theta_{SD} = 90°$, Equation 2.11 and 2.12 can be written as Parallel:

$$\Delta K(\theta_i) = -\sqrt{2} \mid k_i \mid \sin(\theta_i - 45). \tag{2.13}$$

Perpendicular:

$$\Delta k_z(\theta_i) = \sqrt{2} \mid k_i \mid \sin(\theta_i - 45). \tag{2.14}$$

Thus for $\theta_{SD} = 90°$, $\Delta K(\theta_i) = -\Delta k_z(\theta_i)$.

The diffraction peaks are defined by two angles, θ_f and ϕ_f (the azimuth angle of the sample). By choosing the azimuth angle corresponding to one of the directions shown in Figure 2.3, Equation 2.4 is reduced to

$$G_h = h\vec{a}_1^* \tag{2.15}$$

or

$$G_k = k\vec{a}_2^*. \tag{2.16}$$

2.6 Inelastic scattering of helium on a surface

Helium atoms impinging on a surface are not only elastically scattered. They can also interact with phonons at the surface, and either gain or lose energy. The most common technique for experimental determination of phonons is the time-of-flight (TOF) technique where short helium pulses are sent to the surface, and then the time t the helium atoms use to travel a length L to the detector is measured. From this it is possible to calculate the average speed $v = \frac{L}{t}$, and from that the energy $E = \frac{m}{2}v^2$, where m is the mass of the helium atom. The beam is split into small pulses by a chopper, and this chopper defines the start time and the start position of the measurement, see Section 4.1.

The simplest case is when the helium atom interacts with a single surface phonon, and the energy exchange happens in a single interaction process. If the interaction happens between several surface phonons it is called a multi-phonon process. For the single phonon process to dominate the multi-phonon process, the Weare criterion [37] must be fulfilled:

$$\beta = \frac{m_{beam} \cdot E_{i,z} \cdot T}{M_{surface} \cdot k_B \cdot \Theta_D^2} \leq 0,01. \tag{2.17}$$

m_{beam} is the mass of a helium atom, $M_{surface}$ is the effective vibrating mass of the surface (for α-quartz, it is found to be 22 a.u. [38]), $E_{i,z}$ is the perpendicular, incident energy, T is the surface temperature, Θ_D is the surface Debye temperature in [38]. It was determined to be 360 K for α-quartz, and k_B is the Boltzmann constant. The small effective surface mass and the low surface Debye temperature, see Section 2.6.1, make it difficult to achieve data without influence from the multi-phonon background [23].

There exists fixed energy and momentum selection rules for transitions from one vibrational state to another, see Equation 2.18 and 2.19.

$$\Delta\vec{K} = \vec{K}_f - \vec{K}_i = \vec{G}_{hk} + \vec{Q} \tag{2.18}$$

$$\Delta E(\vec{Q}) = \pm\hbar\omega(\vec{Q}). \tag{2.19}$$

$\vec{Q}$ is the wave vector of a phonon with frequency ω, K_i and K_f is the momentum of the helium atom before and after transition respectively, $\vec{G}_{hk}$ is the reciprocal lattice vector described in Subsection 2.1.2 and $+\hbar\omega$ and $-\hbar\omega$ are the energies of annihilation and creation of phonons respectively. Combining Equation 2.18 and Equation 2.19 yields

$$\Delta E(\vec{Q}) = \hbar\omega\left(\vec{Q}\right) = E_i\left[\left(1 + \frac{\Delta\vec{K}}{\vec{K}_i}\right)^2 \cdot \left(\frac{\sin(\theta_i)}{\sin(\theta_{SD} - \theta_i)}\right)^2 - 1\right]. \tag{2.20}$$

The usual presentation of phonons is the dispersion curve, where the energy ΔE is plotted vs the phonon vector $\vec{Q}$.

If a particle is scattered at the lattice and gains or loses energy ΔE and momentum $\Delta\vec{K}$ the quantum state transition of the crystal is specified by the wave vector

$\vec{Q}$, and $\Delta\vec{K} = \vec{G}_{hk} + \vec{Q}$. The wave vector, $\vec{Q}$, is usually described in the literature as the crystal momentum. From that, one can think of $\Delta\vec{K} = \vec{G}_{hk} + \vec{Q}$ as a statement that the crystal momentum is conserved only within the reciprocal lattice vector [39]. For visualization of scattering kinematics it is usually more convenient to work with the real momentum change, $\Delta\vec{k}$, rather than the crystal momentum, $\vec{Q}$.

2.6.1 Debye temperature

The Debye theory of a solid is a model for estimating the contribution of phonons to the heat capacity of the solid. In this model, the phonons are treated as quantum harmonic oscillators vibrating in a box. The thermal energy of the solid is given as the integral over spherical coordinates [40]:

$$U = 3\int_0^{n_{max}} dn \int_0^{\frac{\pi}{2}} d\theta \int_0^{\frac{\pi}{2}} d\phi \, \mathrm{n}^2 \sin(\theta) \frac{\epsilon}{e^{(\frac{\epsilon}{k_B T}-1)}}. \tag{2.21}$$

$\epsilon = hf$ is the energy of the different harmonic oscillators, see Equation 2.22, $n = \mid \vec{n} \mid$ is the magnitude of the vector in n-space specifying the shape of the wave, k_B is the Boltzmann constant and T is the temperature of the crystal.

$$\epsilon = hf = \frac{hc_s}{\lambda} = \frac{hc_s n}{2L}. \tag{2.22}$$

h is Planck's constant, f is the frequency different harmonic oscillators, c_s is the specific heat capacity, λ is the wavelength and L is the length of the crystal.

The angular integrals give $\frac{\pi}{2}$, so that Equation 2.21 now is:

$$U = \frac{3\pi}{2} \int_0^{n_{max}} \frac{hc_s}{2L} \frac{n^3}{e^{\frac{hc_s n}{2LkT}-1}} dn. \tag{2.23}$$

Changing the integral variable to

$$x = \frac{hc_s n}{2Lk_B T}, \tag{2.24}$$

and the upper limit then to

$$x_{max} = \frac{hc_s n_m ax}{2Lk_B T} = \frac{hc_s}{2k_b T} \left(\frac{6N}{\pi V}\right)^{\frac{1}{3}} = \frac{T_D}{T}. \tag{2.25}$$

The last equality defines the Debye temperature, T_D. While bulk vibrational properties like the Debye temperature is easily accessible by standard techniques such as X-ray diffraction or neutron diffraction, determination of the surface Debye temperature is usually more difficult. By using helium atom scattering, W. Steurer et al. [38] have managed to find the surface Debye temperature for α-quartz.

Chapter 3

Experimental Setup

This chapter contains a description of the experimental apparatus MaGiE, 'Makroskopische Gitter Experimente', used for the work presented in this thesis. A detailed description of the experimental procedure is also given. Particular emphasize is given to the parts that were developed or improved particularly for this work. The TOF-calibration for the measurements is also included in this chapter. All National Instruments LabView programs used in this thesis were developed by Andreas Apfolter [35].

3.1 General setup

A helium atom scattering (HAS) apparatus has many components, and these are shown in Figure 3.1.

Pure helium gas (purity of 6.0) is used for the creation of an atomic beam in a supersonic expansion from high pressure through a small nozzle, with a diameter of 10 micron, in the source chamber into vacuum. Collisions between the helium atoms inside the nozzle in the forward direction, coupled with the large quantum mechanical energy exchange scattering cross section, serve to reduce the velocity differences in the helium beam leading to a very small velocity spread of $\frac{\Delta v}{v} < 1\%$ [41]. The nozzle temperature, T_N, can be varied. This means that the energy of the helium atoms, and thus the wavelength, can be regulated. By assuming that the helium atoms behave like an ideal gas, the helium energy, E_i is given by

$$E_i = \frac{1}{2} m_{He} v_i^2 = \frac{\hbar^2 k_i^2}{2 m_{He}} = \frac{5}{2} k_B T_N. \tag{3.1}$$

m_{He} is the mass of the helium atom, v_i is the average velocity, $\hbar k_i$ is the momentum and k_B the Boltzmann constant [42]. A nozzle temperature of about 108K, which was used for the measurements presented in this thesis, corresponds to a helium energy of about 23,3meV. All measurements for this thesis were made with a helium pressure of 100 bar. He-atoms expanding from the small nozzle go through a conically shaped skimmer that selects a small part of the expansion region to form a narrow beam. Only a small part of the atoms coming through the nozzle are going through the skimmer. The rest is pumped out of the source chamber by a turbo molecular pump. The skimmer is exchangeable, and for this thesis a skimmer with

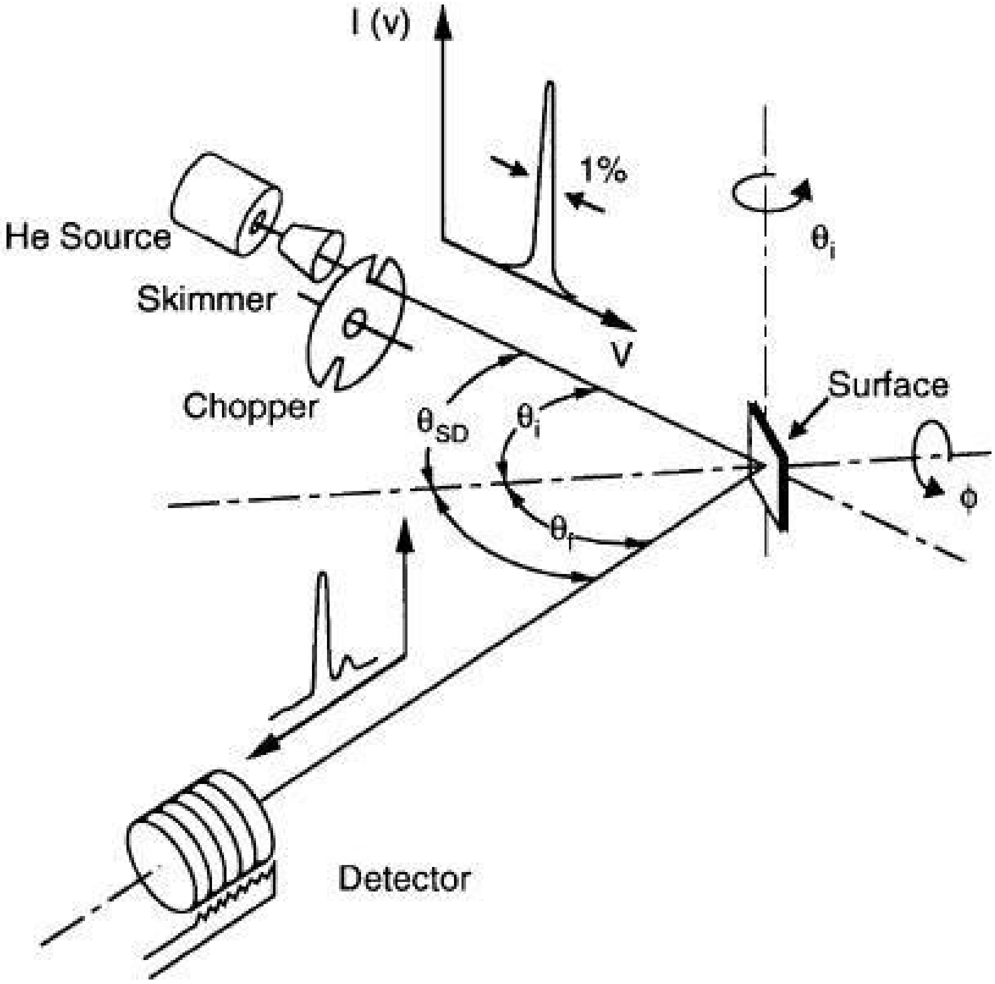

Figure 3.1: Diagram showing the essentials (helium source, skimmer, chopper, investigated sample surface, detector and the angles between source and detector, angle of incoming atom and angle of outgoing atom) of a typical helium atom scattering apparatus. Helium atoms expanding from the high pressure nozzle are collimated and chopped into short pulses. The helium pulses scattered from the surface through a fixed scattering angle θ_{SD} are detected using an electron bombardment detector. The momentum transfer to the surface is varied by changing the incident angle, θ_i of the helium atom beam to the surface. ϕ is the azimuth angle. The velocity spread $\frac{\Delta v}{v}$ of the helium atoms used for the experiments in this thesis was less then 1%. For the experiments performed here, the source detector angle is kept fixed at 90°. [41]

a 400 μm diameter opening diameter was used. The beam then passes through the (differential) pumping stage-1 (DPS-1 in Figure 3.2) and enters the chopper chamber. In this chamber a chopper disc may be inserted into the beam line to cut the beam into short pulses. This is used for time-of-flight (TOF) measurements, see Chapter 4. The next chamber is the target chamber. Here the sample is located on a 360° rotating sample holder. An approximately 4 mm diameter beam hits the sample located in this chamber, under a certain incoming angle. The beam is scattered from the sample into the remaining chambers, which are mounted on a turnable arm with the target chamber as the center of rotation. The angle between the detector and the source chamber, θ_{SD}, may vary between 40° and 190° [35]. At the end of the detector arm, the ionization detector is located. Here the beam is bombarded with electrons to ionize the incoming helium atoms. A magnet is then used for mass selection, and the beam is then focused onto a channeltron detector after that [43].

3.2 Principle of operation

The apparatus used in this the thesis, is a molecular beam apparatus called MaGiE, 'Makroskopische Gitter Experimente'. It was originally developed at the *Max Planck Institute* in Goettingen in the group of Professor Toennies [35]. The apparatus consists of several vacuum chambers, and the pressures in the different vacuum chambers are in the range of 10^{-4} mbar (source chamber) to 10^{-10} mbar (detector chamber) [43]. Figure 3.2 and Figure 3.3 give a scaled view of the instrument. In Figure 3.2 the apparatus is shown in transmission mode, i.e. the angle between the source and the detector, θ_{SD} is 180°. In Figure 3.3 the apparatus is shown in reflection mode (the mode used in this thesis), i.e. the angle between the source and the detector, θ_{SD} is 90°.

The apparatus consist of five main chambers [35]:

- The *source chamber* is the first part of the apparatus. It is used for the creation and first collimation of the helium beam down to a diameter of around 1 mm hitting the sample.

- The *chopper chamber* together with the *iris chamber* follows the source chamber. In this chamber the beam may be chopped, and a further adjustable collimation of the beam can be done with the iris (from 0,6 mm to 5 mm). Chopping means that the beam is split into small pulses by a chopper. For the study of phonons, the inelastic scattering of helium atoms, an energy analysis of the scattered atoms has to be made. This is done through time-of-flight (TOF) measurements. The basic principle of TOF is to measure the time t the particle has used to travel a length L. We assume it travels with constant speed from the chopper to the detector. $v = \frac{L}{t}$, see Section 4.1.

- In the *target chamber* one has the possibility to place different targets in the beam line. For the work presented in this master thesis, the target is a 10 mm × 10 mm × 1 mm α-quartz crystal.

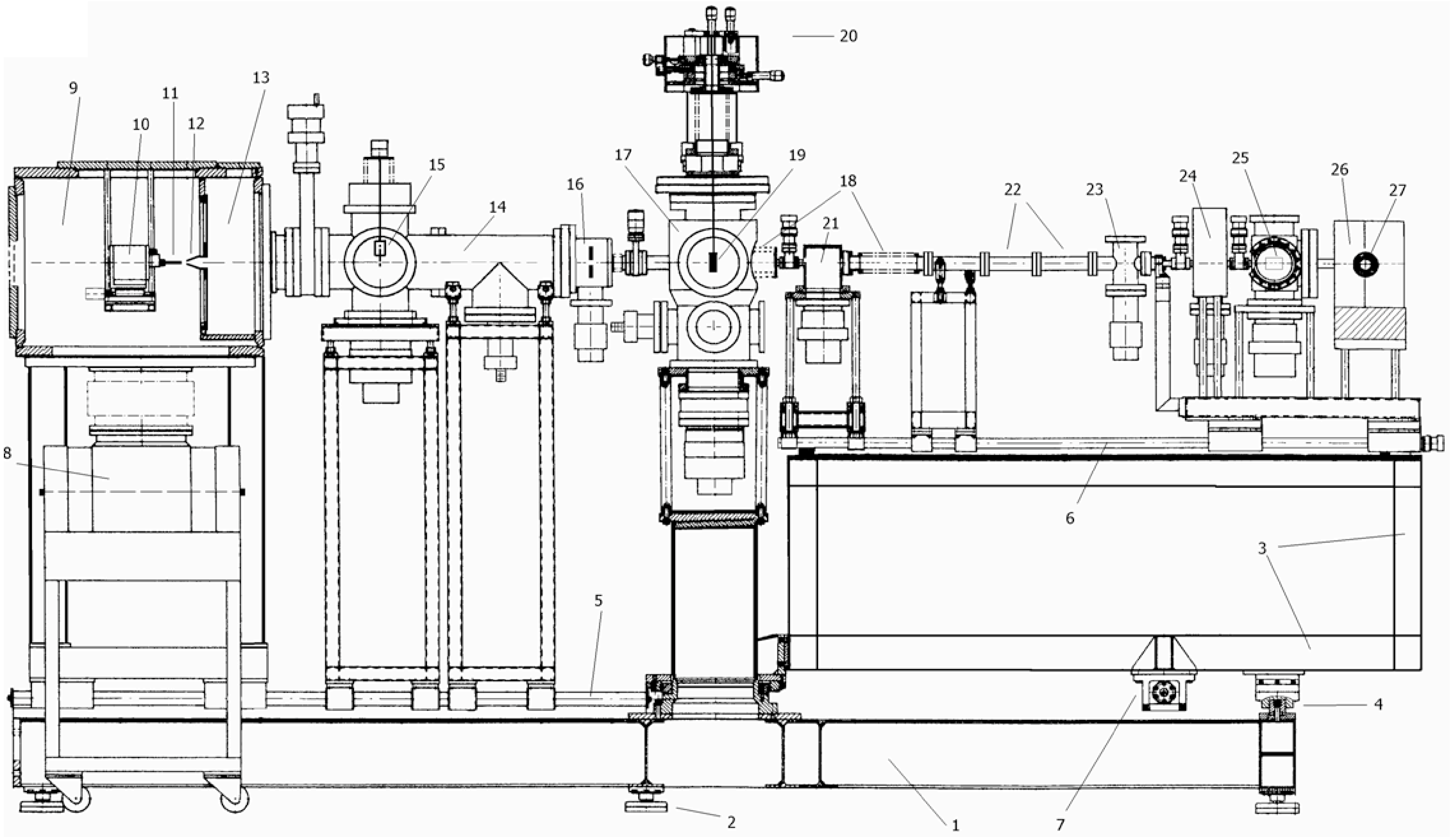

Figure 3.2: Scaled side view diagram of the apparatus. The source-detector angle $\theta_{SD} = 180°$. (1) Mounting basis. (2) Damping feet. (3) Detector arm. (4) Circular guiding rail for the detector. (5) Linear guiding rail for the source chamber. (6) Linear guiding rail for the detector. (7) Placement for the electro engine for the detector arm movement. (8) Source chamber turbo molecular pump. (9) Source chamber (QK). (10) Position system for the nozzle. (11) Nozzle. (12) Skimmer. (13) Differential pumping stage, 1 (PST-1). (14) Chopper chamber (CK). (15) Chopper. (16) Iris chamber and iris (IK). (17) Sample chamber(SK). (18) Ultra High Vacuum Membrane bellow. (19) Sample holder. (20) Sample manipulator. (21) Differential pumping stage, 2 (PST-2). (22) Space for the mounting of an additional pumping stage. (23) Differential pumping stage, 3 (PST-3), not used for the measurements presented in this thesis. (24) Piezo chamber (PIE). (25) Detector chamber (DK). (26) Electromagnet. (27) Channeltron [36].

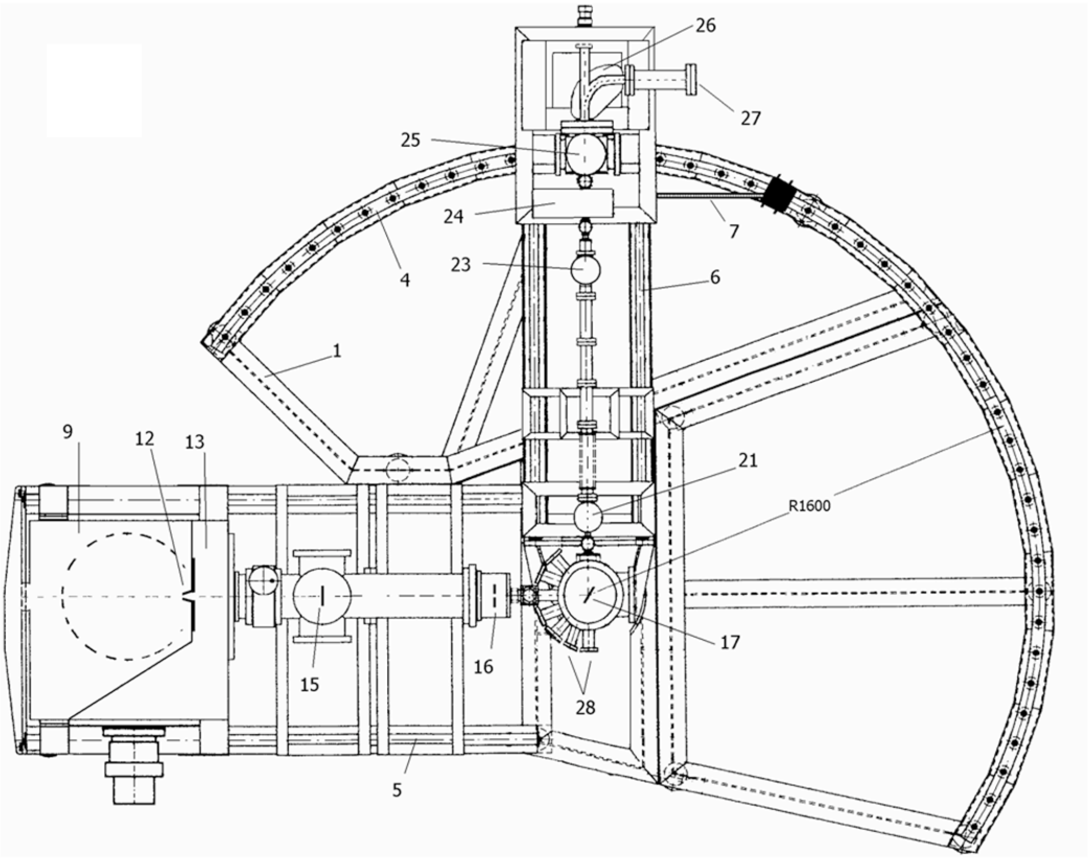

Figure 3.3: The apparatus is shown in the configuration used for these experiments with the angle between the source and detector, $\theta_{SD} = 90°$. (1) Mounting basis. (4) Circular guiding rail for the detector. (5) Linear guiding rail for the source chamber. (6) Linear guiding rail for the detector. (7) Placement for the electro engine for the detector arm movement. (9) Source chamber (QK). (12) Skimmer. (13) Differential pumping stage, 1 (PST-1). (15) Chopper. (16) Iris chamber and iris (IK). (17) Sample chamber(SK). (21) Differential pumping stage, 2 (PST-2). (23) Differential pumping stage, 3 (PST-3), not used for the measurements presented in this thesis. (24) Piezo chamber (PIE). (25) Detector chamber (DK). (26) Electromagnet. (27) Channeltron. (28) Beam inlet flanges [36].

- The *piezo chamber* is used in particular for atom optics experiments. This is not relevant for the work presented in this thesis.
- In the *detector chamber* the helium atoms are detected using an electron bombardment detector.

3.3 Preparation of Experiment

Some improvements on the operation of MaGiE were developed as part of this thesis. This includes calibration of the angular decoder and TOF-measurements, venting procedures, a new sample holder and the cleaning process of the sample.

3.3.1 Calibration of angular decoder

The angular decoder is a readout system, which reads out the angular position of either the target and/or the detector. The LabView program for reading out the position of the target, *Read Current Position*, contained a bug, so a new procedure for calibration of the angular decoder was developed.

1. Turn sample holder to approximately 180°.
2. Vent the target chamber. See Section 3.3.2
3. Measure the distance between the left and right side of the sample holder to the flange (at 180° these should be equal).
    - The angle of the sample holder, Θ, is given as

      $$\Theta = \Theta_0 + N\frac{\Delta\Theta}{\Delta N} + WG\frac{\Delta\Theta}{\Delta WG}. \tag{3.2}$$

      Θ_0 is the angular offset, N counts the complete number of turns of the angular decoder, ($N\epsilon[-2, 2]$), $\frac{\Delta\Theta}{\Delta N}$ is the ratio between the gear of the angular decoder and the gear of the manipulator, WG is the angular position and $\frac{\Delta\Theta}{\Delta WG}$ is the resolution of the angular decoder.
4. Un-tighten the screws that are keeping the angular decoder in place.
5. Turn angular decoder by hand until the program *Read Current Position* shows 180°. For that you might need to change N and/or Θ_0. This is done in the program called *DriveGlobals.vi*, see Figure 3.4.
6. Tighten the screws on the angular decoder.
7. If the tightening of the screws changed the angular offset, Θ_0, the offset has to be changed again.

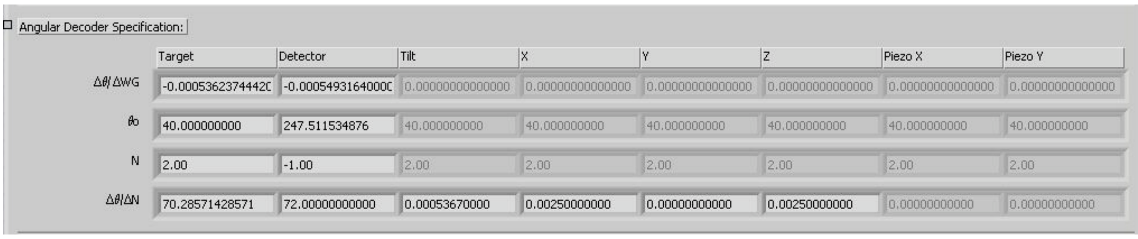

☐ Angular Decoder Specification:

	Target	Detector	Tilt	X	Y	Z	Piezo X	Piezo Y
Δθ/ΔWG	-0.0005362374442C	-0.0005493164000C	0.0000000000000	0.0000000000000	0.0000000000000	0.0000000000000	0.0000000000000	0.0000000000000
θ0	40.000000000	247.511534876	40.000000000	40.000000000	40.000000000	40.000000000	40.000000000	40.000000000
N	2.00	-1.00	2.00	2.00	2.00	2.00	2.00	2.00
Δθ/ΔN	70.28571428571	72.00000000000	0.00053670000	0.00250000000	0.00000000000	0.00250000000	0.00000000000	0.00000000000

Figure 3.4: Screen shot of the program *DriveGlobals.vi.* Θ_0 is the angular offset, N counts the complete number of turns of the angular decoder, ($N\epsilon[-2,2]$), $\frac{\Delta\Theta}{\Delta N}$ is the ratio between the gear of the angular decoder and the gear of the manipulator, WG is the angular position and $\frac{\Delta\Theta}{\Delta WG}$ is the resolution of the angular decoder.

3.3.2 New venting procedure for target chamber

The old venting procedure was designed for an oil based pre-vacuum pump. It was then important to avoid getting oil into the vacuum chambers. The old turbo pump corresponding to the target chamber did not tolerate to be turned off and on frequently, and when it had been turned off, it took quite some time before it could be turned on again, and therefore the venting of the target chamber was performed with a running turbo pump. In the new setup, an oil-free pre-vacuum pump[1] and a new turbo molecular pump[2] were installed, so a new, faster venting procedure for the target chamber was introduced. This venting procedure requires the turbo pump connected to the target chamber to be turned off. The components referred to are indicated in Figure 3.5.

Venting the target chamber with the turbo pump turned off

1. Close the valves to the chambers neighboring the mirror chamber; **PST2-V** and **SK-V**.

2. Write down the pressures in the mirror chamber and as well as the ones for the neighboring chambers.

3. Move sample holder in correct position.

4. Turn of the high voltage pressure measurement gauges for the mirror chamber; **PSK**.

5. Turn of the surveillance system for **SK-Electronic** (red button). Turn of FUG POWER SUPPLY **NTN 140-12.5**, Rack 4.

6. Close the pre-vacuum valves **SK-VV1a** and **Sk-VV1b**.

7. Turn of surveillance **SK-TURBO** (red button), Rack 1, LT3.

---

[1] oerlikon, leybold vacuum, SCROLLVAC SC 5D, pumping volume of 19 l/min, end pressure < 0,05mbar

[2] Pfeiffer Vacuum, TC600

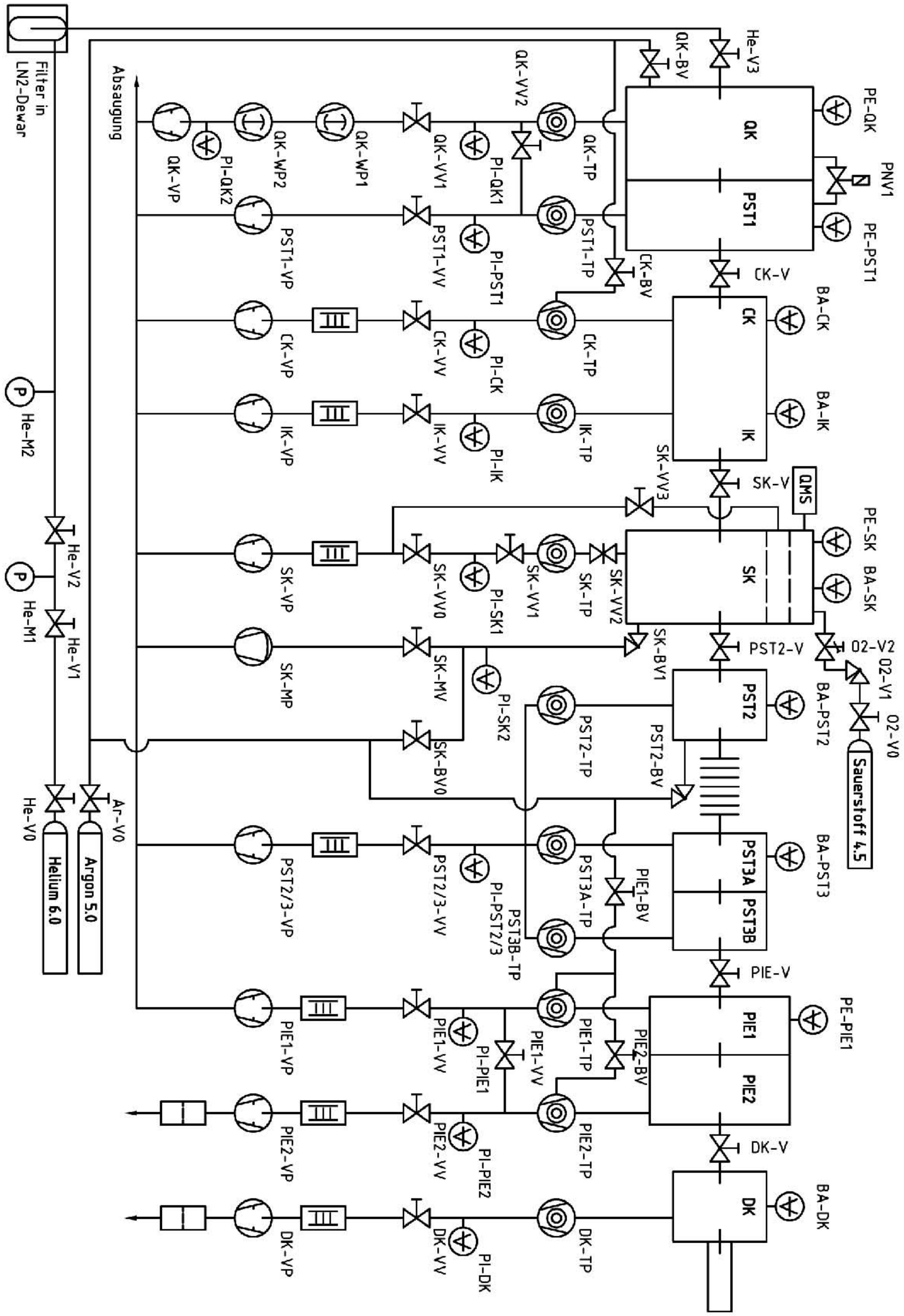

Figure 3.5: Vacuum setup plan of the apparatus [35].

8. Close the water cooling valve **SK** on Magie.
9. Turn of the turbo pump **SK-TP**, Rack 4.
10. Wait around 15 minutes for the turbo pump to slow down.
11. Open the clamp of the **pi-SK2** pressure gauge.
12. Check that there is some pressure on the measurement gauge of the argon outlet.
13. Open the valve **SK-BV1** slowly ($\sim$ 3-4 turns).
14. Open the venting valve **SK-BV0** slowly. Vent the pipes with small ”shots” of argon. The **pi-SK2** pressure gauge will fall of when finished.
15. Close valve **SK-BV0** and fix the clamp of the **pi-SK2** pressure gauge.

Pumping the mirror chamber with the turbo pump turned off

1. Check that **SK-VV1a** and **SK-VV1b** are closed.
2. Check that **SK-BV1** and **SK-BV0** are closed.
3. Turn on the oil-free pre-vacuum pump **SK-KP**, Rack1, LT3.
4. Slowly open both valves **SK-VV1a** and **SK-VV1-b** simultaneously.
5. Check pre-vacuum pressure **PI-SK-1**, Rack 4. When the pre-vacuum pressure is less then 10^{-1} mbar, start the target chamber turbo pump **SK-Turbo**, Rack 1, LT3.
6. Press also the on-button on **SK-TP**, Rack 4.
7. Check that the pre-vacuum pressure is still going down, and that the frequency of the turbo pump is going up.
8. When the frequency of the turbo pump is 833Hz, turn on the on the surveillance **SK-TURBO** (red button), Rack 1, LT3.
9. Turn then on the high voltage pressure measurement gauges for the mirror chamber (**PSK**) once the turbo pump has full speed.

3.3.3 Sample holder

During the move from Graz to Bergen, the previously used sample holder could not be brought along, and therefore a new sample holder was designed for this thesis. The sample holder had to have the option of both heating and cooling the sample, and it also had to be thermally isolated from the MaGiE-system. A drawing of the sample holder can be seen in Figure 3.6.

The body of the sample holder is made of stainless steel, and it is mounted directly onto the MaGiE-system. This means that if the sample would be mounted

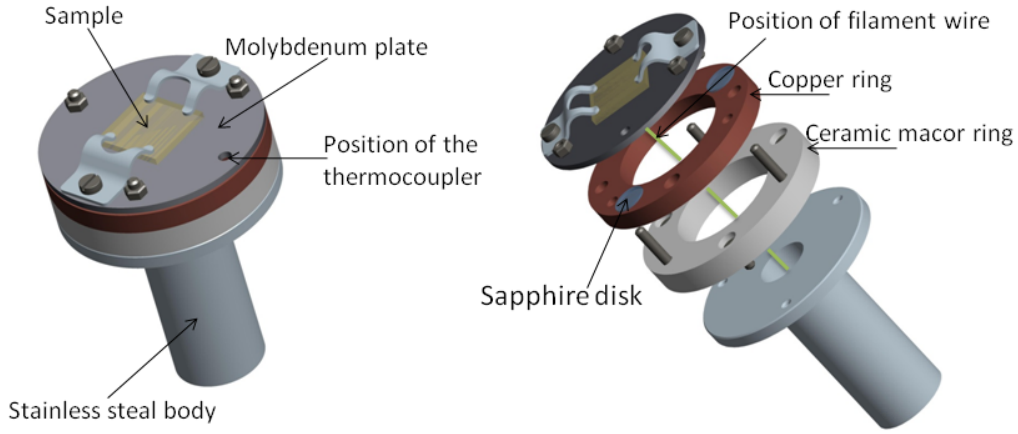

Figure 3.6: Drawing of the sample holder.

directly on the sample holder, it would not be possible to temperature treat the sample without any influence on the entire system. In order to isolate the temperature changes, a ceramic macor spacing ring is placed on top of the sample holder. A copper ring is mounted on the top of this macor ring. Copper braids are connected from the copper ring to a liquid nitrogen cooling system. On top of the copper ring, three small sapphire discs are mounted. These work as spacers to the plate made of molybdenum, which has a good heat transfer coefficient for both high and low temperature, mounted on top of them. A sample is then mounted on the molybdenum plate used for heat transfer from the filament to the sample. Sapphire has very good energy transfer properties for low temperature, but it is fairly bad for transferring energies at high temperature. This means that during the heating process, there is a temperature isolation between the molybdenum plate and the copper ring. The filament is placed on the back of the molybdenum plate, and therefore all the heat is transferred from the filament through the molybdenum plate onto the sample. In the case of cooling the sample, the heat transfer is from the copper ring via the sapphire discs onto the molybdenum plate and further to the sample. In this way it is ensured that the proper cooling from the liquid nitrogen down to 90 K and heating through radiation from the filament up to 650 K can be done.

For temperature measurements, a K-type thermocouple is spot welded onto the molybdenum plate, as Figure 3.6 shows. For several reasons, like for example a fast mounting procedure of the sample and to not cover parts of the investigated surface, the temperature is regulated with a PID-controller at this fixed position on the molybdenum plate. Because the temperature measured is the temperature of the plate, and not the sample, a temperature calibration is necessary.

Mounting of sample holder

The mounting and de-mounting procedure for the sample holder is explained in Appendix C in [35].

3.3.4 Sample preparation

The α-quartz sample used was prepared in *Laboratoire Surface et Interface du Verre, Saint Gobain Recherche*, Aubervilliers, France. First it was cleaned in a soap solution (Alcanox) and then cleaned with three baths of deionized water. A diamond polish with 0,5 μm diamond powder was then made, in the end and a heat treatment under pure O_2 atmosphere at 1,1 atm at 1050° for 120 hours. It was sent to Bergen in a transport box filled with a slight overpressure of argon. After thoroughly cleaning the outside of the transport box, it was placed in a glove bag. Then the glove bag was fitted to the target chamber flange and sealed with tape. The flange of the target chamber was opened after filling the glove box with argon, the sample holder demounted and the transport box opened. The quartz-sample was then transfered on the sample holder, and the sample holder mounted back into the target chamber.

3.3.5 Cleaning the sample with O_2

Previous X-ray photo electron spectroscopy (XPS) experiments done at Saint Gobain [44] showed that most of the contamination on the surface of quartz and silicas, when kept in air, is due to carbon compounds. Elin Søndergård and Anne Lelarge at Saint Gobain developed a cleaning method for the quartz and silica surfaces: Heating the sample and simultaneously flushing it with high partial pressure of oxygen. The idea is that a high partial pressure of oxygen combined with heating can remove the hydrocarbon compounds in a controlled burning process.

A higher partial pressure of oxygen also increases the total pressure in the vacuum chamber. This leads to a higher load on the turbo pump, which again may lead to a higher back diffusion of hydrocarbons. To maintain the lowest total pressure possible in the target chamber, together with a high partial pressure of oxygen around the sample, a micro diffuser was made at Saint-Gobain Recherche, Aubervilliers, France. The micro diffuser is, together with a regulation valve, mounted on a linear translator. The linear translator is then mounted on the inlet flange on the target chamber. By turning the sample holder to the desired position ($\theta = 11°$), the end part of the micro diffuser may be moved via the linear translator (2 on Figure 3.7) towards the quartz sample. The final distance between the sample and the micro diffuser should be around 1 mm. One can monitor the movement of the micro diffuser through one of the other inlet flanges in the mirror chamber. It is now possible to flush the sample with a nearly homogeneous and laminar flow of O_2 [35].

Cleaning procedure

Before the start of the cleaning, the Bayert-Alpert pressure measurement gauge of the mirror chamber must be deactivated. The Bayert-Alpert pressure measurement

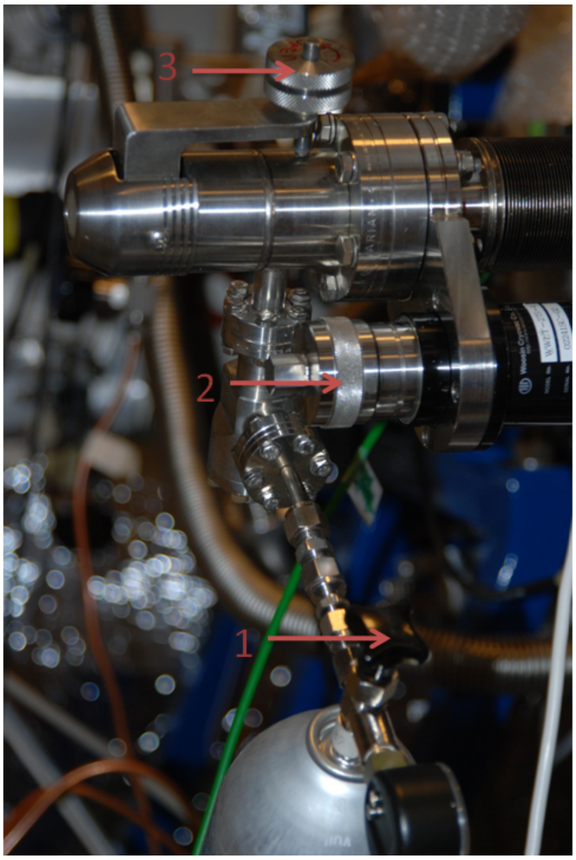

Figure 3.7: The linear translator mounted on MaGie. 1 is the valve on the O_2-bottle, 2 is the positioning wheel of the linear translator for adjusting the distance between the micro diffuser and the sample and 3 is the leak valve for accurate adjustment of the oxygen flow.

gauge works on a basis of a heated filament. The heated filament emits electrons that ionize the helium atoms. The ions are then gathered by a collector and the current is a function of the pressure. The material the filament is made of oxidizes easily, and will therefore be damaged when exposed to oxygen. That is also the same reason for turning off the Bayert-Alpert gauge before venting a chamber.

The cleaning process takes place with the turbo pump turned on. First open the valve on the O_2-bottle[3] (1 on Figure 3.7. Valve 3 on Figure 3.7 may then be opened. Before valve 3 is approximately half open, no O_2 will enter the chamber. When oxygen starts flowing, the pressure will suddenly rise. Pay close attention to the display PSK on Rack 4. The pressure should be in the range of $10^{-4} - 10^{-5}$ mbar during the cleaning. The heating of the sample may now start. To prevent too much tension on the sample, the heating temperature should not rise faster then 200 K/h.

The optimal temperature for the cleaning process is 650 K [35]. This corresponds to a heating current of around 6 A and a heating voltage of 10.6 V. The heating should be at 650 K for two to three hours. Then the heating can be turned slowly down, and the oxygen regulation valve may be closed.

To get a proper signal after the heating and flushing of $\mathrm{O_2}$, the sample has to be cooled down, and then heated again, but this time without $\mathrm{O_2}$-flushing.

3.4 Time-of-flight (TOF) preparation

The principle of the TOF-measurements is treated in Section 4.1. In this section the technical details and the calibration are discussed.

3.4.1 Time-of-flight

The continuous helium beam can be parted into small pulses by a chopper. The mechanical chopper used for the experiments in this thesis consists of a 0,1 mm stainless steel chopper disc with two trapezoidal shaped slits, see Figure 3.8. This is turned by an electrical motor. The vertical chopper position may be changed manually to use different widths of the slits for different energy resolutions. For a more detailed explanation, see [35]. A program, controlled by the computer, is triggered with a LED and a photo detector every time a He-pulse is coming through the chopper. This program starts accumulating the counts in certain time-bins corresponding to the arrival time to the detector. The slit width, the number of bins $N_{channel}$, the measurement time and the delay time are all set before the experiment [36].

Figure 3.9 shows an example of a TOF-spectrum.

3.4.2 TOF-calibration

The time-of-flight module gives the output as an intensity count for a certain measurement time, t_m, that sums up the single TOF-spectra recorded one after another

---

[3] Linde minican, Gase fürs Labors, $\mathrm{O_2}$ Sauserstoff. Purety 4.5. 12l

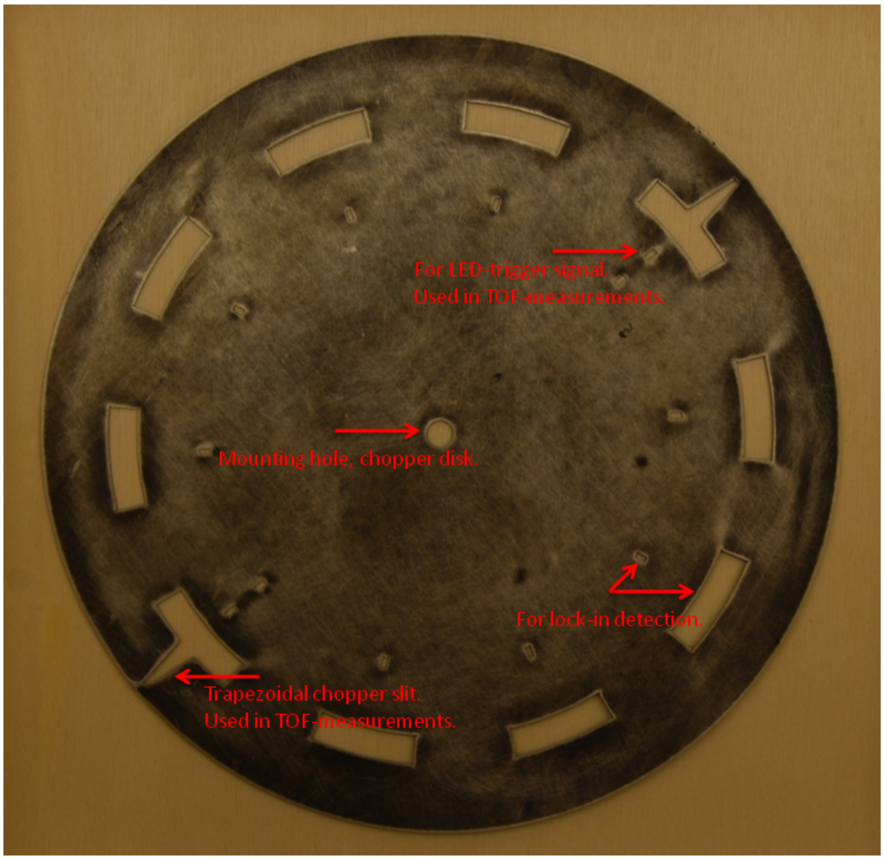

Figure 3.8: The 0,1 mm stainless steel chopper disc.

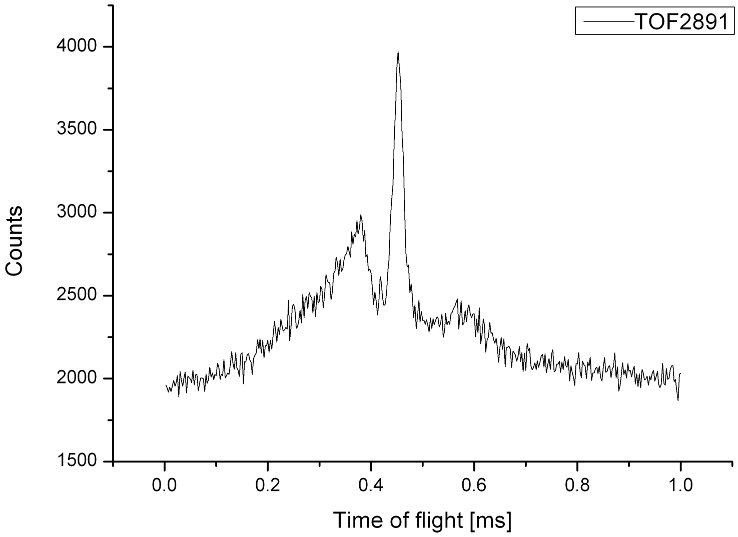

Figure 3.9: Time-of-flight spectrum before the corrections from Equation 3.3 have been included. Temperature nozzle: $T_N = 108K$. Temperature sample: $T_S = 300$ K. Pressure helium: $p_0 = 100bar$. Number of channels: $N_{channel} = 400$. Channel width: $t_{channel} = 2.5\ \mu s$. Delay time: $t_d = 1400\ \mu s$. Measurement done by Katrin Fladischer.

in a predefined time-interval, channel width, $t_{channel}$. When the beam line is open, a trigger signals the start of the recording of channels after a preliminary chosen delay time, t_d. This delay time corresponds to the time the particles, with an energy E_i, use to reach the detector. The actual flight time t_f of the He-pulse starting at the chopper, and the maximum of the Gaussian time distribution, is made up by the previously mentioned delay time and channel width, the peak time t_p and a correction time t_c [35]:

$$t_f = t_d + t_p - t_c - \frac{t_{channel}}{2}. \tag{3.3}$$

The correction time, t_c, is a combination of three parts, $t_c = t_1 + t_2 + t_3$:

1. t_1: The trigger signal. The photo diode is always triggering to early $\Rightarrow t_1 < 0$.

2. t_2: The photo diode is not perfectly aligned with the slit; it has an offset. This means that depending on the direction of rotation t_2 can be either negative or positive.

3. t_3: In principle a perfect slit opening would be a straight line. That is not possible because not enough signal would go through. Even with no offset due to the trigger there still is a time offset caused by the slit opening. This means that $t_3 < 0$ for both negative and positive directions of rotation.

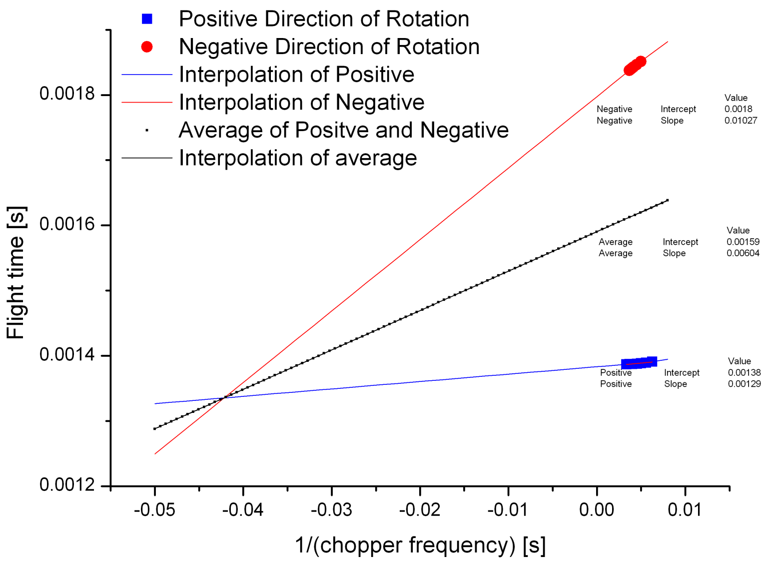

Figure 3.10: Flight time, t_f, corresponding to the inverse chopper frequency $\frac{1}{\upsilon_{chopper}}$ for negative and positive direction of rotation. The average slope of the positive and negative rotation corresponds to t_1; the early trigger signal. Temperature nozzle: $T_N \approx 110$ K. Temperature sample: $T_S < 130$ K. Pressure helium: $p_0 = 100$ bar. Number of channels: $N_{channel} = 400$. Channel width: $t_{channel} = 2.5\ \mu s$. Delay time, negative rotation: $t_d = 1400\ \mu s$ and delay time, positive rotation: $t_d = 900\ \mu s$. Files used for the negative direction of rotation: TOF2804.dat - TOF2809.dat. Files used for the positive direction of rotation: TOF1990.dat - TOF1996.dat. Measurements done by Katrin Fladischer.

Experiments have shown that $| t_1 | > | t_2 | >> | t_3 |$, and this is the reason for the negative sign for t_c in Equation 3.3.

t_c is dependent on the chopper frequency, $\upsilon_{chopper}$, and may be found experimentally by plotting the elastic peak time versus the inverse chopper frequency, see Equation 3.4 and Figure 3.10.

$$t_c = \frac{\alpha}{\upsilon_{chopper}}. \tag{3.4}$$

$\alpha = 0.01027$ for the negative rotation of the chopper disc used for this thesis, see Figure 3.10.

The channel width is predefined and it has only a small influence on the real time. For each measurement value in the TOF-spectrum the count rate value is output together with the end of the corresponding channel interval. To center the count rate with respect to the corresponding channel interval, half of the channel time interval needs to be subtracted. Thus the real flight time, t_f, for TOF2826.dat in Figure 3.11, is

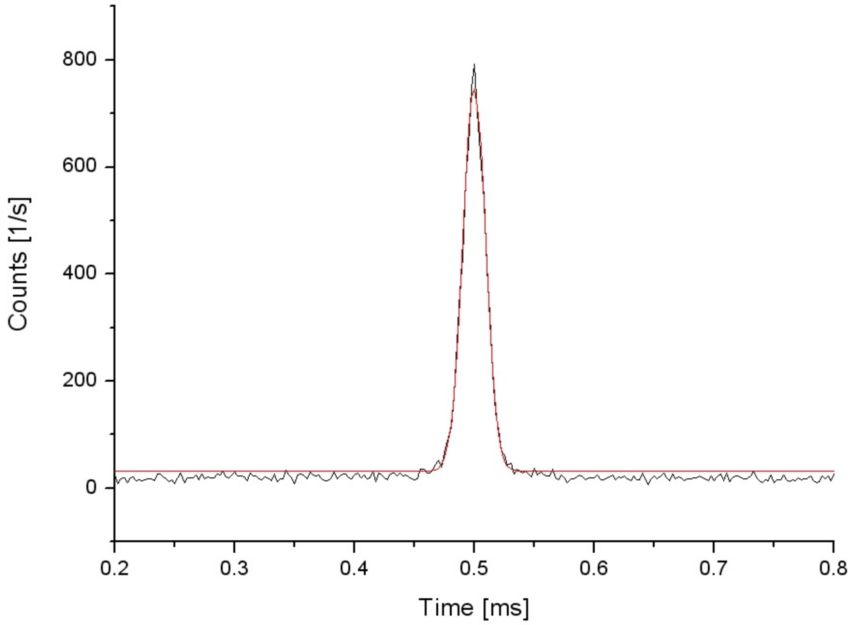

Figure 3.11: Flight time spectrum of the elastic peak (TOF2826.dat). Incident angle: $\theta_i = 42,6°$, the angle between the chopper and detector: $\theta_{SD} = 90,1°$, $p_0 = 100$ bar, $T_N = 102.7$ K, $T_S = 302$ K, $t_d = 1400\ \mu s$, $t_m = 10$ s, $\upsilon_{chopper} = 271$ Hz. From the Gaussian fit: $t_p = 0,4995$ ms. Measurement direction in real space: R(1,0). Measurement done by Katrin Fladischer.

$$t_f = 1,400ms + 0,4995ms - \frac{10,27\frac{ms}{s}}{271Hz} - \frac{0,0025ms}{2} = 1,860ms. \tag{3.5}$$

3.4.3 Angle calibration

There is an offset between the real angle of the sample and the angle given in the LabView program (*TargetScan*) used for turning the sample holder. The angle of the incoming beam must therefore be corrected. This is done with the corresponding ScanLine-file (.SCNL). A scan line gives the diffraction pattern of helium atoms on the quartz surface by turning the sample from 0° to 90°, see Figure 3.12. First find the middle of the specular peak with a Gaussian fit as shown in Figure 3.13. The specular peak should be at 45°, so by subtracting the fitted peak value to 45°, the offset is found. This offset is then added to the angle of the sample holder to get the real angle.

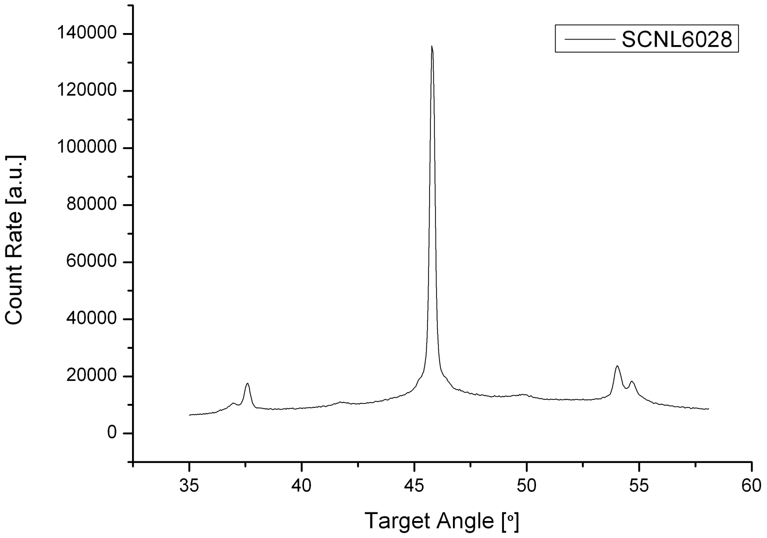

Figure 3.12: In-plane helium atom diffraction spectrum of the α-quartz crystal in the $\Gamma\vec{M}$-direction. SCNL6028.txt. The specular peak is in the middle, and the two side peaks on ≈ 37° and ≈ 54° are the first order peaks. See Chapter 5. $p_0 = 100$ bar, $T_N = 108$ K, $T_S = 302$ K, $t_d = 1400$ μs, $t_m = 10$ s, $\upsilon_{chopper} = 272$Hz. Measurement direction in real space: R(1,0). Measurement done by Katrin Fladischer.

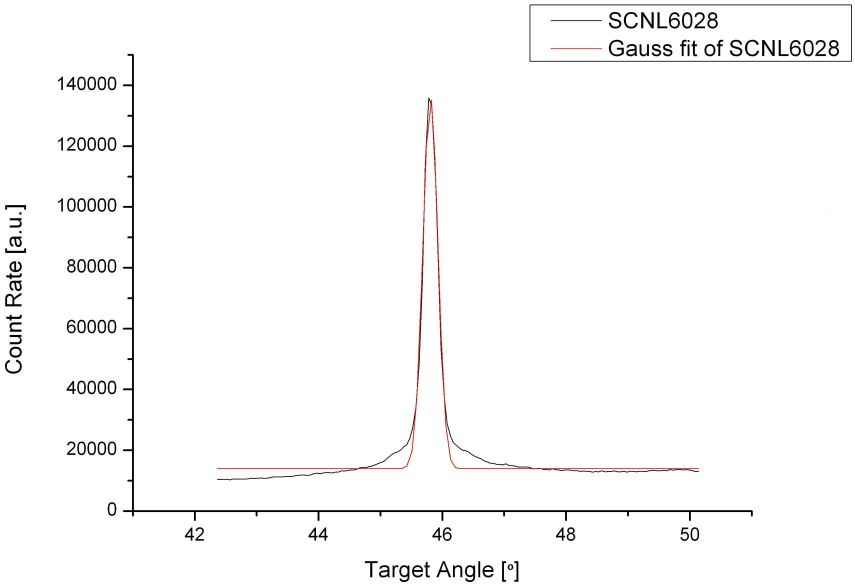

Figure 3.13: Gaussian fit of the specular peak from SCNL6028.txt. The Gaussian fit gives a specular peak of 45,8065°, which means that the offset in this case is 0,8065°.

Chapter 4

Measuring surface phonons

In principle the HAS-experiments are performed with a setup as shown in Figure 4.1. For a more detailed description see Chapter 3. An almost monochromatic beam of He-atoms (the velocity spread for the measurements performed here was less than 1%) is sent onto a surface at a fixed angle of incidence. The scattered beam intensity is then measured at a given reflection angle. As stated in Chapter 2, He-atoms may be scattered either elastical or inelastical. To measure the inelastic scattered atoms, an energy analysis of the beam has to be made. The most commonly used technique is the time-of-flight (TOF) analysis. The He-beam is divided into small pulses and the detected atoms are recorded with time resolution. When the He-atoms are scattered off the sample, the inelastic scattered atoms will gain or lose energy, and will hit the detector before or after the elastic scattered atoms respectively. By varying some of the parameters (like beam energy or incident angle) it is possible to sample different transfer values of energy and momentum [39]. Single phonon processes lead to narrow peaks in the TOF-spectrum. In contrast, multi-phonon processes give broad structures, and this hampers the extraction of single phonon peaks.

4.1 Time of flight (TOF)-measurement

The basic principle is to measure the time t the particle has used to travel a length L to get the average speed, $v = \frac{L}{t}$, and then get the energy, $E = \frac{m}{2}v^2$, where m is the mass of the particle. The beam is split into small pulses by a chopper, and this chopper defines the start time and the start position of the measurement. As illustrated in Figure 4.2, during the propagation towards the detector, the packages are getting broader because of the different energies of the individual particles.

The particles with the higher energy will hit the detector first. If now the progress of the detected intensity$I(t)$ is plotted over time, it is possible to determine the velocity and energy distribution of the particles. To get a sufficient intensity, the measurement is repeated and added: $I(t) = \sum_i I(t)$. The form of the beam packages is described by the chopper transmission function, $C(t)$, and the intensity measured by the detector is a convolution between the chopper transmission function and the real intensity, $i(t)$:

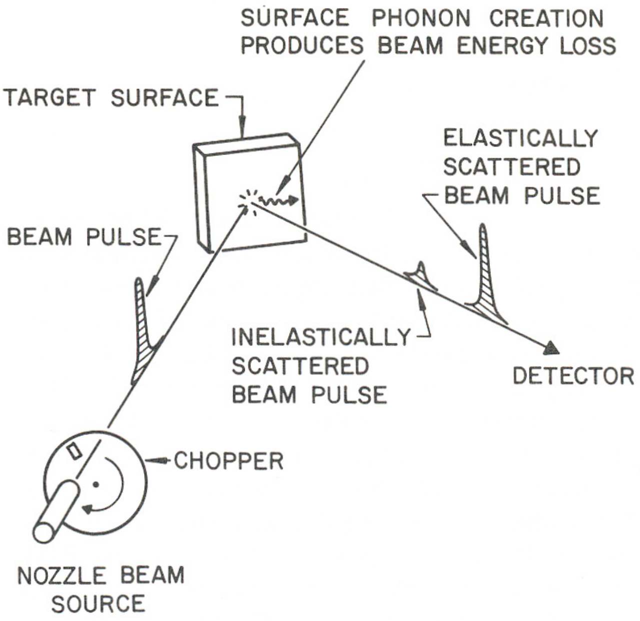

Figure 4.1: Schematic illustration of the measurement of surface phonons using inelastic helium atom scattering with time-of-flight-analysis. [39]

$$I(t) \propto \int_{-\infty}^{\infty} C(t-\tau) i(t) d\tau. \tag{4.1}$$

But also the detector has an influence on the intensity. The ionization of particles happens within an ionization length of L_D which leads to a location dependent ionization probability, $D(x)$. So by combining the chopper transmission function and the probability function, one gets the effective transmission function, $T(t)$:

$$T(t) \propto \int_{L}^{L+L_d} D(x) C(\frac{x}{v}) dx. \tag{4.2}$$

The measured intensity is correlated to the real intensity by

$$I(t) \propto \int_{-\infty}^{\infty} T(t-\tau) i(t) d\tau. \tag{4.3}$$

If both $i(t)$ and $T(t)$ are approximately Gaussian distributed, then $I(t)$ is also Gaussian and Equation 4.3 may be deconvoluted in a very simple manner: When Δt_i is defined as FWHM of $i(t)$, Δt_I is defined as the full width, half max, FWHM, of $I(t)$ and Δt_T is defined as FWHM of $T(t)$ it follows that

$$\Delta t_I^2 = \Delta t_i^2 + \Delta t_T^2. \tag{4.4}$$

Since $T(t)$ is a function of both $D(x)$ and $C(\frac{v}{x})$ (see Equation 4.2), Equation 4.4 can be written as

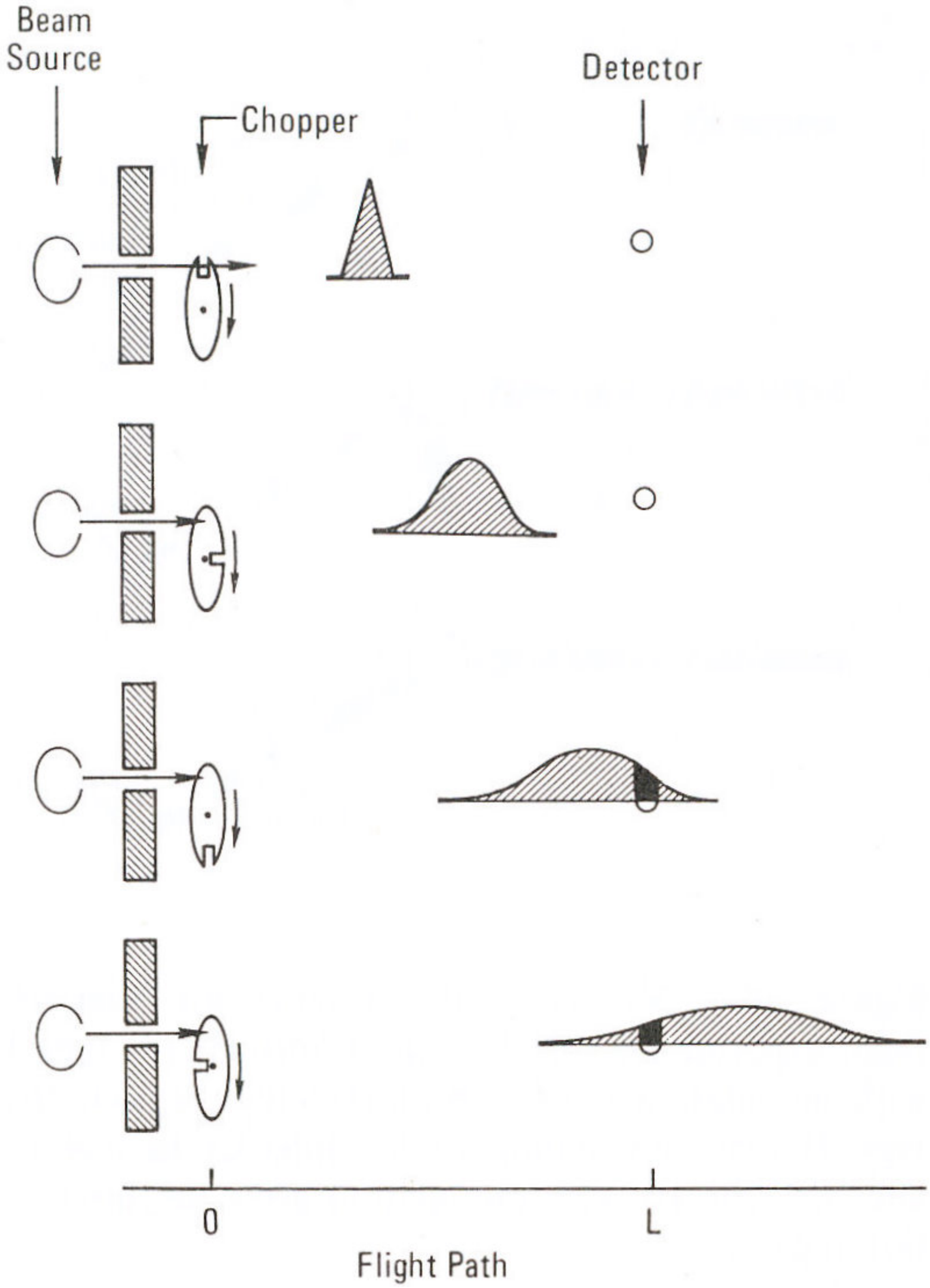

Figure 4.2: A schematic exemplification of a TOF measurement. The atomic beam enters from the left side, and is adjusted by a rotating chopper disk. It then travels towards the detector on the right. The TOF signal at the intersection with the detector is marked black [45].

$$\Delta t_I^2 = \Delta t_i^2 + \Delta t_C^2 + \Delta t_D^2. \tag{4.5}$$

This means that the actual width of the measured TOF-peak, Δt_I^2, consist of the real intensity width, Δt_i^2, and a broadening, both due to the chopper slit, Δt_C^2, and the ionization volume of the detector, t_D^2 [46]. To calculate this width a precise knowledge of the instrumental broadening Δt_C^2 and Δt_D^2 is needed. These broadenings can be estimated as:

$$\Delta t_D = \frac{X_D}{v}, \tag{4.6}$$

$$\Delta t_C = \frac{\omega_{ch}}{2\pi r_{ch} \upsilon_{ch}}. \tag{4.7}$$

X_D is the effective ionization length of the detector, ω_{ch} is the slit width of the chopper, r_{ch} is the radius of the chopper disc that is in the beam line and υ_{ch} is the chopper frequency [35]. The real intensity width is estimated as

$$\Delta t_i = L_{CD} \frac{\Delta v}{v}. \tag{4.8}$$

L_{CD} is the distance from chopper to detector, v is the speed of the beam and Δv is the FWHM of the velocity broadening.

By fitting the detected intensity, $I(t)$, with a Gaussian distribution, $\bar{G}(t)$, the most probable time of flight, t_f is at the maximum of the fitted function. By dividing $\bar{G}(t)$ with the flight distance, L, the velocity distribution, $f(v)$ is written as

$$f(v) = \frac{\bar{G}(t)}{L}, \tag{4.9}$$

and the most probable velocity is given as $v = \max f(v)$.

4.1.1 TOF-resolution

The time width of the peaks plays an important role when trying to resolve TOF spectra. The velocity distribution of the beam will contribute to this time width, but is not necessarily the dominant factor. For the high energy phonon annihilation process, it is normally not the velocity spread that limits the energy resolution, but rather the time widths introduced by the TOF analysis itself [47].

Important resolution quantities:

- FWHM of the measured intensity, $i(t)$: $\Delta t_i = \sqrt{\Delta t_I^2 - \Delta t_T^2}$
- Velocity resolution: $\frac{\Delta v}{v} = \frac{\Delta t_i}{t_f}$
- Energy: $E = \frac{1}{2} m v^2$
- Energy resolution: $\frac{\Delta E}{E} = -2 \cdot \frac{\Delta t_i}{t_f}$

The calculation of the energy resolution is as follows:

$$\begin{aligned}\frac{\Delta E}{E} &= \frac{\frac{1}{2}mv_2^2 - \frac{1}{2}mv_1^2}{\frac{1}{2}mv_f^2} \\ &= \frac{\frac{1}{t_2^2} - \frac{1}{t_1^2}}{\frac{1}{t_f^2}} \\ &= t_f^2 \cdot \frac{t_1^2 - t_2^2}{(t_1 t_2)^2},\end{aligned}$$

t_1 and t_2 are the times corresponding to the time interval given by the FWHM of the time of flight distribution, Δt_i. $t_1 = t_f - \frac{1}{2}\Delta t_i$ and $t_1 = t_f + \frac{1}{2}\Delta t_i$

$$\begin{aligned}\frac{\Delta E}{E} &= t_f^2 \cdot \frac{(t_f - \frac{1}{2}\Delta t_i)^2 - (t_f + \frac{1}{2}\Delta t_i)^2}{((t_f - \frac{1}{2}\Delta t_i)(t_f + \frac{1}{2}\Delta t_i))^2} \\ &= -2\frac{t_f^3 \Delta t_i^2}{(t_f^2 - \frac{1}{4}\Delta t_i^4)^2}.\end{aligned}$$

Since $\Delta t_i << t_f$ we can write $\frac{\Delta E}{E}$ as

$$\frac{\Delta E}{E} = -2\frac{\Delta t_i}{t_f}. \tag{4.10}$$

For improving the resolution of the TOF-measurements it is necessary to [47]

1. Reduce both the angular spread of the beam and the chopper slit widths.
2. Increase the flight path between target and detector.
3. And/or reduce the length of the detector.

4.2 TOF-analysis

The TOF files were fitted with a *MATLAB*-program recently developed for the group by Bjørn Samelin. The procedure is described in Section 4.3.

4.2.1 Transformation from TOF-spectrum to energy spectrum

Flight time spectra can be gained by TOF measurements as explained in Section 4.1. When the flight distances are known (see Figure 4.3), the time-spectrum $f_t(t_{CD})$ can be transformed into an energy-spectrum $f_E(\Delta E)$.

For elastic scattered atoms we can write

$$E_i = \frac{1}{2}m\left(\frac{L_{CT}}{t_{CT}}\right)^2 = \frac{1}{2}m\left(\frac{L_{CD}}{t_{CD}^e}\right)^2 = \frac{1}{2}m\left(\frac{L_{TD}}{t_{TD}^e}\right)^2. \tag{4.11}$$

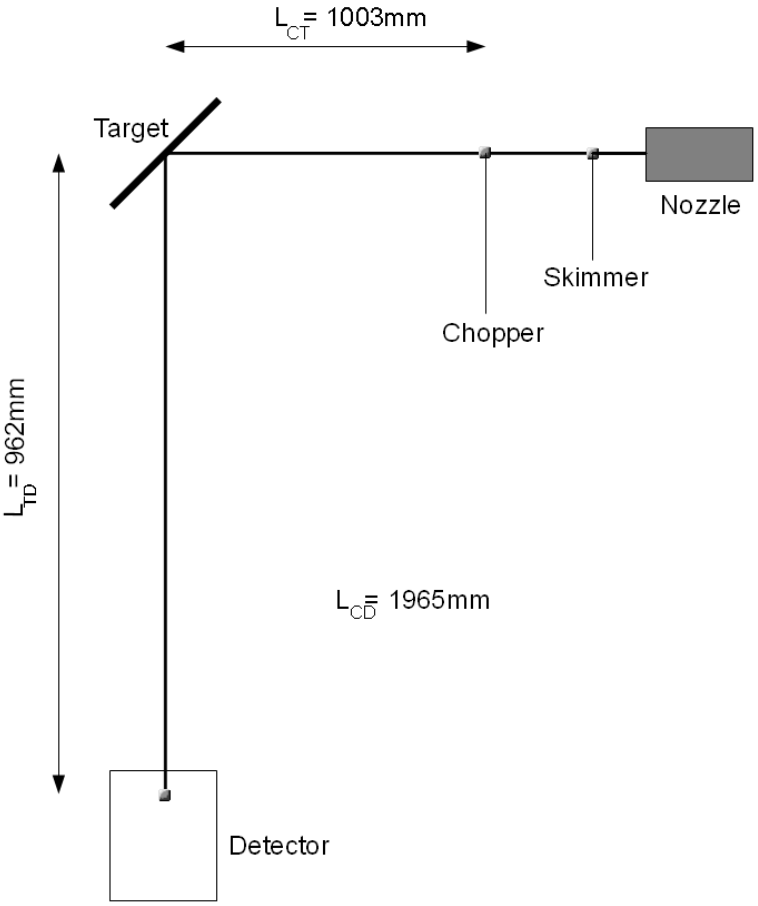

Figure 4.3: A general view of the beam path, including all the lengths needed for the calculations.

L_{CT} is the distance from chopper to target, L_{CD} is the distance from chopper to detector and L_{TD} is the distance from target to detector. The corresponding times are t_{CT}, t^e_{CD} and t^e_{TD} respectively. The superscript e stands for elastic. For the inelastic scattered atoms the energy after impact is

$$E_f = \frac{1}{2} m \left(\frac{L_{TD}}{t^i_{TD}} \right)^2 . \tag{4.12}$$

t^i_{TD} is the time the atom uses from the target to the detector when it is inelastic scattered.

Combining Equation 4.11 and 4.12 one gets the energy spectrum [39]:

$$\Delta E = E_f - E_i = E_i \left[\left(\frac{\frac{L_{TD}}{L_{CD}} \cdot t^e_{CD}}{t^i_{CD} - \frac{L_{CT}}{L_{CD}} \cdot t^e_{CD}} \right)^2 - 1 \right] . \tag{4.13}$$

$\Delta E > 0$ means that the atom gained energy through phonon annihilation, and $\Delta E < 0$ means that the atom lost some energy through phonon generation. The TOF spectrum is a time spectrum, and because of the non-linearity between energy and time in Equation 4.13, it is necessary to multiply with the Jacobian determinant in order to convert from a time spectrum to an energy spectrum.

$$I_E(\Delta E) = I_t(t^i_{CD}) \cdot \mid \frac{dt^i_{CD}}{d\Delta E} \mid . \tag{4.14}$$

Writing t^i_{CD} as a function of ΔE gives

$$t^i_{CD} = \frac{\frac{L_{TD}}{L_{CD}} \cdot t^e_{CD}}{\sqrt{(\Delta E + E_i)}} + \frac{L_{CT}}{L_{CD}} \cdot t^e_{CD}, \tag{4.15}$$

and the corrected intensity is then

$$I_E(\Delta E) = I_t(t_{CD}) \cdot \mid \frac{dt_{CD}}{d\Delta E} \mid = I_t(t_{CD}) \cdot \frac{E_i (t^i_{CD} - \frac{L_{CT}}{L_{CD}} \cdot t^e_{CD})^3}{m \cdot L^2_{TD}} . \tag{4.16}$$

Both the height and the width of the phonon peaks are changed during this transformation, but the total intensity remains the same. Peaks corresponding to shorter flight times ($\Delta E > 0$) are getting broader and lower, and the peaks corresponding to longer flight times ($\Delta E < 0$) are getting more narrow and higher.

Using Equation 2.20 and 4.13, the gain or loss in parallel and the perpendicular momentum of the scattered atom respectively, is calculated to be

$$\Delta K_{\parallel} = K_f - K_i = k_i \left[\frac{\frac{L_{TD}}{L_{CD}} \cdot t^e_{CD}}{t^i_{CD} - \frac{L_{CT}}{L_{CD}} \cdot t^e_{CD}} \cdot \sin(\theta_{SD} - \theta_i) - \sin(\theta_i) \right] . \tag{4.17}$$

$$\Delta k_{\perp} = k_{f,z} - k_{i,z} = k_i \left[\frac{\frac{L_{TD}}{L_{CD}} \cdot t^e_{CD}}{t^i_{CD} - \frac{L_{CT}}{L_{CD}} \cdot t^e_{CD}} \cdot \cos(\theta_{SD} - \theta_i) - \cos(\theta_i) \right] . \tag{4.18}$$

Table 4.1: Values used in this master thesis.

Vertical position of chopper	CP	0.9 inch
Pressure helium beam	p_0	100bar
Frequency, chopper	$\upsilon_{chopper}$	272 Hz
Number of channels	$N_{channel}$	400
Channel width	$t_{channel}$	2.5 μs
Delay time	t_d	1400μs
Distance, chopper-detector	L_{CD}	1965 mm
Distance, chopper-target	L_{CT}	1003 mm
Distance, target-detector	L_{TD}	962 mm
Angle, chopper-detector	θ_{CD}	90.072°

θ_{SD} is the angle between the source and detector and k_i, the magnitude of the wave vector, $\vec{k}_i$, is given as

$$k_i = \frac{2\pi}{\lambda}. \tag{4.19}$$

λ is the wave length of the impinging atom.

In analogy with the energy spectrum, the Jacobian determinant has to be multiplied with the intensity spectrum:

The parallel contribution:

$$I_K(\Delta K_{\parallel}) = I_t(t^i_{CD}) \cdot \mid \frac{dt^i_{CD}}{d\Delta K} \mid = I_t(t^i_{CD}) \cdot \frac{(t^i_{CD} - \frac{L_{CT}}{L_{CD}} \cdot t^e_{CD})^2}{k_i \cdot \frac{L_{TD}}{L_{CD}} \cdot t^e_{CD} \cdot \sin(\theta_{SD} - \theta_i)}. \tag{4.20}$$

With k_i from Equation 4.19:

$$I_K(\Delta K_{\parallel}) = I_t(t^i_{CD}) \cdot \mid \frac{dt^i_{CD}}{d\Delta K} \mid = I_t(t^i_{CD}) \cdot \frac{\hbar(t^i_{CD} - \frac{L_{CT}}{L_{CD}} \cdot t^e_{CD})^2}{m \cdot L_{TD} \cdot \sin(\theta_{SD} - \theta_i)}. \tag{4.21}$$

Values used for fitting and analysis

The values used for fitting and analysis in this master thesis are listed in Table 4.1.

Corrections and transformations

Before the fitting procedure, some corrections and transformations needs to be made:

- Find the correct angle of the incoming beam, see Section 3.4.3.
- Find correct flight time: $t_f = t_d + t_p - t_c - \frac{t_{ch}}{2}$, see Section 3.4.2.
- Find beam energy, see Section 4.2.1:

Table 4.2: The two measurement conditions. T_N is the temperature of the nozzle, and therefore the temperature of the beam, T_s is the sample temperature and β is the Weare value. The third row is the values needed for the Weare criterion to be fulfilled.

T_N [K]	T_{sample} [K]	β
$108,5$	130	$0,04$
110	300	$0,08$
55	77	$0,01$

- Elastic scattering: $E_i = \frac{1}{2}m\left(\frac{L_{CT}}{t_{CT}}\right)^2 = \frac{1}{2}m\left(\frac{L_{CD}}{t^e_{CD}}\right)^2 = \frac{1}{2}m\left(\frac{L_{TD}}{t^e_{TD}}\right)^2$. L_{CT} is the distance from chopper to target, L_{CD} is the distance from chopper to detector and L_{TD} is the distance from target to detector. The corresponding times are t_{CT}, t^e_{CD} and t^e_{TD} respectively.
- Inelastic scattering: $\Delta E = E_f - E_i = E_i\left[\left(\frac{\frac{L_{TD}}{L_{CD}}\cdot t^e_{CD}}{t^i_{CD}-\frac{L_{CT}}{L_{CD}}\cdot t^e_{CD}}\right)^2 - 1\right]$. t^i_{CD} and t^e_{CD} is the time the atom uses from the target to the detector when it is inelastically or elastically scattered, respectively.

Figure 4.20 shows the flight-time-spectrum of TOF2889.dat and Figure 4.24 shows the corresponding energy-spectrum. Because of the multiplication with the Jacobian determinant, the signal is stretched a lot at the lower energies, negative energies with respect to the elastic peak energy. Not only the range of the noise is increasing, also the signal is.

The Weare criterion

For the single phonon process to dominate the multi-phonon process, the Weare criterion, see Equation 2.17, has to be fulfilled; $\beta < 0,01$. For the measurements done for this thesis we have two different measurement conditions; low sample temperature and sample at room temperature, where β is around 0,04 and 0,08 respectively, see Table 4.2. It is clear that the colder the sample is, the less influence there is from the multi-phonon process. For the Weare criterion to be fulfilled, both the nozzle temperature and the sample temperature have to be lower ($T_N < 55$ K and $T_{sample} < 77$ K). This is not possible with the current setup of the apparatus.

4.3 Fitting the time-of-flight measurements

The goal with this fitting procedure is to fit Gaussian functions into the time of flight signal. The large multi-phonon background means that this is a difficult procedure, with the peaks being so broad that the results obtained cannot be said to be 100% certain. However, with the large amount of data available, the trends can be extracted with very good certainty. Further experiments can then in the future be used to do targeted tests to obtain specific energies with higher probabilities. For the fit to work, good start parameters need to be included.

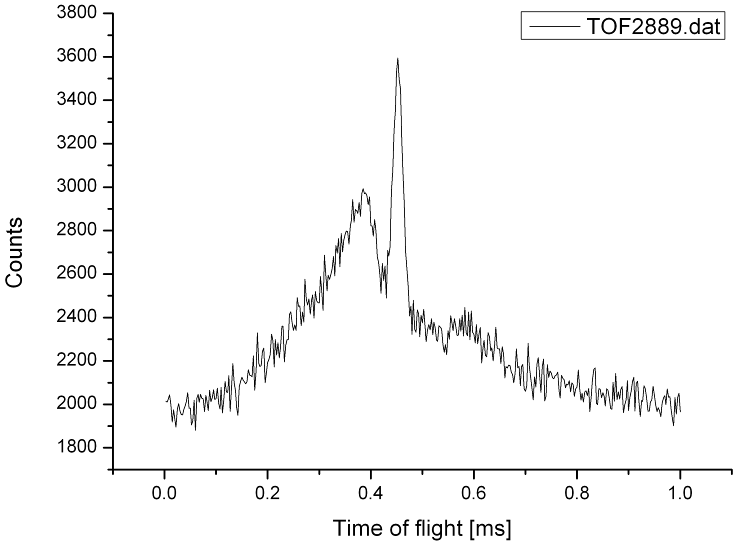

Figure 4.4: Time-of-flight spectrum before the corrections from Equation 3.3 has been included. The TOF2899.dat measurement was done in the $\Gamma\vec{M}-$direction, see Figure 2.3, the angle of the incoming helium beam $\theta_i = 48,280°$, the temperature of the nozzle $T_N = 108$ K, the pressure of the helium beam $p_0 = 100$ bar, the temperature of the sample $T_S \approx 300$ K. Measurement done by Katrin Fladischer.

Table 4.3: Measurement parameters for TOF2889.dat

Direction	$\Gamma\vec{M}$
Incoming angle of helium beam	$\theta_i = 48,3°$
Temperature nozzle	$T_N = 108$ K
Pressure helium beam	$p_0 = 100$ bar
Temperature sample	$T_S \approx 300$ K

TOF2889.dat was used for an illustration of the fitting procedure, and the raw data are shown in Figure 4.4. The TOF2899.dat measurement was done in the $\Gamma\vec{K}-$direction, see Figure 2.3, the angle of the incoming helium beam $\theta_i = 48,280°$ and the temperature of the sample $T_S \approx 300$ K. Parameters are also presented in Table 4.3.

4.3.1 Procedure to identify the peaks in the time of flight spectrum

Before the fitting is done, all resolvable peaks have to be identified. This is done in three steps:

1. Finding the peaks
2. A found peak is subtracted from the raw signal.

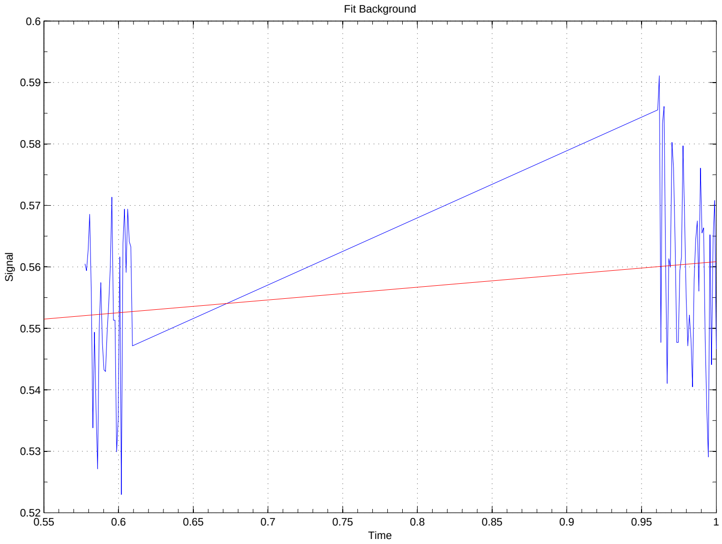

Figure 4.5: The background noise is deleted with a linear fit for a better resolution. As seen in Figure 4.4, the background noise lies around 2000 counts.

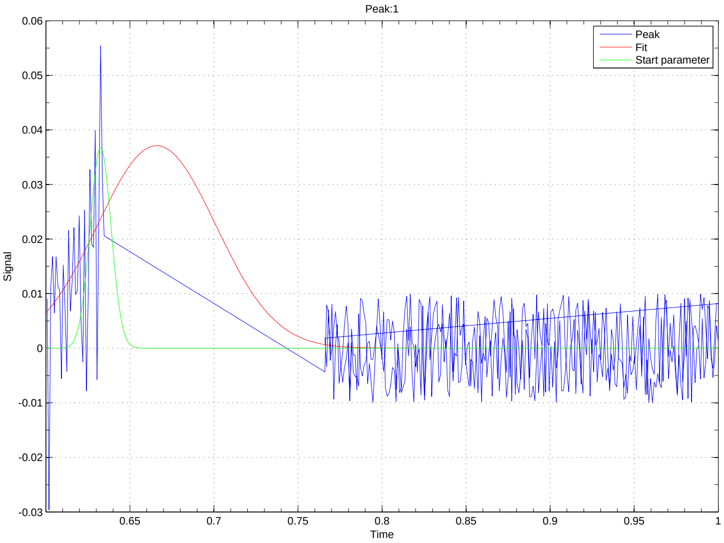

Figure 4.6: The first Gaussian peak fitted. The blue line is the signal, the green line depicts the start parameter for the Gaussian fit and the red line is the fit.

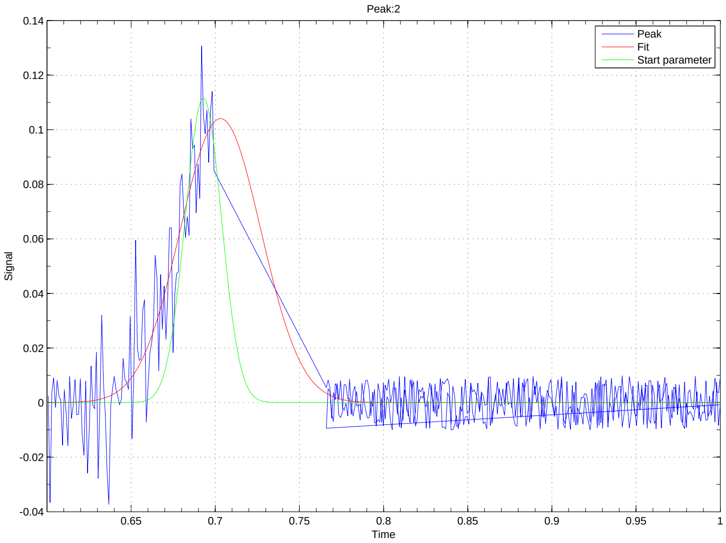

Figure 4.7: The second Gaussian peak fitted. The blue line is the signal, the green line depicts the start parameter for the Gaussian fit and the red line is the fit.

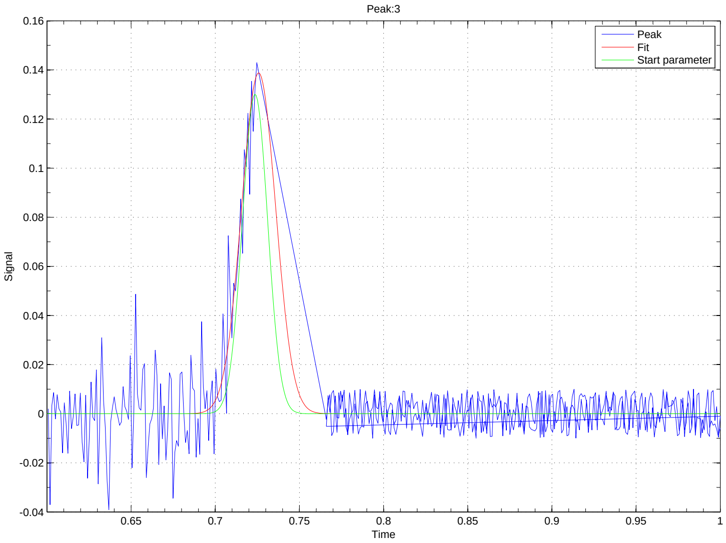

Figure 4.8: The third Gaussian peak fitted. The blue line is the signal, the green line depicts the start parameter for the Gaussian fit and the red line is the fit.

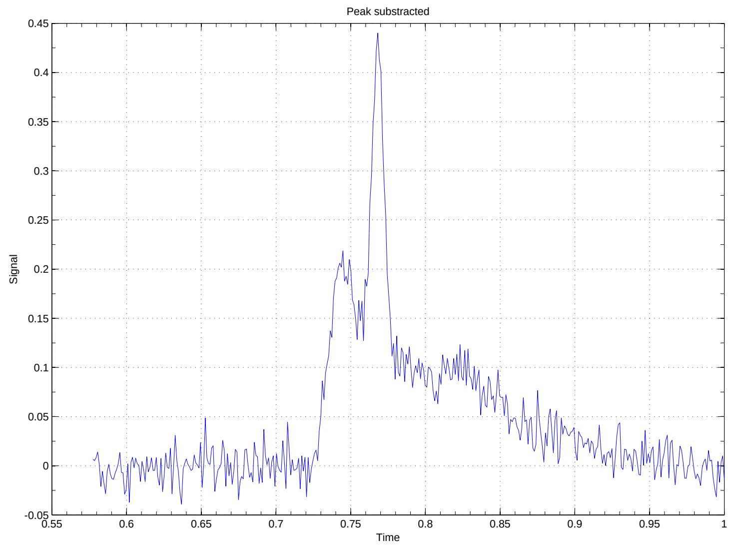

Figure 4.9: The three first Gaussian peaks subtracted from the signal. The background on the left side is now only noise.

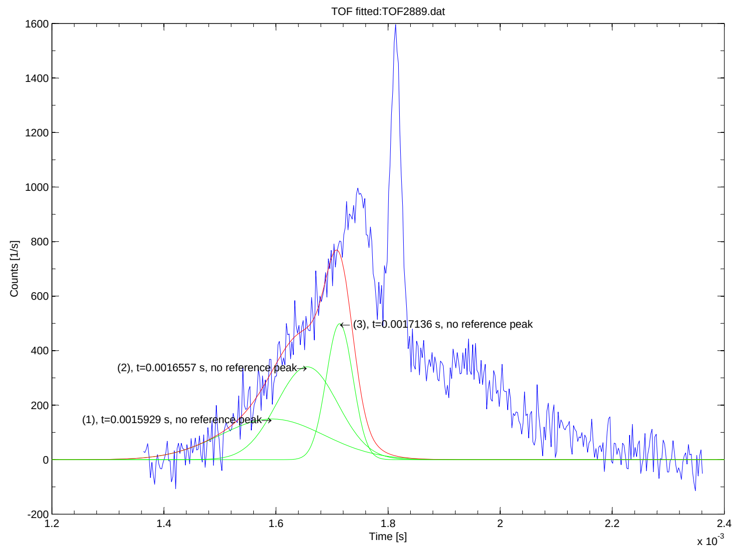

Figure 4.10: The three first Gaussian peaks fitted. The 'no reference peak' means that the elastic peak is still not fitted, and therefore there is no ΔE yet. The green lines are the fits of the peaks, the red line is the sum of the single fits and the blue line is the signal.

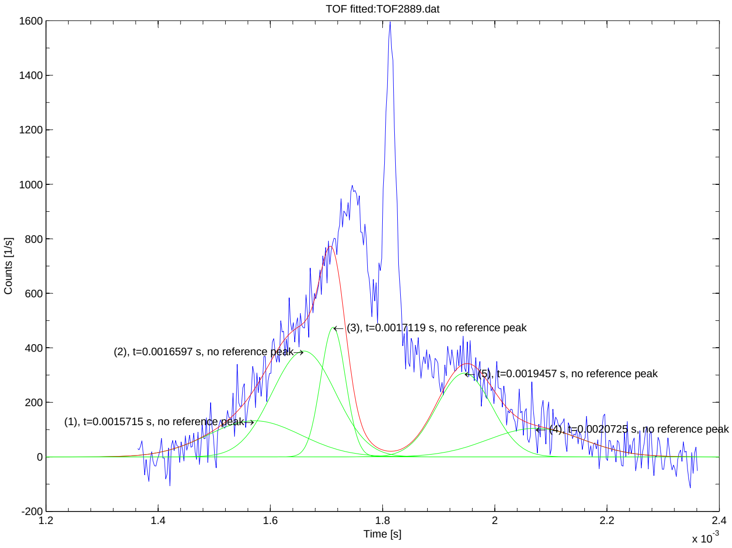

Figure 4.11: The five first Gaussian peaks fitted. The green lines are the fits of the peaks, the red line is the sum of the single fits and the blue line is the signal.

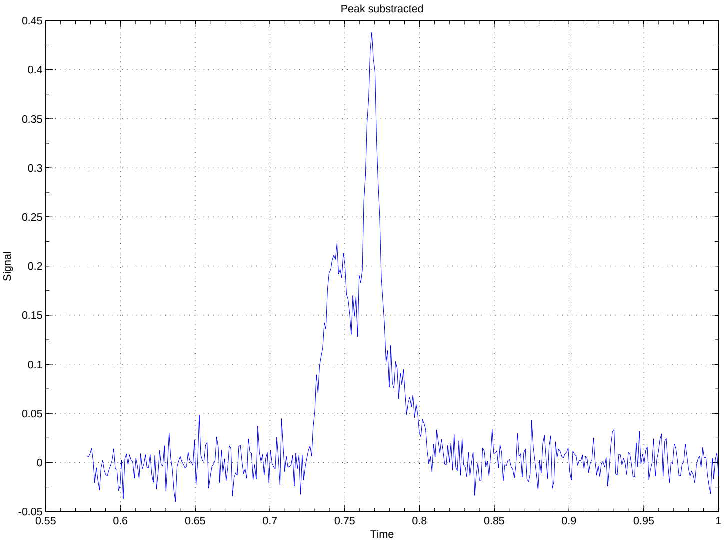

Figure 4.12: The five first Gaussian peaks subtracted from the raw signal.

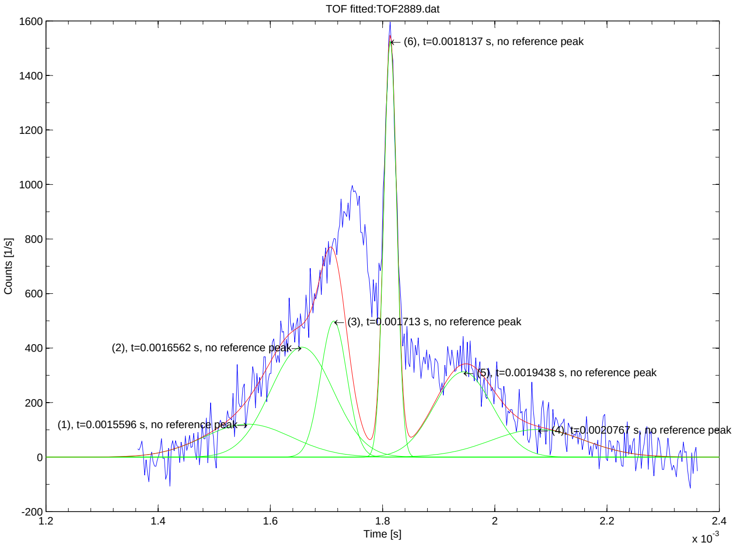

Figure 4.13: The six first Gaussian peaks fitted, including the elastic peak. The green lines are the fits of the peaks, the red line is the sum of the single fits and the blue line is the signal.

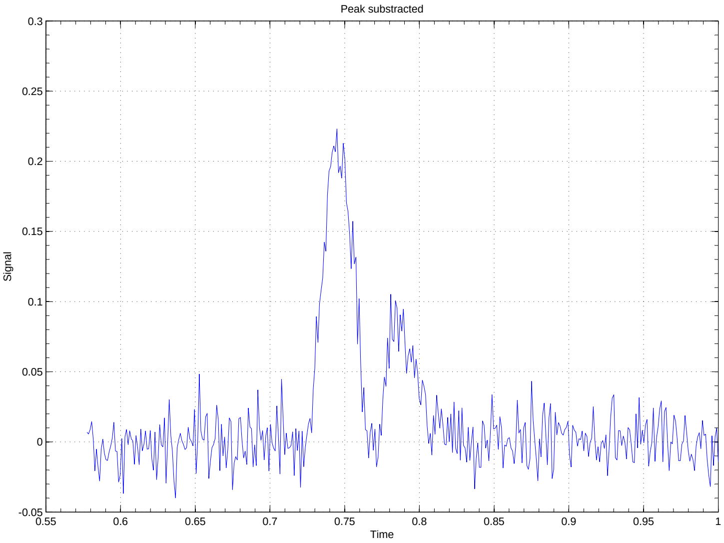

Figure 4.14: The six first Gaussian peaks subtracted from the raw signal. The two peaks left are not Gaussian distributed.

3. Are all peaks found, the fitting process is done again for all peaks, but:
    - The actual peak to be fitted is not subtracted from the raw signal
    - All peaks which are still to be fitted in this iteration step are subtracted from the raw signal using the fit parameters from the last run.
    - Peaks which have already been fitted in this iteration step are subtracted from the raw signal using the fit parameters found in the actual run.

4.3.2 The fitting procedure

The fitting procedure is as follows:

1. First the background noise (caused by the background pressure in the detector chamber) is subtracted from the raw data with a linear fit, see Figure 4.5.
2. A phonon either gains or loses energy. Because it is not probable that a helium atom both gain or lose energy in the same process, a phonon peak does not cross the elastic peak. Due to that, the signal after the elastic peak is set to a random signal (around 0), see Figure 4.6. This is done in order to force the peaks on the left side of the elastic peak to not cross the middle.
3. The only way to separate the Gaussian peaks is to find the first 3 peaks from the left to the right. Fit a Gaussian function for the left most peak, see Figure 4.6.
4. Subtract the fitted peaks from the raw signal. In Figure 4.9 the three first peaks are subtracted from the signal.
5. Repeat Point 3 for peak 2 and 3, see Figure 4.7 and Figure 4.8. It is important to find a good inflection point before the peak top, so that the fitting program does not make a too big Gaussian fit. This is important for separation between the different peaks. In Figure 4.10 the 3 first peaks are fitted.
6. After the 3 first peaks, the same procedure is performed from the right side with usually 2 or 3 Gaussian fits. In this example, Figure 4.11, there is only 2 Gaussian peaks on the right side.
7. Then it ends up with a middle peak with two shoulders, see Figure 4.12.
8. Pick parameters for fitting the middle peak. Figure 4.13 shows the elastic peak fitted together with the first 5 peaks.
9. After the subtraction of the middle peak, the remaining signal looks like two small peaks, not really Gaussian distributed, see Figure 4.14. This is because there is an additional broad peak centered around the middle caused by contamination on the surface and/or a multi-phonon background. The multi-phonon background should in principle be symmetrical around 0. The Weare criterion in Equation 2.17 states that for the single phonon process to dominate the multi-phonon process, β has to be less then $0,01$. In the measurements

done for this thesis, β is in the range from $0,03$ to $0,08$. This means that there will be a contribution from the multi-phonon scattering.

10. A trick is needed for the fitting of the multi-phonon peak: Try to make a Gaussian peak as symmetrical as possible around the middle of the two peaks from Point 9, see Figure 4.15. This is not fitted in the first iteration step. Decide where a Gaussian peak would lie from the conditions of the small peaks (height and width) and subtract this peak. When this is plotted, the fit is shifted due to the multi-phonon peak, see Figure 4.16. This is corrected for in the next iteration, Point 13. Then two Gaussian peaks still appear (either number 9 and 10 or number 8 and 9, as it is in this case, see Figure 4.17.). There may also be more peaks, but it is not possible to resolve them. The background signal then sometimes goes below 0, as seen in Figure 4.17, because of the fact that the included multi-phonon peak is only a rough estimate. At the same time the peaks 1 to 6 might in sum lie above the raw signal. It will be corrected in the second evaluation round, see Point 13. Figure 4.18 shows all the peaks fitted to the raw signal.

11. To check how good the fitting is, the fitted peaks are subtracted from the raw signal. This is shown in Figure 4.19. As seen, there is nothing left which could be identified as a peak, which means that all the resolvable peaks are found.

12. If not enough peaks are included, it will not only be background noise in the fit from Point 11. Figure 4.23 shows all the peaks subtracted when the 9th peak is missing, and together with the plot of all the peaks fitted in Figure 4.22 (with the 9th peak missing) this is a good indicator for more peaks.

13. Run the program one more time, subtract the peaks found, and even after the second time, the signal is better distributed.

14. Point 13 is done 3 times. Figure 4.20 and Figure 4.21 show the fitting and background noise after 3 iterations.

15. The dirt/multi-phonon peak is found after the second iteration.

Two files are produced: .EDP-files and .POS-files. The .EDP-files contains the energy results (peak values) and the energy plot as seen in Figure 4.24, and the .POS files holds information about the TOF-results before they are converted into the energy-scale, see Section 4.2.1. All peak energies given in the .EDP-files are in respect to the elastic peak. For dispersion analysis of these files, the energies have to be converted into reciprocal positions.

- Transform the flight-time-spectrum into an energy-spectrum. Because of the non-linearity of the energy the overall intensity of the spectrum has to be multiplied with the Jacobian determinant, see Section 4.2.1.

- Find beam wavelength $\lambda = \frac{h}{\sqrt{2 m_{He} \Delta E}}$

- Find length of beam wave vector $\mid k_i \mid = \frac{2\pi}{\lambda}$.

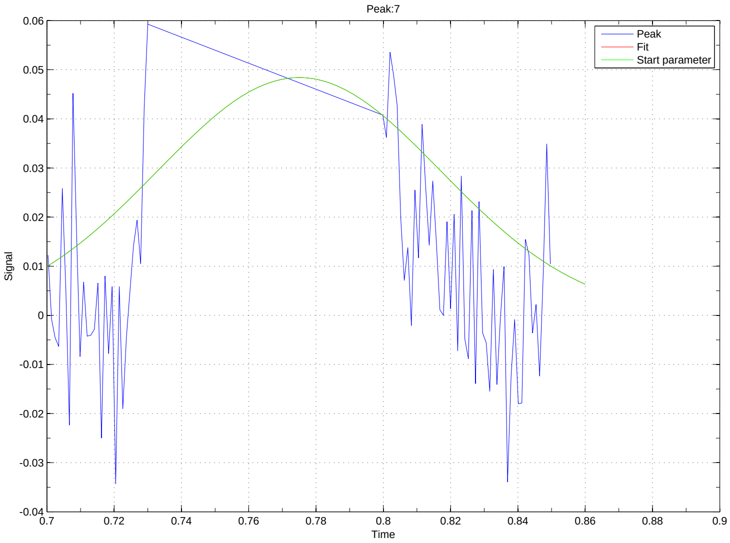

Figure 4.15: The Gaussian fit made as symmetrical as possible around the middle of the two peaks. The blue line is the signal and the green line depicts the start parameter for the Gaussian fit. There is no fit made for this step.

- Find position in K-space:
  - Parallel: $\Delta K_{\parallel} = k_i \left[\frac{\frac{L_{TD}}{L_{CD}} \cdot t^e_{CD}}{t^i_{CD} - \frac{L_{CT}}{L_{CD}} \cdot t^e_{CD}} \cdot \sin(\theta_{SD} - \theta_i) - \sin(\theta_i) \right].$
  - Perpendicular: $\Delta k_{\perp} = k_i \left[\frac{\frac{L_{TD}}{L_{CD}} \cdot t^e_{CD}}{t^i_{CD} - \frac{L_{CT}}{L_{CD}} \cdot t^e_{CD}} \cdot \cos(\theta_{SD} - \theta_i) - \cos(\theta_i) \right].$

  θ_{SD} is the angle between the source and the detector. θ_i is the angle of the incoming beam.

- Transform the flight-time-spectrum to a reciprocal-space-spectrum. Because of the non-linearity of the ΔK the overall intensity of the spectrum has to be multiplied with the Jacobian determinant.

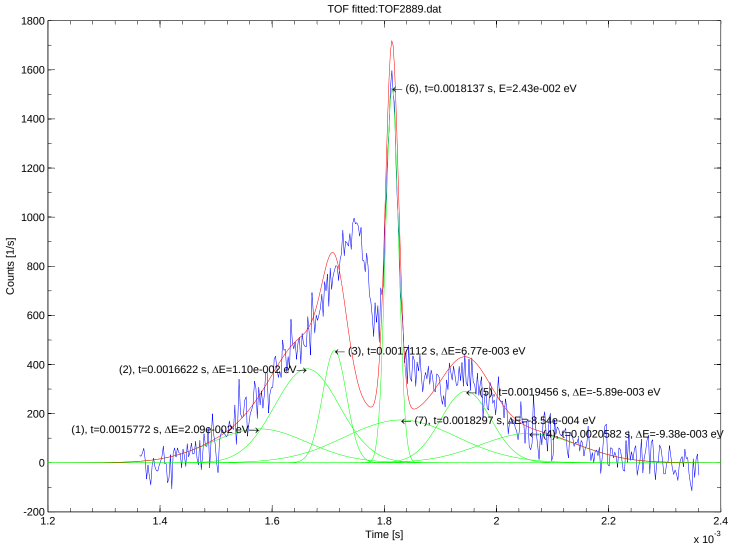

Figure 4.16: The seven first peaks plotted. The multi-phonon peak shifts the peak 1 to 6. The green lines are the fits of the peaks, the red line is the sum of the single fits and the blue line is the signal.

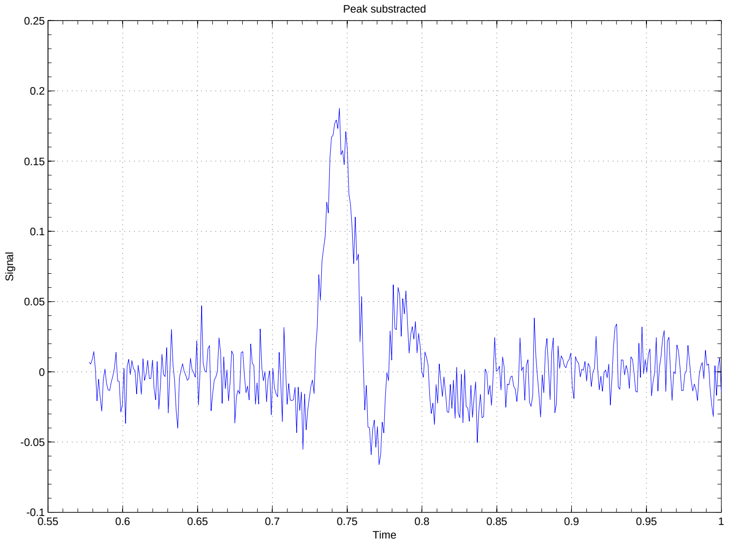

Figure 4.17: The last 2 peaks left from the raw signal. As seen, the background here goes below zero. This is due to the fact that the multi-phonon scattering found is taking up too much place and some of the peaks 1 to 6 are too big for this first iteration, but this will be better with more iterative runs.

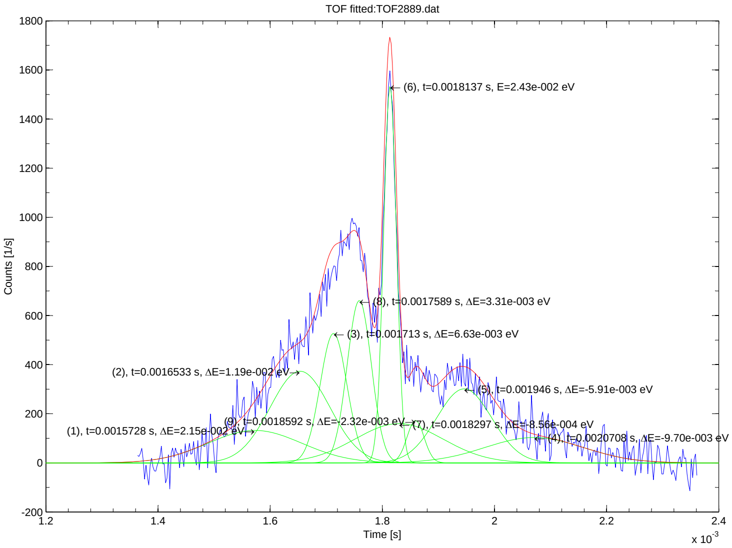

Figure 4.18: The 9 peaks fitted to the raw signal. This fit is not so good, but it is getting better with more iterations, see Figure 4.20. The green lines are the fits of the peaks, the red line is the sum of the single fits and the blue line is the signal.

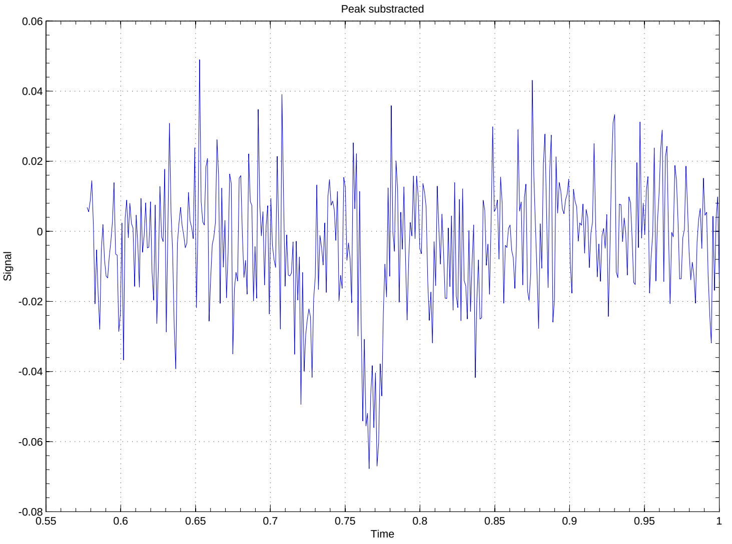

Figure 4.19: The 9 peaks subtracted from the raw signal. It is not possible to resolve any more Gaussian peaks. As seen the background here also goes below zero, but this will be better with more runs. See Figure 4.21.

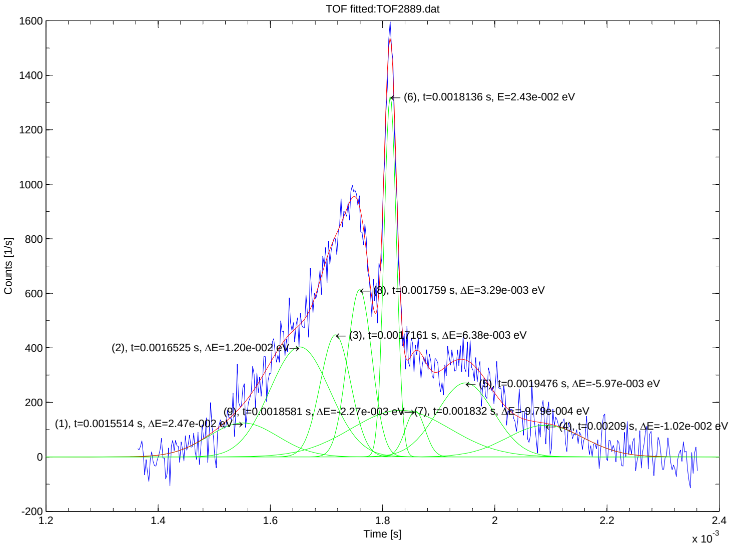

Figure 4.20: The 9 Gaussian peaks fitted to the raw signal after 3 iterative runs.

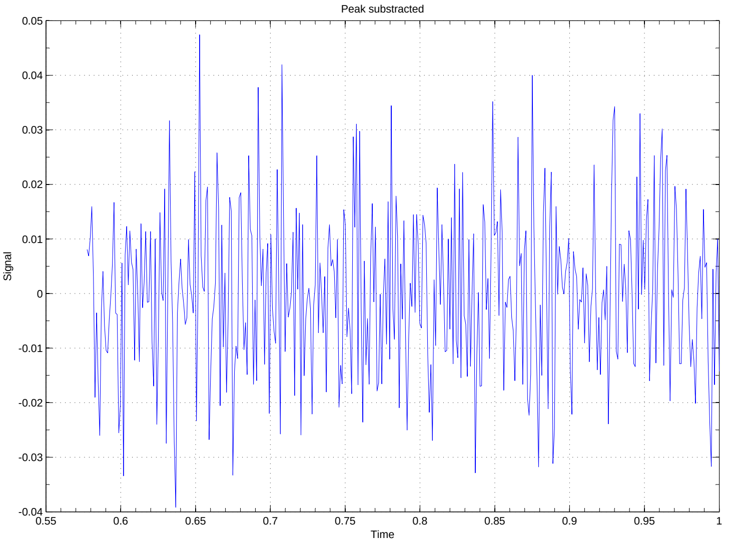

Figure 4.21: The 9 Gaussian peaks subtracted from the raw signal after 3 iterative runs, leaving only noise.

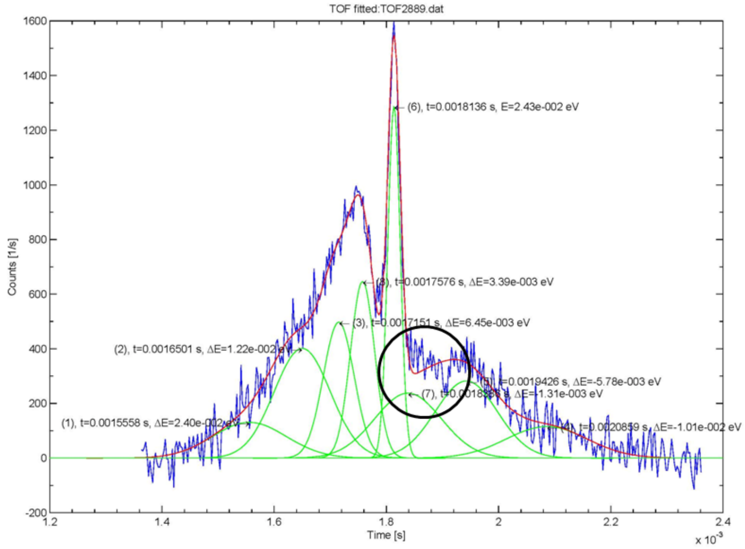

Figure 4.22: The 8 first Gaussian peaks fitted to the raw signal. As seen, the red line for the fitting is not longer a very good fit for the blue signal inside the black circle. This is the same area where the 9th peak is in Figure 4.20. The green lines are the fits of the single peaks.

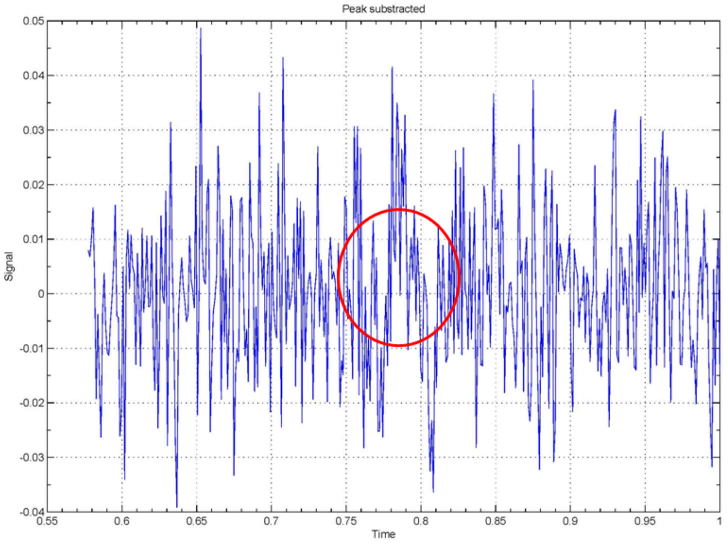

Figure 4.23: The 8 peaks subtracted from the raw signal. Compared to Figure 4.21, it is not only noise. The red ring indicates where the last resolvable Gaussian peak is.

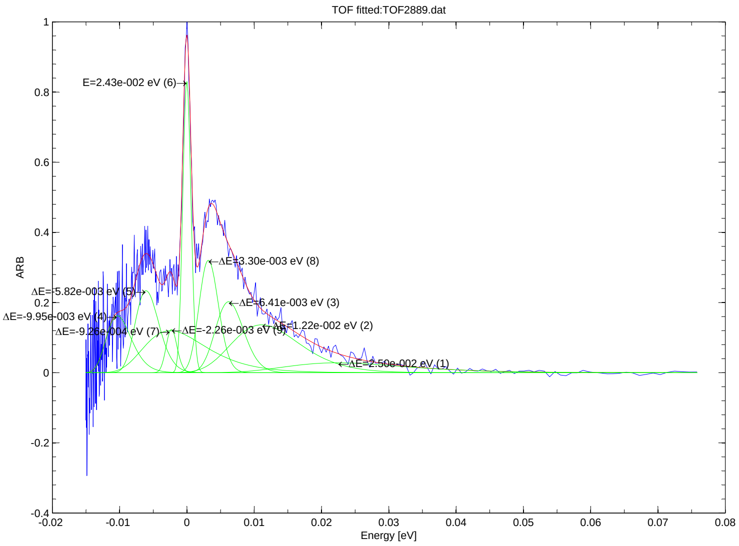

Figure 4.24: A conversion to the energy scale is made. Because of the non-linearity of the conversion from TOF to energy, the overall intensity of the spectrum has to be multiplied with the Jacobian determinant, see Section 4.2.1. The green lines are the fits of the peaks, the red line is the sum of the single fits and the blue line is the signal.

Chapter 5

Results

In this chapter first the diffraction patterns for different sample orientations are presented. They show a (1×1) hexagonal main pattern with an additional weak (2×2) pattern. This is in agreement with previously published results and show that we are indeed measuring on the same surface as previously. Then the results of the phonon measurements are given and compared with theory. The main result is that a low-energy dispersion less phonon band could now be identified. For the $\Gamma\vec{K}$-direction the dispersionless phonon-mode was found at (2,3 +/- 0,6) meV, the first overtone at (6,1 +/- 0,5) meV and the second overtone at (10,9 +/- 1,5) meV. For the $\Gamma\vec{M}$-direction the dispersionless phonon-mode was found at (2,9 +/- 0,4) meV, the first overtone at (6,6 +/- 0,6) meV and the second overtone at (10,8 +/- 1,5) meV.

For the $\Gamma\vec{K}$-direction the dispersionless phonon-mode was found at (2,3 +/- 0,6) meV, the first overtone at (6,1 +/- 0,5) meV and the second overtone at (10,9 +/- 1,5) meV. For the $\Gamma\vec{M}$-direction the dispersionless phonon-mode was found at (2,9 +/- 0,4) meV, the first overtone at (6,6 +/- 0,6) meV and the second overtone at (10,8 +/- 1,5) meV.

5.1 Diffraction spectra for different sample orientations

For the elastic scattering experiments, the scattering angle (the angle between the source and detector) was held constant at $\theta_{SD} = 90°$. The sample was rotated in the scattering plane between 10° and 80°, and in the crystal plane (the azimuthal angle) in steps of 30°. The diffraction pattern is hexagonal, and the periodicity of the main peaks corresponds to the bulk crystal lattice constants at around 4,9 Å. These crystal lattice constant, are the same as found experimentally in [12]. The diffraction pattern show a 60° symmetry, even though with the basis of the unit cell one would expect a 120° symmetry. This may be explained with the presence of terraces, with step height of 1/3 of the unit cell, rotated 60° relative to each other [12]. The additional weak (2×2) peaks (denoted with an * in Figure 5.1, can be explained by a semi-dense surface structure with a (2×1) symmetry [30], since three domains of (2×1) can give a diffraction pattern similar to a hexagonal (1×1)

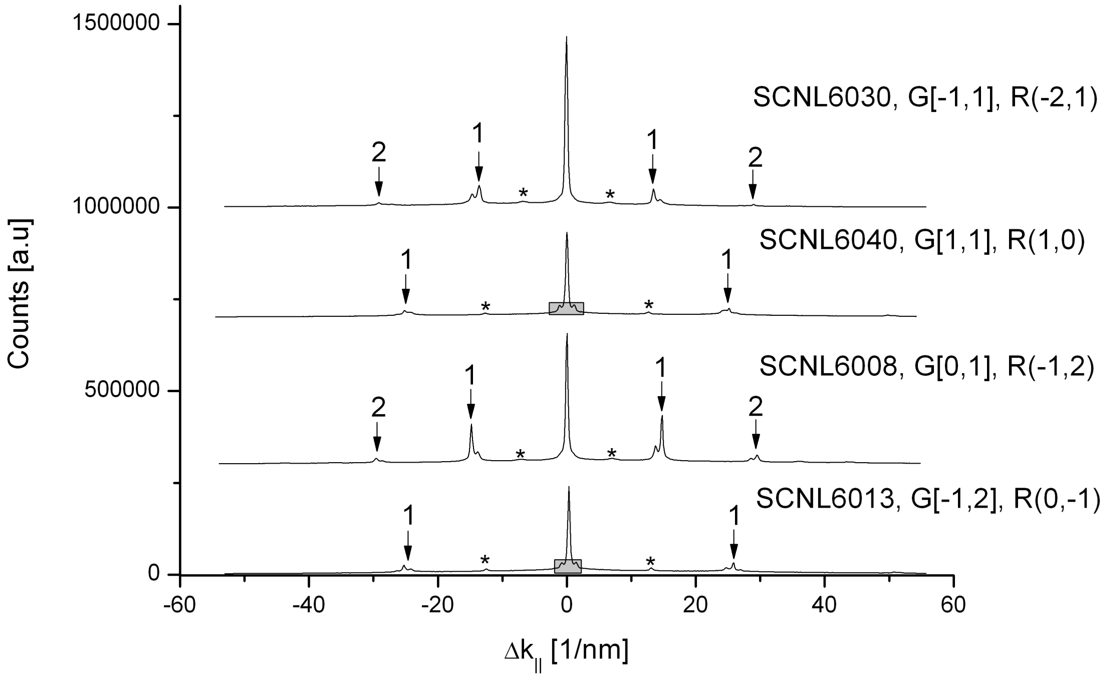

Figure 5.1: In-plane helium atom diffraction spectra for 4 different crystal orientations. The diffraction patterns are shifted by adding 3,5*1E5 to the actual count rates for SCNL6008, adding 7,0*1E5 to the actual count rates for SCNL6040 and adding 1,0*1E6 to the actual count rates for SCNL6030. G[a,b] is the direction in reciprocal space, R(c,d) is the corresponding direction in real space. The incoming wave length of the helium beam was at 0,92 Å for all measurements. 1 is the first order diffraction peak and 2 is the second order diffraction peak. Additional weak peaks are labeled with *, and these weak peaks correspond to the ((2 × 2) reconstruction described in Section 2.2.1. The satellite peaks are indicated in the grey box. The surface temperature $T_S < 130$ K for all measurements.

structure combined with a (2 × 2) structure. The most recent paper by Chen et al. [31] is stating that the experimentally observed (2 × 2) pattern from [12], can be explained by combinations of (2 × 1) surfaces more energetically stable than the dense (1 × 1) surfaces. The satellite peaks around the main diffraction peak in the R(1,0) and R(0,-1) (real space directions), indicated in the grey box in Figure 5.1, is probably due to a long-range surface reconstruction.

5.2 Phonons

Figure 5.5 and Figure 5.6 show the phonon dispersion curves including scan lines. The dispersionless phonon-mode, the first overtone and the second overtone are also all resolved. The first overtone energy should be 2 times the dispersionless phonon-mode energy, and the second overtone energy should be two times the first overtone energy and this fits with our measurements within the experimental error.

Figure 5.2 and Figure 5.3 illustrate the angular area for the direction of the incoming beam in the previous measurements in [23] and for the measurements done for this thesis. Figure 5.4 shows a time of flight spectrum with nine resolvable Gaussian peaks. In addition to the elastic peak at around $t_p = 1.85$ s, phonon peaks are seen. The peaks on the right hand side of the elastic peak correspond to phonon creation, and the peaks to the left of the elastic peak correspond to phonon annihilation. The prominent elastic TOF-peak indicates the presence of a large amount of defects on the surface. The multi-phonon peak is large, as expected given the experimental conditions (see discussion in Section 4.2.1). The prominent elastic peak and the large multi-phonon peak hamper the extraction of more phonon peaks, see Section 4.3. The analysis revealed that because of the large multi phonon background it was not possible to extract phonons corresponding to a Rayleigh mode, but it was possible to fit very nicely a dispersionless optical mode corresponding roughly to the low-energy value predicted by theory, see Figure 5.7 where $\Delta E_{DL} = 2,3$ +/- 0,6 meV. DS stands for dispersionless. In addition higher order harmonics could be fitted for this mode at 6,1 +/- 0,5 meV and 10,9 +/- 1,5 meV. The same mode could be found in the $\Gamma\vec{M}$ direction, see Figure 5.8 where $\Delta E_{DL} = 2,9$ +/- 0,4 meV, and the higher order harmonics at 6,6 +/- 0,6 meV and 10,8 +/- 1,5 meV. The reason why the lower energy phonon-mode could not be resolved in the first published measurements, was most likely due to the fact that these measurements were carried out at a lower pressure of around 80 bar, and hence a worse velocity spread, than the measurements carried out here where the initial pressure was at 100 bar. It is also possible that the crystal used in previous experiments was of a lower quality and/or with more surface contaminates which would lead to a higher multi phonon background and hence make the extraction of the lower energy phonon peaks more difficult.

Table 5.1 and Table 5.2 show the mean energy and the standard deviation for the different phonon-modes. Even though there are two different sample temperatures ($T_S < 130$K and $T_S \approx 300$K) for the ΓM-direction, the standard deviation is in the same range as the standard deviation in the ΓM-direction, where the measurements are done with the same temperature ($T_S < 130$K).

Figure 5.7 and Figure 5.8 show the phonon dispersion curves plotted within a single Brillouin zone, assuming a simple 1x1 structure. The dispersionless mode, the first overtone and the second overtone are all resolved. The dispersionless mode seems to cross the entire Brillouin zone, which is not quite in agreement with the theoretical prediction, but we have successfully measured a lower energy mode. The values of the energy modes measured ((2,3 +/- 0,6) meV, (6,1 +/- 0,5) meV and (10,9 +/- 1,5) meV for the $\Gamma\vec{K}$-direction, and for the $\Gamma\vec{M}$-direction (2,9 +/- 0,4) meV, (6,6 +/- 0,6) meV and at (10,8 +/- 1,5) meV) is not quite the same as the values predicted by theory (5 meV and 7,5 meV for the ΓK-direction and 6 meV and 7.5 meV for the ΓM-direction). A perfect agreement with theory is not to be expected since the theory does not take into account the two different reconstructions present on the surface, but assumes that only the dense (1×1) surface reconstruction is present. Also, the long range surface reconstruction indicated by the satellite peaks

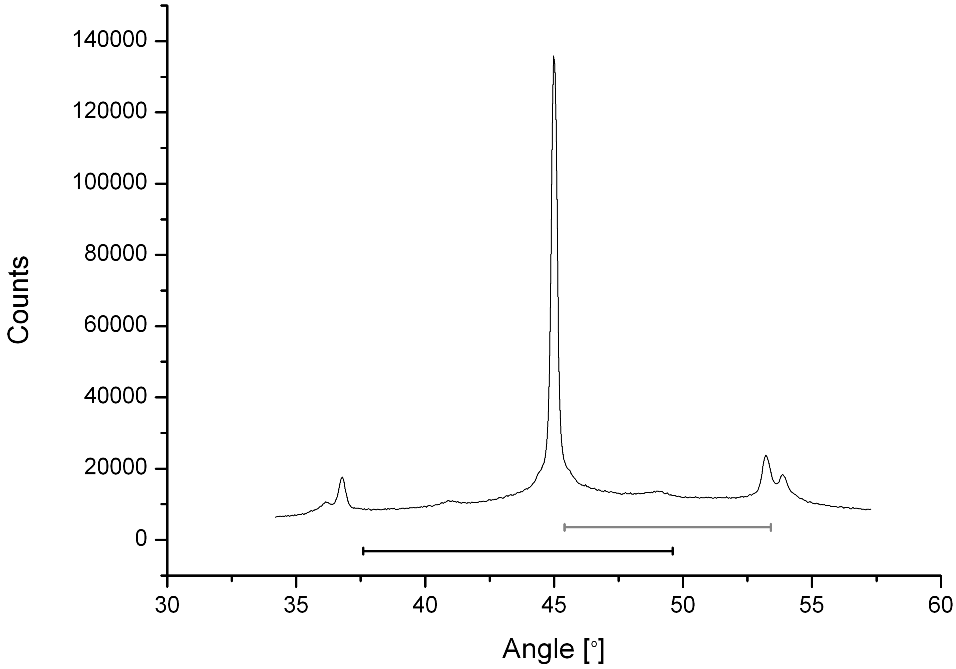

Figure 5.2: Illustration of the angular area for the direction of the incoming beam in [23] and the measurements done for thesis in the $\Gamma\vec{K}$-direction. The black line is the range in the previous measurements given in [23]. The grey line indicates the different angles used for the measurements presented in this thesis.

is also not taken into account.

The large standard deviation is due to the fitting procedure, and this is why no error bars are written for each individual points in Figure 5.5, Figure 5.6, Figure 5.7 and Figure 5.8. Ideally, for each incident angle, several TOF-spectra would be measured and evaluated separately to determine the error in the fitting process. However, due to the time each TOF-measurement takes, this was not done for these initial experiments.

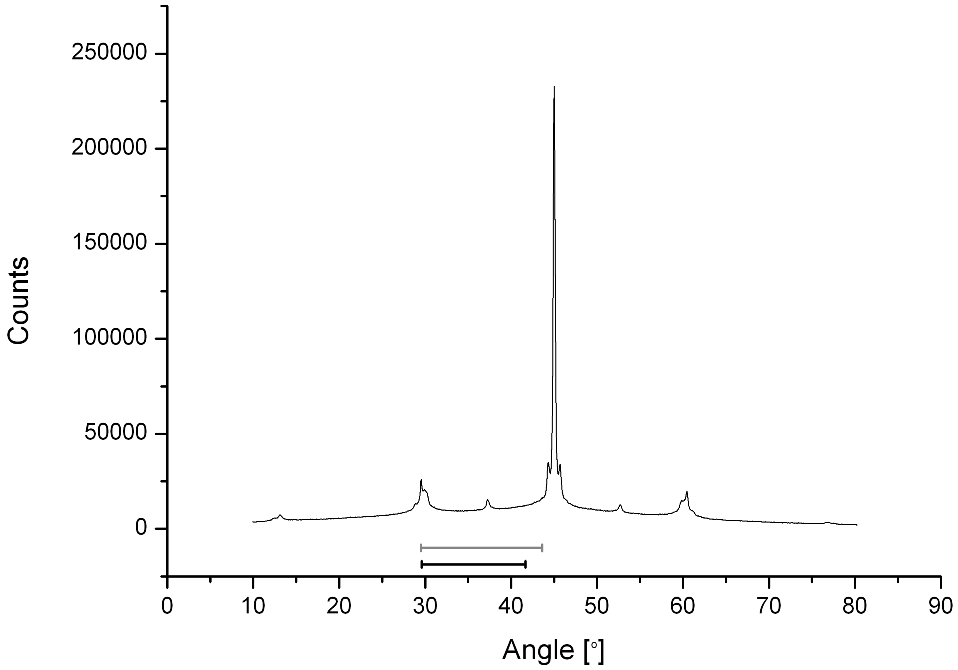

Figure 5.3: Illustration of the angular area for the direction of the incoming beam in [23] and the measurements done for thesis in the $\Gamma\vec{M}$-direction. The black line is the range done in the previous measurements given in [23]. The grey line indicates the different angles used for the measurements presented in this thesis.

Table 5.1: Mean energy and standard deviation for the low-energy phonons in a single Brillouin zone. DL=Dispersionless phonon-mode, FO=First Overtone, SO=Second overtone

$\Gamma\vec{K}$-direction	DL	FO	SO
Mean Energy [meV]	2,3	6,1	10,9
Standard Deviation [meV]	0,6	0,5	1.5

$\Gamma\vec{M}$-direction	DL	FO	SO
Mean Energy [meV]	2,9	6,6	10,8
Standard Deviation [meV]	0,4	0,6	1,5

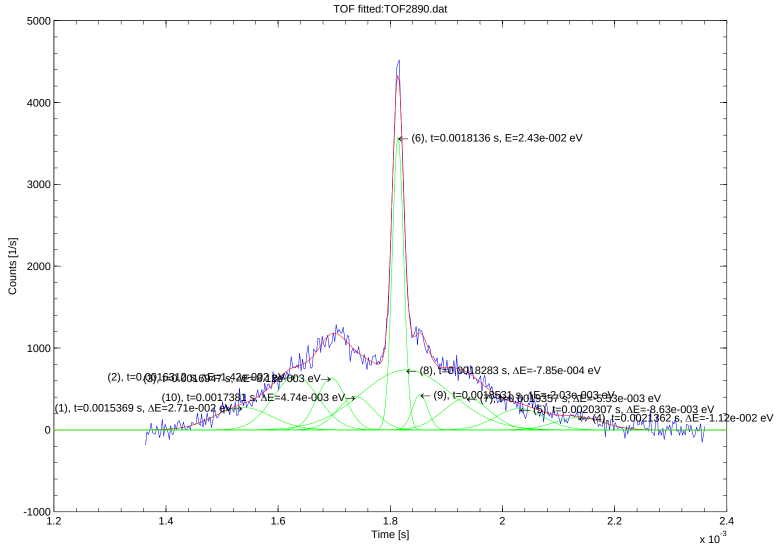

Figure 5.4: Time of flight spectrum with nine resolvable Gaussian peaks. Angle, incoming helium beam: $\theta_i = 52,5°$, Temperature nozzle: $T_N = 108$ K. Temperature sample: $T_S > 150$ K. Pressure, helium: $p_0 = 100$ bar. Number of channels: $N_{channel} = 400$. Channel width: $t_{channel} = 2.5\ \mu s$. Delay time: $t_d = 1400\ \mu s$.

Table 5.2: Mean energy and standard deviation for the low-energy phonons. DL=Dispersionless phonon-mode, FO=First Overtone, SO=Second overtone, - stands for creation of phonons, and + stands for annihilation of phonons.

$\Gamma\vec{K}$-direction	DL-	DL+	FI-	FI+	SO-	SO+
Mean Energy [meV]	-2,1	2,5	-6,6	6,1	-10,7	11,5
Standard Deviation [meV]	0,5	0,6	1,1	0,5	0,8	1,7

$\Gamma\vec{M}$-direction	DL-	DL+	FI-	FI+	SO-	SO+
Mean Energy [meV]	-2,8	3,1	-6,3	7,0	-9,9	11,7
Standard Deviation [meV]	0,4	0,4	0,7	0,4	0,6	1,5

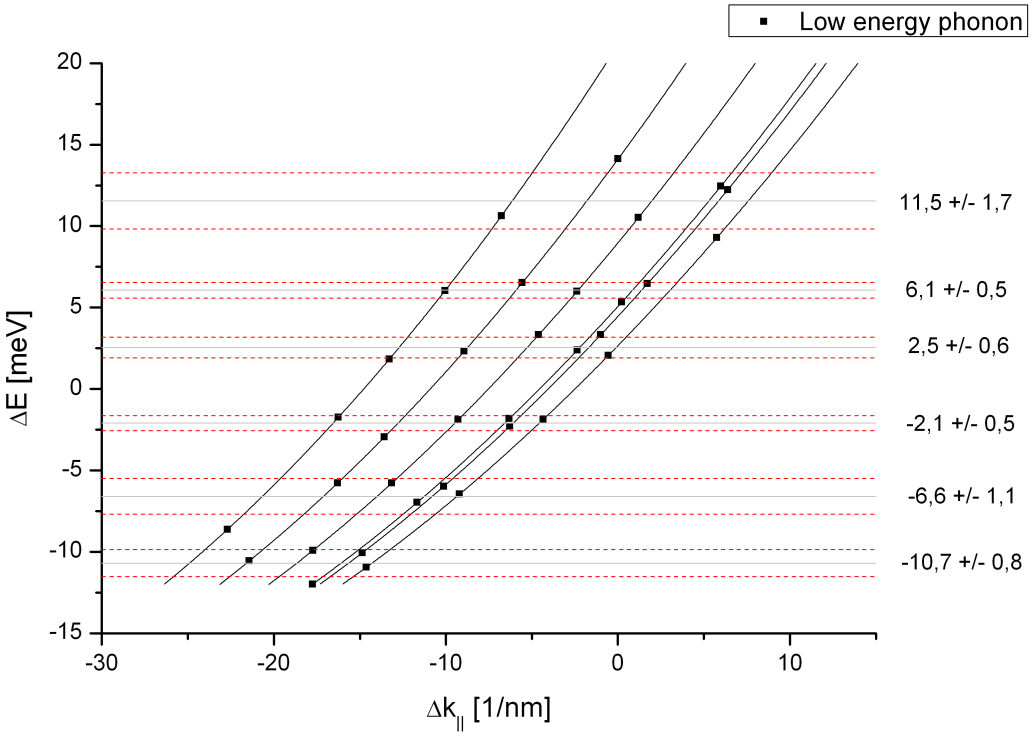

Figure 5.5: Measured phonon dispersion curves in the $\Gamma\vec{K}$-direction for $\Delta\vec{k}_{||}$ vs ΔE plotted in the extended zone scheme. The black line show the scan curves. The squares are the resolved low-energy phonons. The grey line is the mean energy for a particular phonon branch, and the dashed, red line is the corresponding standard deviation. $\Delta E > 0$ corresponds to phonon annihilation, and $\Delta E < 0$ corresponds to phonon creation.

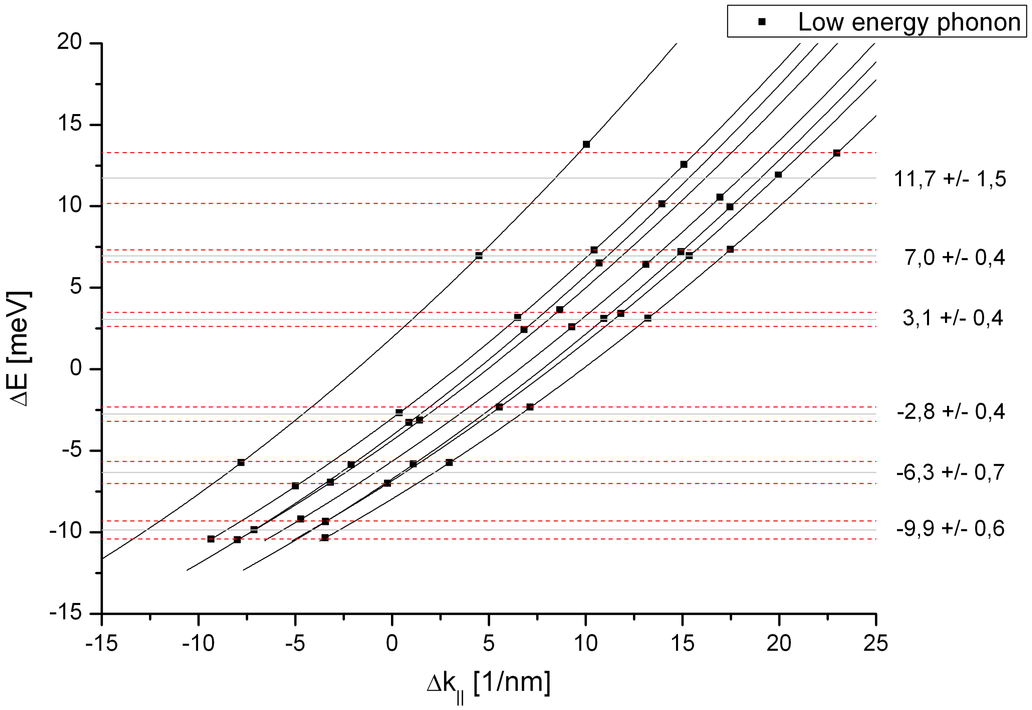

Figure 5.6: Measured phonon dispersion curves in the $\Gamma\vec{M}$-direction for $\Delta\vec{k}_{||}$ vs ΔE plotted in the extended zone scheme. The black line show the scan curves. The squares are the resolved low-energy phonons. The grey line is the mean energy for a particular phonon branch, and the dashed, red line is the corresponding standard deviation. $\Delta E > 0$ corresponds to phonon annihilation, and $\Delta E < 0$ corresponds to phonon creation.

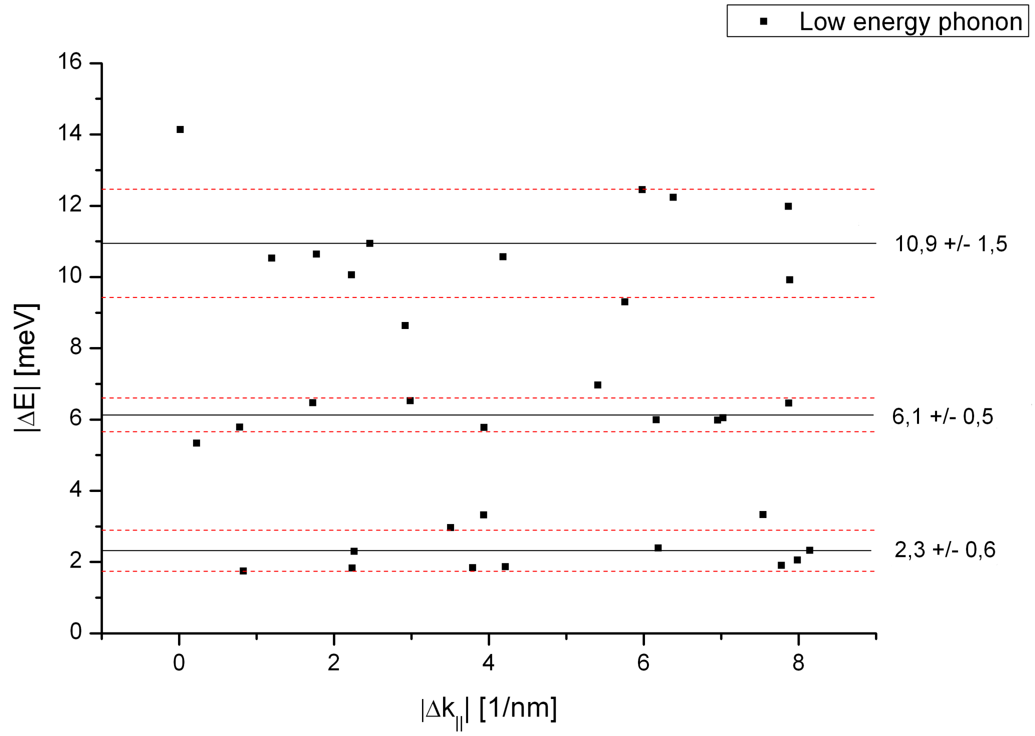

Figure 5.7: Measured phonon dispersion curves with the absolute energy values plotted in a single Brillouin zone in the $\Gamma\vec{K}$-direction. The size of the reciprocal lattice vector, $\mid \vec{G} \mid = 25,6\ \mathrm{nm}^{-1}$ The squares are the resolved low-energy phonons. The black line is the mean energy for a particular phonon branch, and the dashed, red line is the corresponding standard deviation. The measurements are shown within the first Brillouin zone.

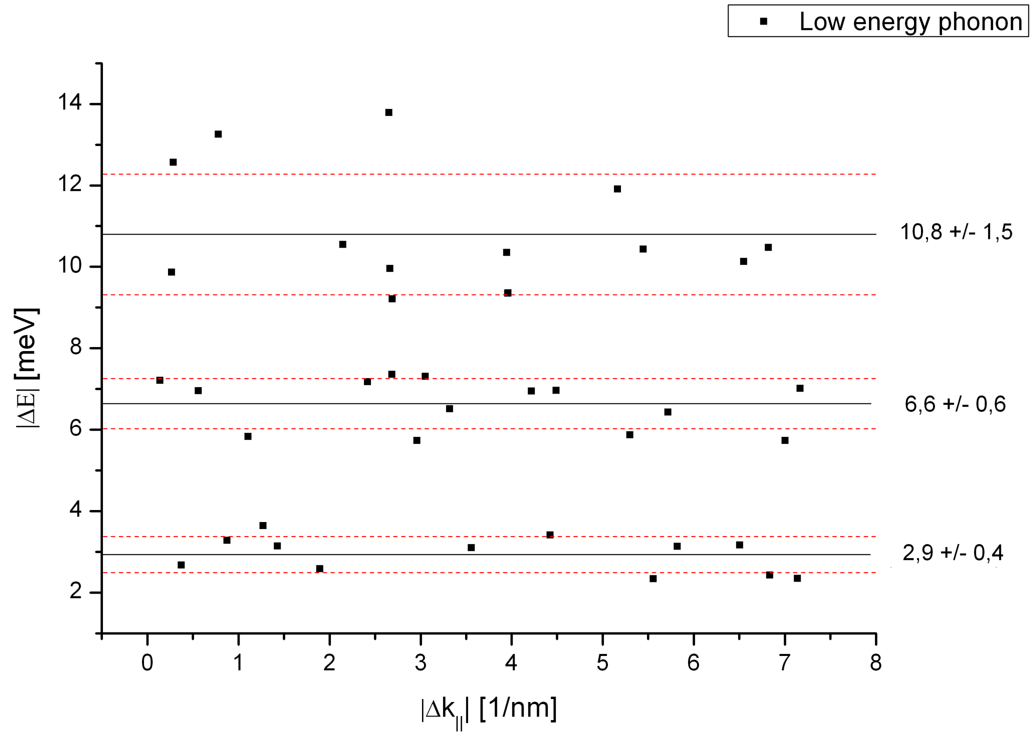

Figure 5.8: Measured phonon dispersion curves with the absolute energy values plotted in a single Brillouin zone in the $\Gamma\vec{M}$-direction. The size of the reciprocal lattice vector, $\mid \vec{G} \mid = 14,8$ nm^{-1} The squares are the resolved low-energy phonons. The black line is the mean energy for a particular phonon branch, and the dashed, red line is the corresponding standard deviation. The measurements are shown within the first Brillouin zone.

Chapter 6

Conclusion and outlook

The main aim for this thesis was to investigate if the low-energy surface phonons missing from earlier experiments was in fact present [23]. By performing measurements over a wider angular range and with a higher energy resolution than previous measurements and using a new fitting procedure, low-energy surface phonons of α-quartz (0001) surface could be found. The previous measurements can be predicted as the first overtone for this basic mode. Additional higher-order harmonics for the low-energy dispersionless mode corresponding to first and second overtone could also be found.

The first HAS diffraction from an α-quartz (0001) surface presented [12] propose a model of the α-quartz (0001) surface where the presence of terraces with step heights of 1/3 of the height of the unit cell is leading to domains rotated 60° relative to each other. This model and the experimental data corresponds well with the theoretical predictions that foresees an (1×1) surface reconstruction with 120° symmetry of the unit cell. The occurrence of the additional weak peaks can be explained as a (2×1) surface reconstruction, since a hexagonal (1×1) structure combined with three domains of (2×1) can give a diffraction pattern similar to a (1×1) structure combined with a (2×2) structure. The most recent paper by Chen et al. [31] states that the experimentally observed (2×2) pattern, can be explained by combinations of (2×1) surfaces which are more energetically stable than the dense (1×1) surfaces. These diffraction measurements have been reproduced for this thesis, where the periodicity for the hexagonal pattern corresponds to a repeat distance of about 4,9 Å. This is similar to what was found experimentally in [12].

Shortly after the publication of the first structural paper on α-quartz investigated with helium atom scattering, the first paper on the low-energy surface phonons on α-quartz was published [23]. The results from this paper did only partially agree with theory. And in particular no measurements of the predicted low-energy optical phonons could be found. For both the $\Gamma\vec{K}$ and $\Gamma\vec{M}$-direction we have measured a dispersion less optical phonon mode of 3 meV, a first overtone of 6 meV and a second overtone of 11 meV. The theoretical predicted values are 5 meV and 7,5 meV for the $\Gamma\vec{K}$-direction and 6 meV and 7.5 meV for the $\Gamma\vec{M}$-direction (not quite dispersionless). The predicted Rayleigh mode is not found in these initial experiments.

There are several possible explanations why the theory does not fit the experiments. The theoretical calculations are based on the (1×1)-dense structure [23], but

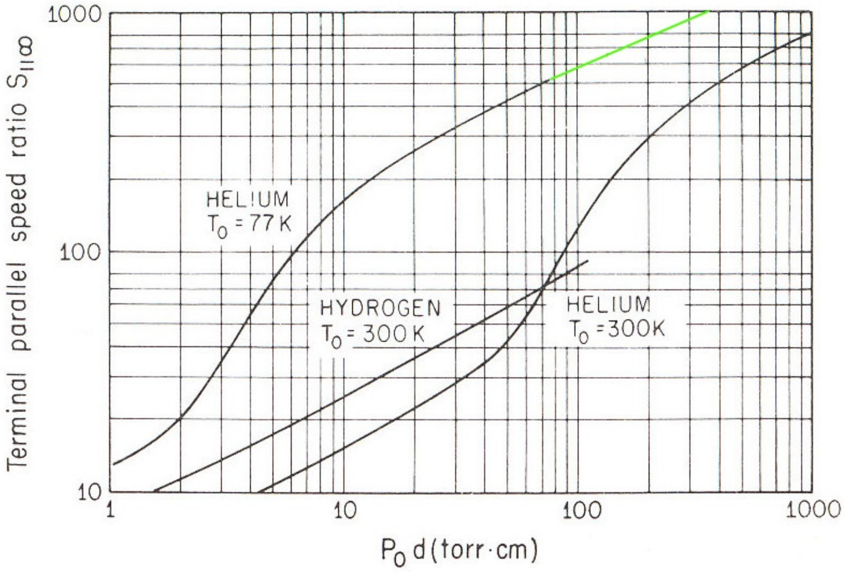

Figure 6.1: Terminal speed ratio versus source conditions for helium and hydrogen [42]. The green line is the linear extrapolated curve for thermal speed of helium with an initial temperature of 77 K. An initial pressure of 200 bar and a skimmer of 10 μm corresponds to a pressure times diameter ($p_0 \cdot d$) of 150 torr·cm.

we know from diffraction measurements that the surface is more complicated. Also, the long range surface reconstruction indicated by the satellite peaks is not taken into account. Hence, it is not even clear if the Brillouin zone is correctly defined. The large multi phonon background in the center of the Brillouin zone makes it difficult to resolve the Rayleigh phonon mode.

Future work on the α-quartz (0001) surface could be to should concentrate on finding the missing Rayleigh mode. For that one need a better signal to noise ratio and a better velocity resolution of the beam. With a longer measurement time for the TOF-measurement at a higher beam pressure, probably more low-energy phonon peaks could be resolved. With the current setup the pressure can be increased up to 200 bar, which would mean an improvement in the velocity spread of the beam from around 1% to about 0,2% [42]. A higher quality crystal surface could also help. The major improvement would be to cool the sample to liquid helium temperatures, which would decrease the multiphonon background. This would, however, require considerable reconstruction of the existing experimental equipment. Figure 6.1 shows the terminal speed ratio versus source conditions for helium and hydrogen used to estimate the velocity spread at higher source pressures.

In conclusion we have successfully reproduced the diffraction pattern, and calculated the same lattice constant as predicted by theory. With the new fitting procedure, a dispersionless, low-energy, optical surface phonon mode could be found in reasonably good agreement with theoretical predictions.

Appendix A

Table of TOF-files.

In this appendix, all the TOF-spectra used for analysis in this thesis are listed, including a list of the used energies.

A.1 $\Gamma\vec{K}$-direction

The TOF-files used for the analysis in the $\Gamma\vec{K}$-direction are listed in Table A.1.

A.2 $\Gamma\vec{M}$-direction

The TOF-files used for the analysis in the $\Gamma\vec{M}$-direction are listed in Table A.2.

Table A.1: TOF-files used for analysis in the $\Gamma\vec{K}$-direction. The peak in bold features is the elastic peak, and all the other energies are given in respect to this peak.

TOF-file	Incoming beam angle	Peak number	Energy [meV]
TOF2888	46.48°	1	21.20
		2	9.58
		3	4.59
		4	-10.80
		5	-6.45
		6	**24.4**
		7	-0.85
		8	2.06
		9	-1.88
TOF2889	47.40°	1	23.61
		2	11.71
		3	6.51
		4	-10.02
		5	-5.94
		6	**24.3**
		7	-0.94
		8	3.35
		9	-2.28
TOF2890	52.50°	1	26.97
		2	14.20
		3	8.06
		4	-11.23
		5	-8.58
		6	**24.3**
		7	-5.55
		8	-0.79
		9	-2.06
		10	4.57
TOF2891	48.48°	1	36.02
		2	16.26
		3	7.31
		4	-10.39
		5	-5.94
		6	**24.4**
		7	-0.63
		8	4.51
		9	-1.74

TOF-file	Incoming beam angle	Peak number	Energy [meV]
TOF2892	49.47°	1	18.39
		2	10.45
		3	6.29
		4	-10.00
		5	-5.70
		6	**24.4**
		7	-0.93
		8	-2.09
		9	3.74
TOF2893	50.48°	1	32.63
		2	18.83
		3	9.88
		4	-10.89
		5	-6.30
		6	**24.3**
		7	-0.05
		8	-3.50
		9	4.77
TOF2894	51.48°	1	30.05
		2	14.38
		3	6.48
		4	-10.69
		5	-5.76
		6	**24.4**
		7	-0.96
		8	2.26
		9	-2.93
TOF2895	52.98°	1	21.98
		2	10.40
		3	6.08
		4	-8.94
		5	-4.84
		6	**24.3**
		7	-0.53
		8	1.83
		9	-1.76
TOF2899	46.70°	1	24.88
		2	11.89
		3	5.26
		4	-12.00
		5	-7.01
		6	**24.4**
		7	-0.90
		8	2.40
		9	-1.82

Table A.2: TOF-files used for analysis in the $\Gamma\vec{M}$-direction. The peak in bold features is the middle peak, and all the other energies are given in respect to that.

TOF-file	Incoming beam angle	Peak number	Energy [meV]
TOF2907	44.09°	1	14.67
		2	7.12
		3	-8.20
		4	-5.76
		5	**24.3**
		6	-0.53
		7	-3.76
		8	-1.60
		9	1.85
		10	19.68
TOF2908	40.39°	1	19.68
		2	9.84
		3	7.20
		4	-9.50
		5	-5.89
		6	-5.02
		7	**24.4**
		8	-0.83
		9	3.29
		10	-1.96
TOF2909	44.41°	1	17.01
		2	9.99
		3	6.43
		4	-9.80
		5	-5.78
		6	**24.4**
		7	-1.01
		8	2.47
		9	-3.27
TOF2912	43.01°	1	22.40
		2	12.46
		3	7.28
		4	-10.39
		5	-7.25
		6	-5.51
		7	**23.1**
		8	0.33
		9	-2.69
		10	3.19

TOF-file	Incoming beam angle	Peak number	Energy [meV]
TOF2913	41.99°	1	26.20
		2	14.98
		3	7.90
		4	-10.41
		5	-6.91
		6	-4.55
		7	**23.0**
		8	0.51
		9	-3.15
		10	3.82
TOF2914	41.01°	1	18.29
		2	9.95
		3	6.36
		4	-9.22
		5	-7.53
		6	-4.93
		7	**23.1**
		8	0.14
		9	2.61
		10	-4.22
TOF2915	40.00°	1	22.37
		2	12.06
		3	6.88
		4	-9.74
		5	-7.21
		6	-4.93
		7	**23.1**
		8	0.08
		9	-2.24
		10	3.23
TOF2916	39.01°	1	29.97
		2	13.57
		3	7.38
		4	-10.36
		5	-8.20
		6	-5.74
		7	**23.1**
		8	1.21
		9	-2.33
		10	3.07

Appendix B

Figures of the TOF-spectra.

In this appendix you will find figures of all the TOF-spectra, including all the fitted peaks, used for analysis in this thesis.

B.1 $\Gamma\vec{K}$-direction

The TOF-files used for the analysis in the $\Gamma\vec{K}$-direction are shown in Figure B.1 to Figure B.9.

B.2 $\Gamma\vec{M}$-direction

The TOF-files used for the analysis in the $\Gamma\vec{M}$-direction are shown in Figure B.10 to Figure B.17.

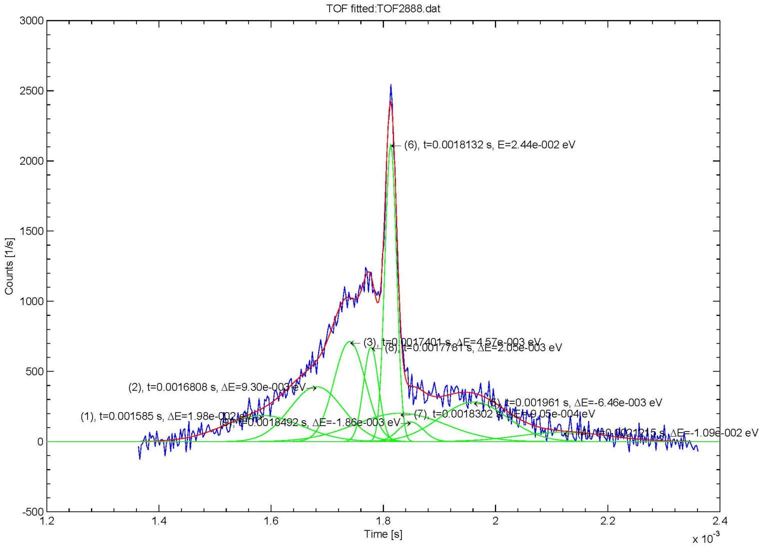

Figure B.1: TOF2888

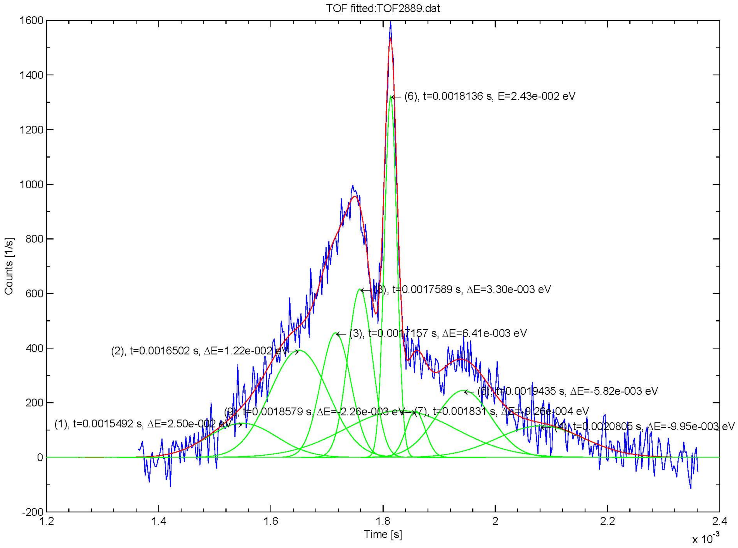

Figure B.2: TOF2889

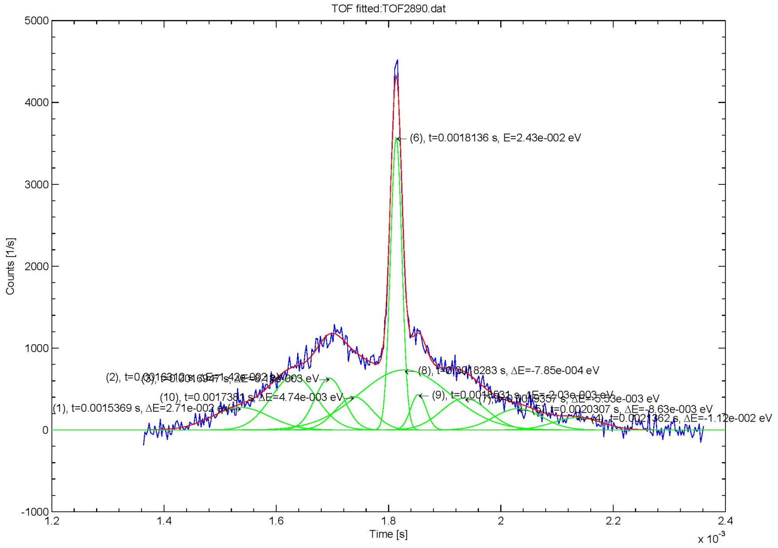

Figure B.3: TOF2890

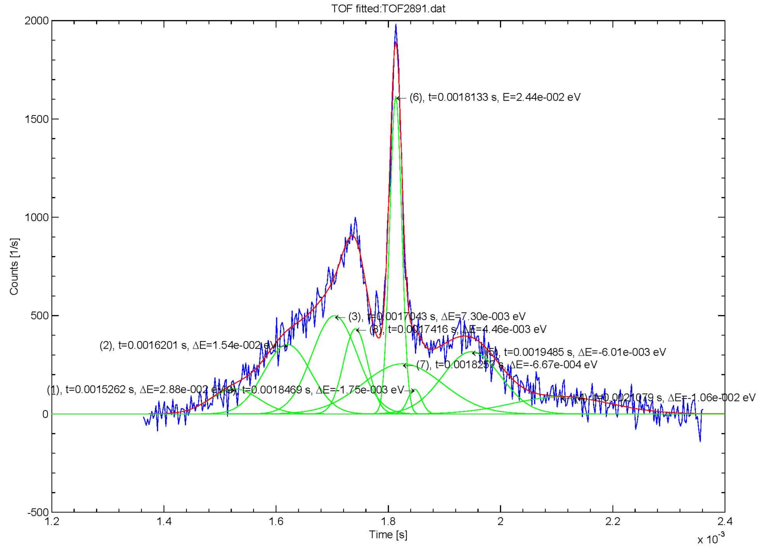

Figure B.4: TOF2891

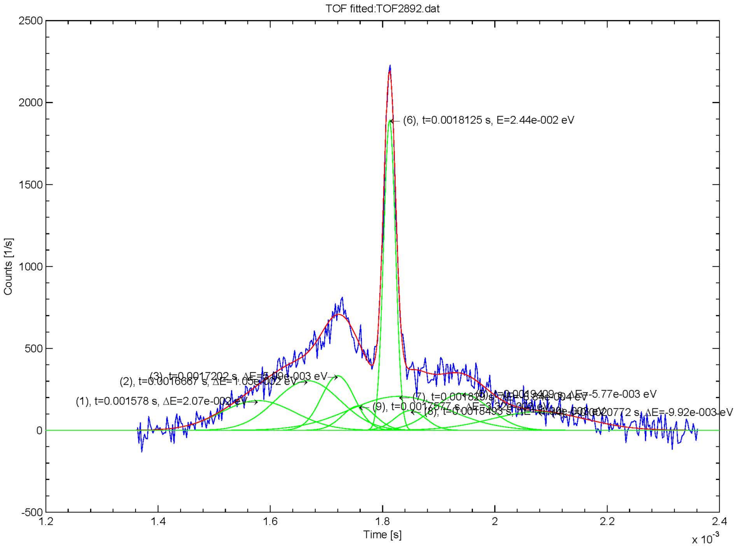

Figure B.5: TOF2892

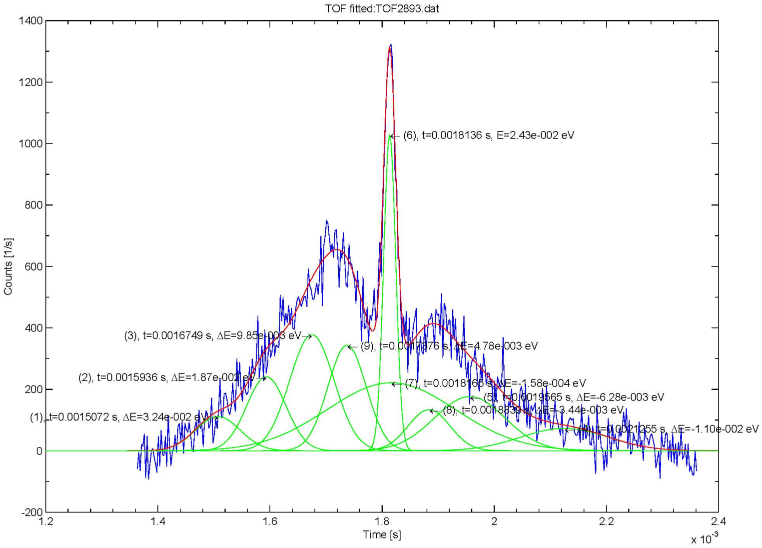

Figure B.6: TOF2893

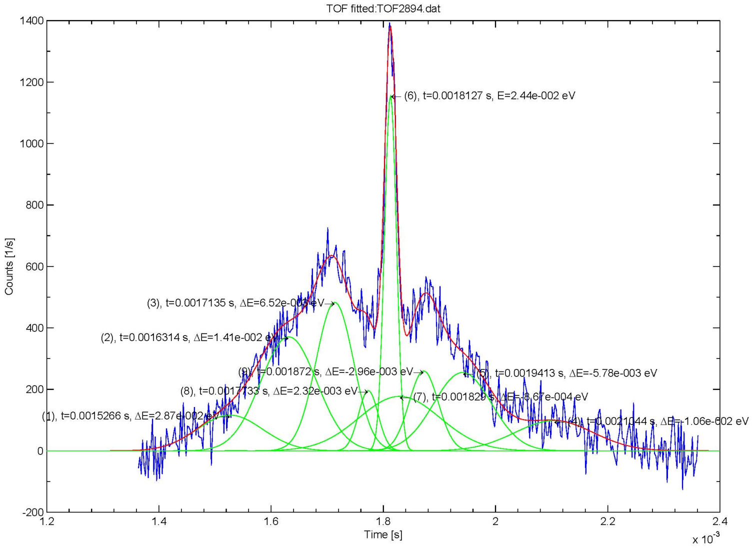

Figure B.7: TOF2894

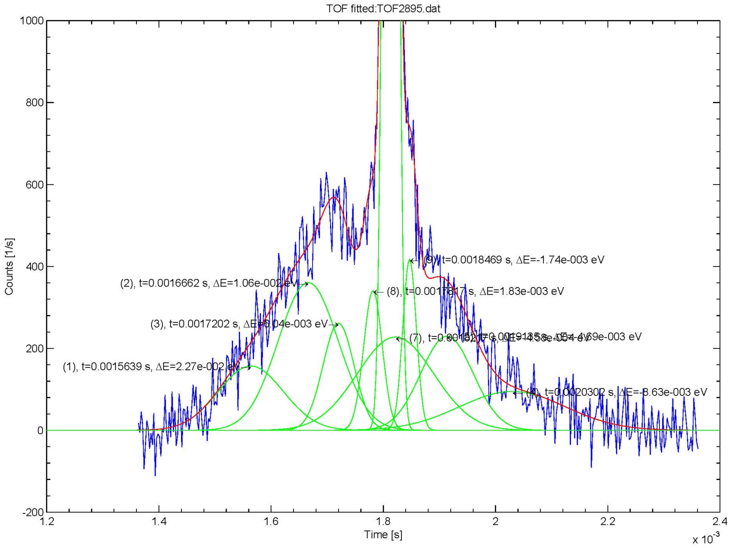

Figure B.8: TOF2895

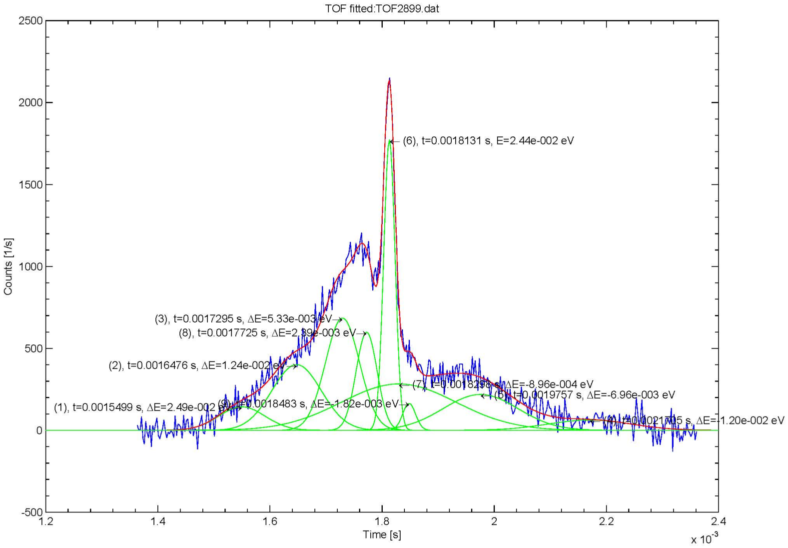

Figure B.9: TOF2899

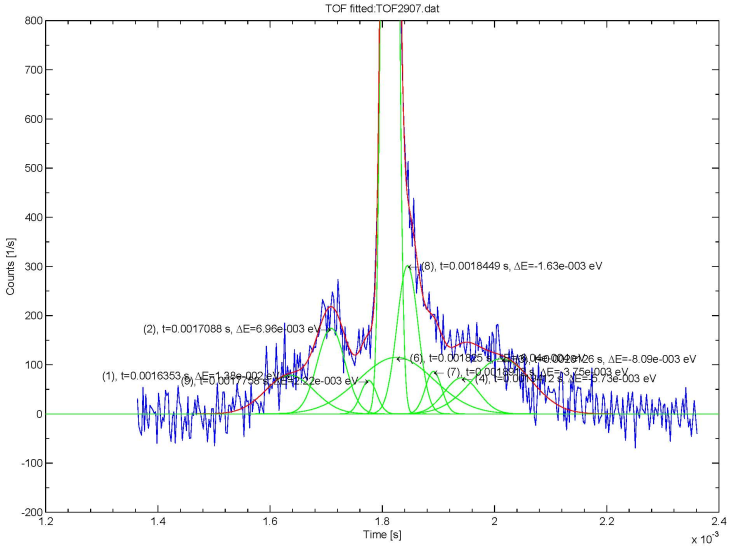

Figure B.10: TOF2907

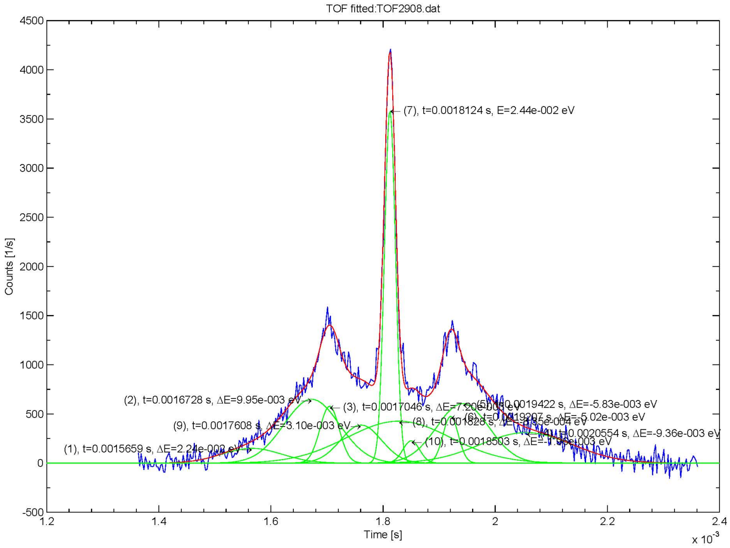

Figure B.11: TOF2908

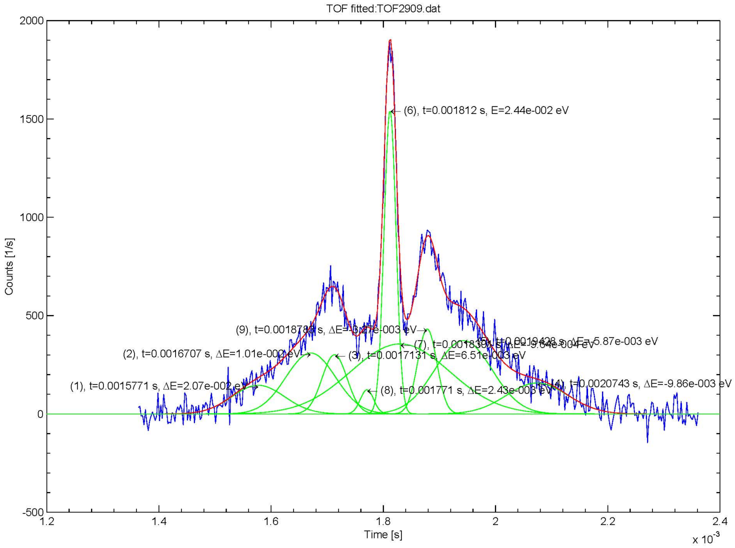

Figure B.12: TOF2909

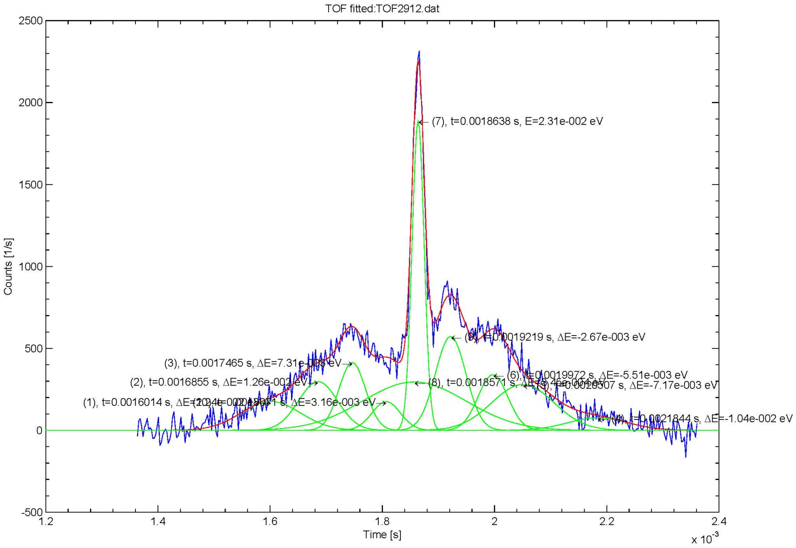

Figure B.13: TOF2912

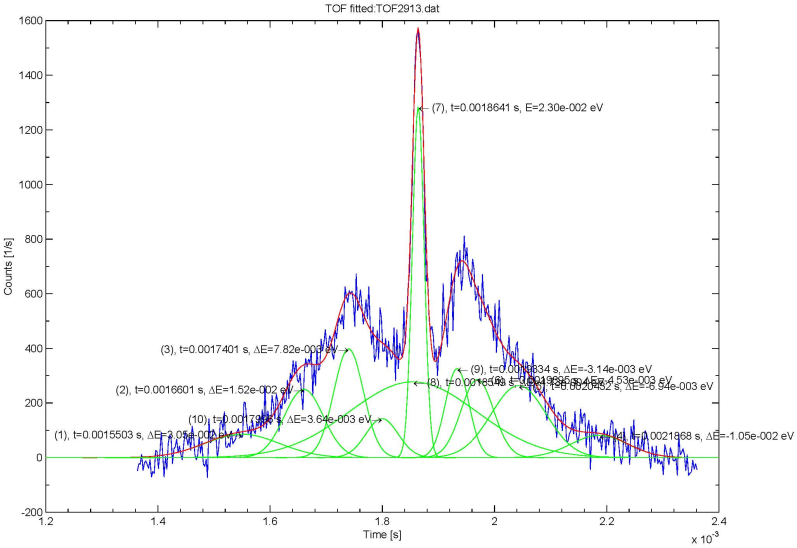

Figure B.14: TOF2913

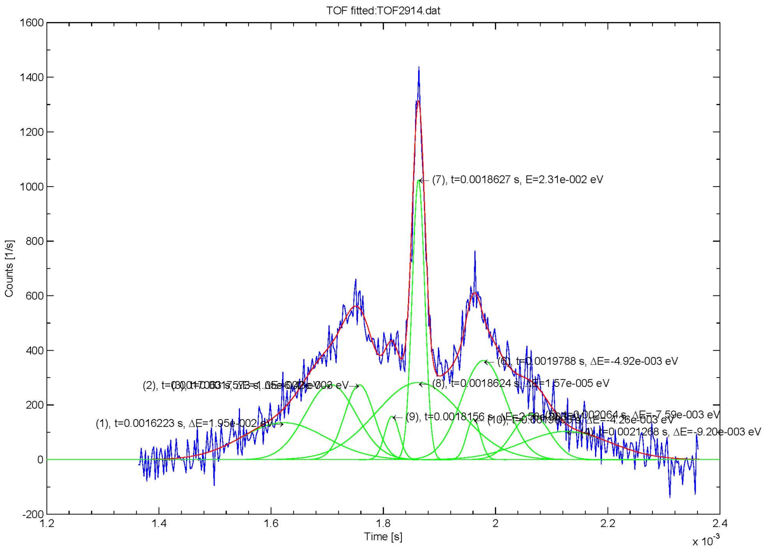

Figure B.15: TOF2914

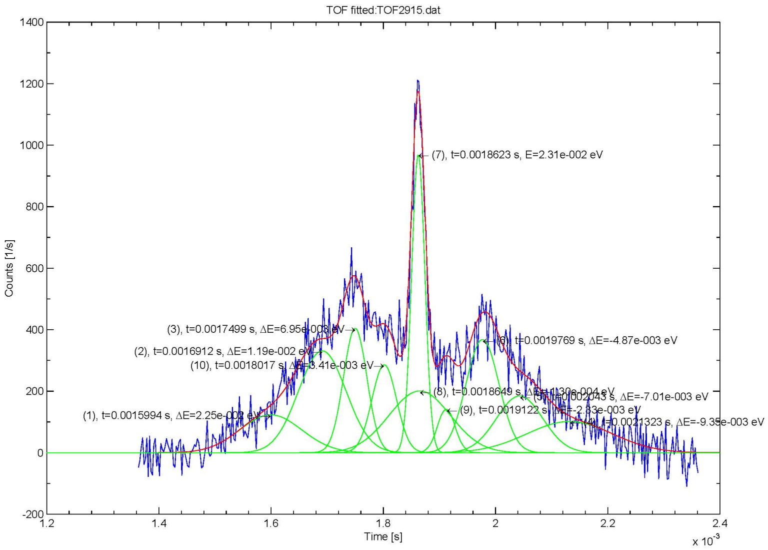

Figure B.16: TOF2915

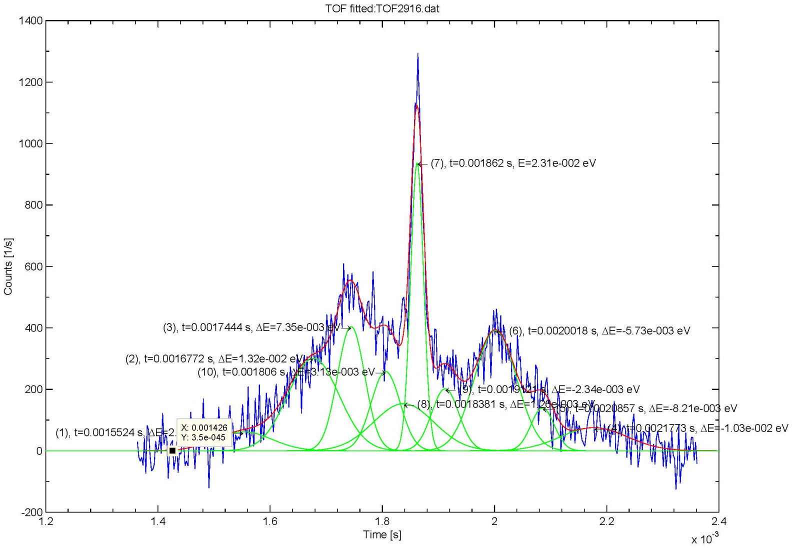

Figure B.17: TOF2916

Bibliography

[1] Torgeir T. Garmo, editor. *Norsk Steinbok*. Universitetsforlaget, 1995.

[2] Ch. Weißmantel and C. Hamann, editors. *Grundlagen der Festkörperphysic*. Johann Ambrosius Barth Verlag, 1995.

[3] Haakon Fossen. Quartz crystal from Hardangervidda. Bergen Museums collections.

[4] Peter J. Heaney. *Silica - Physical behaviour, geochemistry and materials applications*, chapter Structure and chemistry of the low-pressure silica polymorphs. Mineralogical Society of America, 1994.

[5] Wolfram Steurer. New Applications of Helium Atom Scattering: The α-Quartz (0001) Surface and the Influence of Steps on the Atom-Focussing Mirror. Master's thesis, Graz University of Technology, 2006.

[6] G. Kopitkovas, T. Lippert, N. Murazawa, C. David, A. Wokaun, J. Gobrecht, and R. Winfield. Laser processing of micro-optical components in quartz. *Applied Surface Science*, 254(4):1073–1078, 2007.

[7] S. Seidelin, J. Chiaverini, R. Reichle, J. J. Bollinger, D. Leibfried, J. Britton, J. H. Wesenberg, R. B. Blakestad, R. J. Epstein, D. B. Hume, W. M. Itano, J. D. Jost, C. Langer, R. Ozeri, N. Shiga, and D. J. Wineland. Microfabricated surface-electrode ion trap for scalable quantum information processing. *Phys. Rev. Lett.*, 96(25):253003, Jun 2006.

[8] R. Notman and T.R. Walsh. Molecular Dynamics Studies of the Interactions of Water and Amino Acid Analogues with Quartz Surfaces. *Langmuir*, 25(3):1638–1644, 2009.

[9] I. Jánossy. LEED study of quartz crystals. *Surface Science*, 25:647–649, 1971.

[10] F. Bart and M. Gautier. A LEED study of the (0001) α-quartz surface reconstruction. *Surface Science*, 311(1-2):L671–L676, 1994.

[11] M. Kawasaki, K. Onuma, and I. Sunagawa. Morphological instabilities during growth of a rough interface: AFM observations of cobbles on the (0001) face of synthetic quartz crystals. *Journal of Crystal Growth*, 258(1-2):188–196, 2003.

[12] W. Steurer, A. Apfolter, M. Koch, T. Sarlat, E. Søndergård, WE Ernst, and B. Holst. The structure of the α-quartz (0001) surface investigated using helium atom scattering and atomic force microscopy. *Surface Science*, 601(18):4407–4411, 2007.

[13] J.W. Han and D.S. Sholl. Enantiospecific adsorption of amino acids on hydroxylated quartz (10 10) w. *Phys. Chem. Chem. Phys*, 12:8024–8032, 2010.

[14] L. Tian, S.Q. Zhao, and K. Zhao. Annealing Effect on Photovoltages of Quartz Single Crystals. *Chinese Physics Letters*, 27:127301, 2010.

[15] PL Clay, EF Baxter, DJ Cherniak, SP Kelley, JB Thomas, and EB Watson. Two diffusion pathways in quartz: A combined UV-laser and RBS study. *Geochimica et Cosmochimica Acta*, 2010.

[16] F. Knauer and O. Stern. über die Reflexion von Molekularstrahlen. *Zeitschrift für Physik A Hadrons and Nuclei*, 53(11):779–791, 1929.

[17] I. Estermann and O. Stern. Beugung von Molekularstrahlen. *Zeitschrift für Physik A Hadrons and Nuclei*, 61(1):95–125, 1930.

[18] E. Hulpke, editor. *Helium Atom Scattering.* Springer-Verlag, 1992.

[19] BN Brockhouse and AT Stewart. Scattering of Neutrons by Phonons in an Aluminum Single Crystal. *Physical Review*, 100(2):756–757, 1955.

[20] J. Aldag and RM Stern. Surface Thermal Diffuse Scattering from Tungsten. *Physical Review Letters*, 14(21):857–860, 1965.

[21] J.R. Bledsoe and S.S. Fisher. Scattering of helium nozzle beams from LiF (001) and NaCl (001) crystal surfaces:: I. Elastic and inelastic transitions. *Surface Science*, 46(1):129–156, 1974.

[22] Bodil Holst. Why use helium to investigate materials, February 2009.

[23] W. Steurer, A. Apfolter, M. Koch, WE Ernst, B. Holst, E. Søndergård, and SC Parker. Low-energy surface phonons on α-quartz (0001). *Physical Review B*, 78(3):35402, 2008.

[24] Hemmer P. C., editor. *Faste Stoffers Fysikk.* Tapir Forlag, 1987.

[25] M. C. Desjonqueres and D. Spanjaard, editors. *Consepts in Surface Physics.* Springer-Verlag, 1998.

[26] Charles Kittel, editor. *Introduction to Solid State Physics.* John Wiley & Sons, 1986.

[27] Neil W. Ashcroft and N. David Marmin, editors. *Solid State Physics.* Brooks/Cole, 1976.

[28] Gerald Burns, editor. *Solid State Physics.* Academic Press, Inc, 1985.

[29] N.H. de Leeuw, F.M. Higgins, and S.C. Parker. Modeling the Surface Structure and Stability of α-Quartz. *J. Phys. Chem. B*, 103(8):1270–1277, 1999.

[30] G.M. Rignanese, A. De Vita, J.C. Charlier, X. Gonze, and R. Car. First-principles molecular-dynamics study of the (0001) α-quartz surface. *Physical Review B*, 61(19):13250–13255, 2000.

[31] Y.W. Chen, C. Cao, and H.P. Cheng. Finding stable α-quartz (0001) surface structures via simulations. *Applied Physics Letters*, 93:181911, 2008.

[32] J. Szeftel. Surface phonon dispersion, using electron energy loss spectroscopy. *Surface Science*, 152:797–810, 1985.

[33] M Henzler and W Göpel, editors. *Oberflächenphysik des Festkörpers*. B. G. Teubner Stuttgart, 1994.

[34] W Kress. *Surface Phonons*, chapter Vibrational Properties of Clean Surfaces: Survey of Recent Theoretical and Experimental Results. Springer-Verlag, 1991.

[35] Andreas Apfolter. Wiederaufbau und Test einer He-Streuapparatur und erste Streuexperimente an amorpher sowie kristalliner SiO2-Oberfläche. Master's thesis, Graz University of Technology, 2005.

[36] Yasin Ekinci. *High Resolution Scattering of He Atoms and D_2 Molecules from the LiF(001) Crystal Surface*. PhD thesis, Georg-August-University of Göttingen, 2003.

[37] J.H. Weare. Helium scattering from solid surfaces. *The Journal of Chemical Physics*, 61:2900, 1974.

[38] W. Steurer, A. Apfolter, M. Koch, WE Ernst, and B. Holst. Surface Debye temperature of α-quartz (0001). *Surface Science-Including Surface Science Letters*, 602(5):1080–1083, 2008.

[39] R. B. Doak. *Atomic and Molecular Beam Methods, Volume 2*, chapter Single-Phonon Inelastic Helium. Oxford University Press, 1992.

[40] Daniel V. Schroeder, editor. *An Introduction to Thermal Physics*. Addison Wealey Longman, 2000.

[41] A.P. Graham. The low energy dynamics of adsorbates on metal surfaces investigated with helium atom scattering. *Surface Science Reports*, 49(4-5):115–168, 2003.

[42] David R. Miller. *Atomic and Molecular Beam Methods, Volume 1*, chapter Free Jet Sources. Oxford University Press, 1988.

[43] Thomas Reisinger. Fresnel atom-optics experiments with a supersonic helium beam. Master's thesis, Graz University of Technology, 2007.

[44] Elin Søndergård. private communications, 2008.

[45] Daniel J. Auerbach. *Atomic and Molecular Beam Methods, Volume 1*, chapter Velocity Measurements by Time-of-Flight Methods. Oxford University Press, 1988.

[46] Katrin Fladischer. *Helium atom scattering experiments: neutral atom focusing and surface investigation of TFF and TCNQ molecules on Cu(100), NiAl(110) and* Al_2O_3*/NiAl(110)*. PhD thesis, Graz University of Technology, 2009.

[47] R. B. Doak. *Helium Atom Scattering*, chapter Experimental Limitations and Opportunities in Single-Phonon Inelastic Helium Scattering. Springer-Verlag, 1992.